TEXTURED SURFACES FOR ELECTROMAGNETIC APPLICATIONS

THESIS SUBMITTED BY

SAYAN SARKAR

DOCTOR OF PHILOSOPHY (ENGINEERING)

DEPARTMENT OF ELECTRONICS AND
TELECOMMUNICATION ENGINEERING

FACULTY COUNCIL OF ENGINEERING & TECHNOLOGY

JADAVPUR UNIVERSITY
KOLKATA, INDIA

2022

JADAVPUR UNIVERSITY

KOKATA – 700032, INDIA

INDEX NO. 268/20/E

1. **Title of the Thesis**:

   TEXTURED SURFACES FOR ELECTROMAGNETIC APPLICATIONS

2. **Name, Designation & Institution of the Supervisors**:

   DR. BHASKAR GUPTA

   Professor, Dept. of Electronics and Telecommunication Engineering, Jadavpur University, Kolkata – 700032, West Bengal, India

3. **List of Publications**:

JOURNALS

I. **Sayan Sarkar** and Bhaskar Gupta, "*Ultrathin chiral metasurface with multiple functionalities,*" **International Journal of RF and Microwave Computer-Aided Engineering**, vol. 32, no. 11, article number e23345, 2022.

II. **Sayan Sarkar** and Bhaskar Gupta, "*Multiband Chiral Metasurface for Asymmetric Reflection and Transmission of Circularly Polarized Waves,*" **IEEE Antennas and Wireless Propagation Letters**, vol. 21, no. 1, pp. 178-182, 2022.

III. **Sayan Sarkar** and Bhaskar Gupta, "*Multiband Ultrathin Chiral Metasurface for Polarization Conversion, Symmetric and Asymmetric Transmission,*" **AEU - International Journal of Electronics and Communications,** vol. 142, article number 154009, 2021.

IV. **Sayan Sarkar** and Bhaskar Gupta, "*A Tri-band Spoof Surface Plasmon Polaritons Based Antenna for Endfire Radiation,*" **International Journal of RF and Microwave Computer-Aided Engineering**, vol. 31, no. 7, article number e22668, 2021.

V. **Sayan Sarkar** and Bhaskar Gupta, "*A Dual-Band Fabry-Perot Cavity Antenna with a Single Partially Reflecting Surface and Reduced Cavity Height for WLAN Applications,"* **Radioengineering,** vol. 30, no. 1, pp. 104-110, 2021.

VI. **Sayan Sarkar** and Bhaskar Gupta, "*Artificial magnetic conductor with self-complementary unit cells having high angular stability,"* **IET Electronics Letters**, vol. 56, no. 14, pp. 704-706, 2020.

VII. **Sayan Sarkar** and Bhaskar Gupta, "*A Dual Band Circularly Polarized Antenna with a Dual Band AMC Reflector for RFID Readers,*" **IEEE Antennas and Wireless Propagation Letters**, vol.19, no.5, pp. 796-800, 2020.

CONFERENCES

I. **Sayan Sarkar**, Bhaskar Gupta, "*Ultrathin Dual-Band Metasurface for UHF-RFID and WLAN Applications,"* 2021 IEEE International Conference on RFID – Technology and Applications (**IEEE RFID-TA**), 2021, pp. 101-104.

4. **List of Patents**: NIL

5. **List of Presentations in National/International/Conferences/Workshops**:

I. Paper titled "*Ultrathin Dual-Band Metasurface for UHF-RFID and WLAN Applications"* presented in **2021 IEEE International Conference on RFID – Technology and Applications** held from 6-8th October 2021 by **Sayan Sarkar.**

STATEMENT OF ORIGINALITY

I, **Sayan Sarkar**, registered on **12/10/2020** do hereby declare that this thesis entitled "**Textured Surfaces for Electromagnetic Applications**" contains literature survey and original research work done by the undersigned candidate as part of Doctoral studies.

All information in this thesis has been obtained and presented in accordance with the existing academic rules and ethical conduct. I declare that, as required by these rules and conduct, I have fully cited and referred all materials and results that are not original to this work.

I also declare that I have checked this thesis as per the "Policy on Anti Plagiarism, Jadavpur University, 2019", and the level of similarity as checked by iThenticate software is 1%.

Signature of Candidate

Date: 9/11/2022

Certified by Supervisor(s):

Prof. Bhaskar Gupta
Professor
Dept. of E. & T.C. Engg.
Jadavpur University
Kolkata

Dr. Bhaskar Gupta
Professor, Dept. of ETCE
Jadavpur University, Kolkata – 700032

CERTIFICATE FROM THE SUPERVISORS

This is to certify that the thesis entitled "**Textured Surfaces for Electromagnetic Applications**" submitted by **Shri Sayan Sarkar**, who got his name registered on **12/10/2020** for the award of Ph. D. (Engg.) degree of Jadavpur University is absolutely based upon his own work under the supervision of **Prof. Bhaskar Gupta**, Dept. of Electronics and Telecommunication Engineering, Jadavpur University, Kolkata – 700032, West Bengal, India, and that neither his thesis nor any part of the thesis has been submitted for any degree/diploma or any other academic award anywhere before.

Prof. Bhaskar Gupta
Professor
Dept. of E. & T.C. Engg.
Jadavpur University
Kolkata

Bgupta 07/11/22

Dr. Bhaskar Gupta
Professor, Dept. of ETCE
Jadavpur University, Kolkata – 700032

ACKNOWLEDGEMENTS

Firstly, I wish to take this opportunity to thank my supervisor **Professor Bhaskar Gupta** and acknowledge the deep impact he has had in cultivating within me the interest and curiosity that I have developed towards the theory and applications of Electromagnetism of which Microwave Engineering is but a small part. His patience, the immense knowledge he shares with us and the relationship he has with all his students clearly brings out the best in them. I am very thankful that I have been able to work under the guidance of such an able and well-established professor.

I wish to express my gratitude to the current Head of the Department of ETCE, **Prof. Manotosh Biswas** and the past HoD, **Prof. Ananda Shankar Chowdhury** for always extending a helping hand whenever I needed it.

I would like to thank **Dr. Amartya Banerjee**, **Dr. Suman Pradhan**, **Mr. Ardhendu Kundu**, **Mr. Joydeep Pal**, **Mr. Sourav Banik**, **Dr. Kaushik Patra**, **Dr. Ayona Chakraborty** and **Mr. Soham Ghosh** for all their help and support. This thesis would not have been complete without their help and co-operation.

Lastly, but most importantly, I would like to thank my father, mother, and grandmother for encouraging me to pursue the subject I love and for their constant and unwavering faith in my abilities. Without their support, I would not be where I am today. Unfortunately, my grandfather, who was also extremely supportive of me throughout my life, passed away in 2020 without getting to see me finish my doctorate course. He was very enthusiastic about higher studies and always kept himself updated about my progress. This dissertation is dedicated to his memory.

Sayan Sarkar

Dated: 7/11/2022

CONTENTS

List of Figures vi

List of Tables xi

Acronyms xii

CHAPTER 1: Introduction 1

1.1 Textured Surfaces 1

- 1.1.1 Dimensional Constraints 2
- 1.1.2 Advantage of Periodicity 2
- 1.1.3 Unique Properties and Uses of Textured Surfaces 4

1.2 Motivation of the Thesis 5

1.3 Organization of the Thesis 5

CHAPTER 2: Literature Review 9

2.1 HIS 9

2.2 FPC using PRS 12

2.3 CMS 13

2.4 SSPP 14

2.5 Conclusions 15

CHAPTER 3: Analyzing the Textured Surfaces 30

3.1 High Impedance Surface - HIS 30

3.1.1 Analysis 30

3.1.2 Unique Properties of the HIS 31

3.1.3 Effects of the metallic vias on the EBG and AMC properties 37

3.1.4 Effect of angle of incidence on the AMC property 39

3.2 Partially Reflecting Surface - PRS 40

3.2.1 Working Principle of the FPC made using PRS 40

3.2.2 Narrow operating region due to resonance condition 42

3.3 Chiral Metasurface – CMS 42

3.3.1 Polarization plane rotation 43

3.3.2 Asymmetric Transmission of LP and CP waves 44

3.4 Spoof Surface Plasmon Polariton – SSPP 46

3.4.1 Surface Plasmon Polaritons 46

3.4.2 Spoof Surface Plasmon Polaritons 50

3.5 Conclusions 51

CHAPTER 4: A Dual-band AMC Reflector with UHF-RFID Reader 53

4.1 Introduction to RFID 53

4.2 Objective 54

4.3 Antenna and AMC design 54

4.4 Antenna Characteristics 57

4.5 Conclusions 66

CHAPTER 5: An AMC having very high Angular Stability 68

5.1 Objective 68

5.2 AMC unit cell geometry and Equivalent Circuit 68

5.3 Simulated response of the AMC 70

5.4 Evaluation of the Equivalent Circuit Parameters 72

5.5 Experimental Verifications 75

5.6 Conclusions 78

CHAPTER 6: FPC Antenna with AMC ground and Reduced Cavity Height 80

6.1 Objective 80

6.2 PRS and AMC Unit Cell designs 81

    6.2.1 PRS Unit Cell 81

    6.2.2 AMC Ground Plane 83

6.3 Patch Antenna 85

6.4 Fabry-Pérot Cavity Antenna 86

    6.4.1 Experimental Verifications 87

6.5 Conclusions 91

CHAPTER 7: A Multiband Multifunctional Chiral Metasurface 93

7.1 Objective 93

7.2 Unit Cell Geometry and Response 94

7.2.1 Effects of adding the semicircular metallic arcs 98

7.2.2 Co-T bands 99

7.2.3 Linear to circular polarization conversion band 99

7.2.4 Induced surface currents 100

7.2.5 Band tuning and performance optimization 102

7.3 Experimental Verification 103

7.3.1 Co-T band 105

7.3.2 LTC band 106

7.3.3 Polarization conversion ratio (PCR) 107

7.4 Comparisons with similar structures and advantages of the proposed MS 109

7.5 Conclusions 110

CHAPTER 8: A Multiband Meta-Mirror 112

8.1 Concept of a Meta-Mirror 112

8.2 Objective 112

8.3 Unit Cell design 113

8.4 CMS Properties 114

8.4.1 Importance of the different parts of the Unit Cell 116

8.4.2 Induced Surface Current Distributions 117

8.4.3 Tuning the Frequency Bands 118

8.5 Experimental Verifications 119

8.6 Conclusions 122

CHAPTER 9: A Tri-band SSPP based End-fire Antenna 124

9.1 Objective 124

9.2 Proposed Antenna Geometry 124

9.2.1 SSPP Unit Cell 126

9.2.2 Unequal Dimensions of the CPW Ground Planes 127

9.2.3 Evolution of the Bottom Structure Geometry 128

9.3 Electric Field Distributions 129

9.4 Tuning the Frequency Bands 130

9.5 Experimental Verifications and Antenna Radiation Patterns 133

9.6 Advantages of the Proposed SSPP based Antenna 136

9.7 Conclusions 138

CHAPTER 10: Conclusions 140

10.1 Contributions of the Thesis 140

10.2 Future Research Areas 141

LIST OF FIGURES

Fig. 1.1. The three main branches of texture surfaces that will be the discussed in the dissertation. 1

Fig. 1.2. Arbitrary periodic structure having periodicity in the z-direction. 2

Fig. 3.1. Mushroom type HIS. 30

Fig. 3.2 (a) Capacitance and inductance of the unit cells and (b) equivalent lumped circuit model. 31

Fig. 3.3. Surface wave propagation along an impedance surface. 31

Fig. 3.4. Field arrangements of the TM and TE surface waves propagating along the impedance surface. (J = surface current density) 32

Fig. 3.5. (a) An HIS unit cell consisting of a square metallic patch on a grounded dielectric substrate. (b) The patch is connected to the ground plane with a metallic via. The substrate used is FR-4 (ε_r=4.3, tanδ =0.02) with a thickness of 1.52mm. 33

Fig. 3.6. Dispersion diagram of a typical HIS. 33

Fig. 3.7 (a) Antenna with conventional reflector, (b) antenna with HIS reflector. 35

Fig. 3.8 (a) PBCs and Ports during CST analysis. (b) Reflection phase diagram of the HIS of Fig. 3.5. 36

Fig. 3.9. Unit cell. 38

Fig. 3.10. Reflection phase, induced current magnitude and induced current phases of the 2D array of metallic patches on a grounded dielectric without the presence of vias. 39

Fig. 3.11. TE and TM polarized oblique incident waves. 39

Fig. 3.12. Ray diagram demonstrating working principle of an FPC. 40

Fig. 3.13. Field configurations for TM incidence at the interface between two media. 47

Fig. 3.14. Illustration of an SPP wave existing in air-metal interface. 49

Fig. 3.15. Dispersion curve for an SPP wave existing in air-metal interface. 50

Fig. 4.1. Circular patch antenna (a) top and (b) bottom. 54

Fig. 4.2. Real part and argument of the individual slot admittances (subscript h = horizontal slot; subscript v = vertical slot). 55

Fig. 4.3. (a) AMC until cell (Grey = metal, white = substrate). (b) Reflection phase and magnitude plot. 56

Fig. 4.4. Fig. 4.4. Fabricated antenna with AMC reflector containing 25-unit cells (a) Top View, (b) Side view illustration and (c) 3D view. 57

Fig. 4.5 (a) Different measurement configurations. (b) Practical setup for performing the measurements. 58

Fig. 4.6 (a) Reflection coefficient magnitude vs. frequency. (b) Axial ratio (AR) vs. frequency. 59 - 60

Fig. 4.7. Simulated surface current distributions (A/m) at (a) 915MHz and (b) 2.45GHz. 60 - 61

Fig. 4.8. Radiation patterns at (a) Co-pol 915MHz, (b) Co-pol 2.45GHz, (c) Cross-pol 915MHz and (d) Cross-pol 2.45GHz. Vertical markings are in dBi. 62 - 63

Fig. 4.9. Simulated axial ratio (dB) versus angular variations at (a) 915MHz and (b) 2.45GHz. 64

Fig. 4.10. Comparisons of AR vs. elevation angle between dual-band AMC and single-band AMC. 65

Fig. 5.1 (a) Unit cell geometry. Equivalent circuit of unit cell for (b) E_y incidence and (c) E_x incidence. 69

Fig. 5.2 (a) Plane wave incidence on the AMC. (b) Parallel connection between cell impedance and grounded dielectric impedance. 70

Fig. 5.3 (a) Simulated reflection phase for different E-field polarization angles phi (ϕ) and normal incidence ($\theta = 0°$). (b) Simulated TE/TM reflection phase for different incident angles (θ). 71

Fig. 5.4. CST and ADS response comparison for (a) E_y incidence and (b) E_x incidence. 74

Fig. 5.5 (a) Phase measurement configurations for normal incidence. (b) TE and TM incidence phase measurement configurations. 75-76

Fig. 5.6 (a) Fabricated prototype with 196 unit cells. Measured reflection phases for (b) various phi and (c) various TE and TM oblique incidence angles. 76-77

Fig. 6.1. PRS (a) top, (b) bottom and (c) CST analysis ports and PBCs. 81

Fig. 6.2. Reflection coefficient magnitudes and phases of the PRS within the (a) 2.4GHz band and (b) 5.8GHz band. 82

Fig. 6.3. E-field distributions (V/m) at (a, b) 2.4GHz and (c, d) 5.8GHz. 82-83

Fig. 6.4 (a) AMC unit cell geometry. (b) Reflection coefficients within the (b) 2.4GHz and (c) 5.8GHz bands. 84

Fig. 6.5 (a) Patch antenna geometry. Induced surface currents (A/m) at (b) 2.4GHz and (c) 5.8GHz. 85

Fig. 6.6 (a) Simulated FPCA. (b) Fabricated FPCA and (c) Measurement setup with inset picture of the VNA. 86-87

Fig. 6.7. S_{11} parameters of the FPCA within (a) 2.4GHz band and (b) 5.7GHz band. (c) AR vs. freq within 2.4GHz band. 87

Fig. 6.8. E-field distributions (V/m) within the FP cavity at (a) 2.4GHz and (b) 5.8GHz. 88

Fig. 6.9. Far field radiation patterns at (a) Co-pol 2.4GHz, (b) Co-pol 5.8GHz, (c) Cross-pol (opposite handedness) 2.4GHz and (d) Cross-pol 5.8GHz. 88-89

Fig. 6.10. (a) Simulated radiation efficiencies within the two bands. Peak gain vs. frequency plots within the (b) 2.4GHz band and (c) 5.8GHz band. 90

Fig. 7.1. Unit cell (a) top view, (b) bottom view and (c) 3D view. 95

Fig. 7.2. Simulated co– and cross-polarized reflection and transmission parameters for a –z directed LP incident plane wave (forward wave) having (a) E_x component and (b) E_y component. 96

Fig. 7.3. Transmission bands of the MS when (a) –z directed LP plane wave (forward wave) is incident on the top surface (Side 1) and (b) + z directed LP plane wave (backward wave) is incident on bottom surface (Side 2). 97

Fig. 7.4. Simulated asymmetric transmission parameter Δ_{lin}^{i} for the CMS. 97

Fig. 7.5. Transmission parameters with and without the semicircular arcs for incident LP plane wave (forward wave) having (a) E_x component and (b) E_y component. 98

Fig. 7.6. Simulated surface currents (A/m) of top and bottom layers for normal incidence of a forward EM wave at (a) 3.3GHz (for E_x and E_y incidence), (b) 4.1GHz (for E_y incidence), (c) 5.7GHz (for E_y incidence), (d) 6.3GHz (for E_y incidence), (e) 9.8GHz (for E_x incidence), (f) 11.5GHz (for E_x incidence) and (g) 12.8GHz (for E_y incidence). 100-101

Fig. **7.7.** Effects of varying L-cell on (a) co– and (b) cross-polarized transmission coefficients. 102-103

Fig. 7.8 (a) Fabricated MS with 144 unit cells. Measurement configurations (b) for normal incidence and (c) TE, TM incidence. (d) Measurement setup for co- (left) and cross- (right) polarization measurements. 103-104

Fig.7. 9. Measured co- and cross- polarized magnitudes and phases within the LTC band. 105

Fig.7. 10. Angular stability of the Co-T band for (a) TM and (b) TE incidence. 106

Fig. 7.11 (a), (b) The AR and (c), (d) S_3/S_0 ratios of the proposed MS for TE incidence within the LTC band. 106-107

Fig. 7.12. Simulated and measured PCR for (a) E_y incident on Side 1 and (b) E_x incident on Side 1. 108

Fig. 7.13. Measured PCR for (a) TE incidence and (b) TM incidence on Side 1. 108-109

Fig. 8.1. Comparison between a conventional mirror and meta-mirror. 112

Fig. 8.2 (a) Top and (b) bottom geometry of the CMS unit cell. 113

Fig. 8.3. Reflection coefficients of the CMS for (a) LHCP forward incidence (RHCP backward incidence) and (b) RHCP forward incidence (LHCP backward incidence). 114

Fig. 8.4. Simulated asymmetry parameter of the proposed CMS. 115

Fig. 8.5. (a) Evolution of the unit cell geometry and (b) asymmetry parameters for the three configurations of the unit cell. 116

Fig. 8.6. Simulated surface current distributions (A/m) on the top and bottom layers for normal incidence of a forward EM wave at (a) 5.66GHz (for LHCP incidence), (b) 6.16GHz (for RHCP incidence), (c) 10.55GHz (for RHCP incidence), (d) 11.11GHz (for LHCP incidence) and (e) 12.1GHz (for LHCP incidence). 117

Fig. 8.7. Asymmetric parameter of scaled MS. 118

Fig. 8.8. Fabricated prototype of the MS having 144 unit cells. 119

Fig. 8.9 Co-polarization (left) and cross-polarization reflection coefficient measurement setups. 120

Fig. 8.10 (a) Simulated and measured PCR at normal incidence. Variations of the (b) PCR and (c) Δ_{rx} for LHCP and RHCP oblique incidence. 121

Fig. 8.11 (a) LHCP and RHCP antenna pairs used for measurement (left) and measurement setup (right). (b) Measuring the reflection coefficient magnitude within the 5.5-5.8GHz band for LHCP incidence. (c) Measuring the reflection coefficient magnitude within the 6.1-6.25GHz band for RHCP incidence 122

Fig. 9.1. Proposed antenna (a) top and (b) bottom surface. (c) End view of the antenna showing waveguide port position and E-field distributions (V/m). 125

Fig. 9.2. Dispersion diagrams of the SSPP unit cell with varying h. 126

Fig. 9.3. S_{11} vs. frequency for three different cases. 127

Fig. 9.4 (a), (b), (c) Evolution of bottom geometry. (d) S_{11} vs. frequency for the three bottom geometries. 128

Fig. 9.5. Average E-field distributions (V/m) on the top (left) and bottom (right) surfaces at (a) 7.7GHz, (b) 8.5GHz and (c) 12.6GHz. 129-130

Fig. 9.6. Tuning the (a) first band, (b) second band and (c) third band. 131-132

Fig. 9.7 (a) Fabricated prototype top and bottom. (b) Comparison between simulated and measured S_{11}. 133

Fig. 9.8. Normalized simulated and measured far field patterns at (a) 7.7GHz, (b) 8.5GHz, (c) 12.4GHz, (d) 12.6GHz and (e) 13GHz. 134-135

Fig. 9.9. Measured peak gain vs. frequency and simulated efficiency vs. frequency within the third band. 136

LIST OF TABLES

Table 3.1. Comparing the PEC, PMC and AMC. 37

Table 4.1. Effects of introducing the AMC reflector. 63

Table 4.2. Comparisons with other dual-band UHF-RFID readers present in literature. 65

Table 5.1. Approximate theoretical values of the equivalent circuit parameters. 73

Table 5.2. Optimized values of the equivalent circuit parameters. 73

Table 5.3. Comparisons with previous works. 78

Table 6.1. Comparisons of the proposed FPCA with dual-band FPCAs found in literature. 91

Table 7.1. Comparisons with similar structures found in literature. 110

Table 9.1. Comparisons with some existing end-fire antennas. 137

ACRONYMS

AMC = Artificial Magnetic Conductor

AR = Axial Ratio

AS = Absorbing Surface

AT = Asymmetric Transmission

AUT = Antenna under Test

BW = Bandwidth

CMS = Chiral Metasurface

CP = Circular Polarization/ Circularly Polarized

CPC = Cross-polarization Conversion

CPW = Co-planar Waveguide

EBG = Electromagnetic Band Gap

EHF = Extremely High Frequency

EM = Electromagnetic/Electromagnetism

FSS = Frequency Selective Surface

FPC = Fabry-Pérot Cavity

FPCA = Fabry-Pérot Cavity Antenna

GW = Gap Waveguide

HF = High Frequency

HIS = High Impedance Surface

LHCP = Left-hand CP

LP = Linear Polarization/ Linearly Polarized

LTC = Linear to Circular

MS = Metasurface

PBC = Periodic Boundary Condition

PBG = Photonic Band Gap

PEC = Perfect Electric Conductor

PMC = Perfect Magnetic Conductor

PRS = Partially Reflecting Surface

RCS = Radar Cross Section

RFID = Radio Frequency Identification

RHCP = Right-hand CP

RS = Reflecting Surface

SCUC = Self-complementary Unit Cell

SHF = Super High Frequency

SMA = Sub-Miniature A

SRG = Self/series Resonant Grid

SP = Surface Plasmon

SPP = Surface Plasmon Polariton

SSPP = Spoof Surface Plasmon Polariton

SSN = Simultaneous Switching Noise

TE = Transverse Electric

TEM = Transverse Electromagnetic

TM = Transverse Magnetic

UHF = Ultra High Frequency

WLAN = Wireless Local Area Network

WPT = Wireless Power Transfer

VHF = Very High Frequency

VNA = Vector Network Analyzer

CHAPTER 1

INTRODUCTION

1.1 Textured Surfaces

The word *meta* originated from the Greek word μετά. It is a prefix which can be used to mean *beyond*, *transcending* or *more comprehensive*. In electromagnetic (EM) theory, the term metamaterial (MM) is usually given to an engineered/artificial material which possesses properties not found in its constituent elements. MMs can exhibit many unconventional properties like negative refraction, reversed Doppler shift, reversed Goos-Hänchen shift and many others [1]. MMs in the true sense are 3D structures. The unit cell of an MM is arranged periodically along all the three axes (x, y, and z). When the unit cell is arranged periodically along only two axes, i.e., in a single plane, then it creates a **metasurface (MS)**. So metasurfaces can be considered to be the 2D equivalent of metamaterials. The focus of this dissertation will be metasurfaces. Since MSs are mostly created by periodically repeating the same unit cell in a plane, we can also call them **textured surfaces. In this dissertation, the term *textured surfaces* and *metasurfaces* are used interchangeably**. The three main branches of textured surfaces that this dissertation will revolve around are presented in Fig. 1.1.

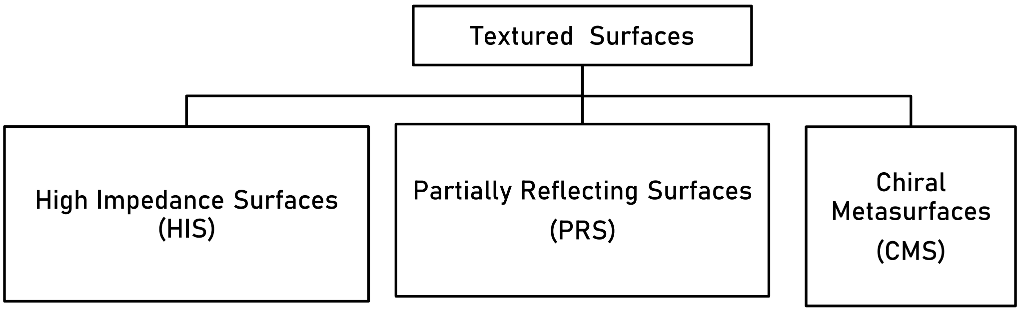

Fig. 1.1. The three main branches of texture surfaces that will be the discussed in the dissertation.

Another special case of textured surfaces having periodicity along only one direction will be discussed. These are the Spoof Surface Plasmon Polaritons (SSPP) structures, and they also possess some interesting properties worth discussing.

1.1.1 Dimensional Constraints

In their book titled *Electromagnetic Metamaterials: Transmission Line Theory and Microwave Applications* [2], Caloz and Itoh define a metamaterial as a material which is **effectively homogeneous**. This means that the cell size and the periodicity of the MM are much smaller than wavelengths of the incident electromagnetic waves at the operating frequencies. The same condition also holds true for MSs. In effectively homogeneous media, the refractive phenomena are predominant when compared to the scattering/diffraction phenomena. Such a medium can be described in terms of an effective permittivity ε_{eff} and an effective permeability μ_{eff}. Once ε_{eff} and μ_{eff} have been defined, the medium can then be described by the effective surface impedance $Z_s = \sqrt{\mu_{eff}/\varepsilon_{eff}}$. The effective parameters depend upon the nature of the unit cell constituting the medium. Therefore, by changing and adjusting the unit cell geometry, the effective parameters can be changed, which in turn changes the properties of the medium itself. Therefore, metamaterials and metasurfaces derive their properties from the nature of their unit cells.

1.1.2 Advantage of Periodicity

Consider an arbitrary infinite 1D periodic structure as shown in Fig. 1.2. It has a periodicity d in the z-direction.

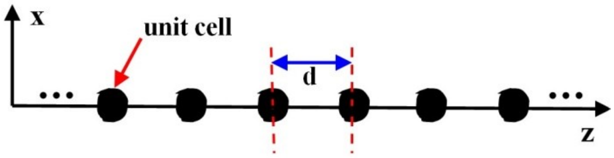

Fig. 1.2. Arbitrary periodic structure having periodicity in the z-direction.

Any EM field component in this structure can be described as

$$\psi(x, y, z + nd) = e^{-jk_{z0}nd}\psi(x, y, z) \tag{1.1}$$

where k_{z0} is the complex phase shift between neighbouring cells and is given by $k_{z0} = \beta - j\alpha$ with β = propagation constant and α = attenuation constant. Equation 1.1 is often called the periodic boundary condition (PBC). The component of the field satisfying (1.1) can also be described as

$$\psi(x,y,z) = e^{-jk_{z0}z}P(x,y,z) \tag{1.2}$$

where *P(x, y, z)* is a periodic function which depends upon the periodicity of the concerned structure such that *P(x, y, z) = P(x, y, z + d)*. Equation 1.2 tells us that the wave passing through a periodic structure gets modulated by the periodic function *P(x, y, z)*. Now, utilizing the fact that *P* is a periodic function, it can be expressed as a Fourier series and written as

$$P(x,y,z) = \sum_{n=-\infty}^{\infty} a_n(x,y)e^{-j\frac{2\pi n}{d}z} \tag{1.3}$$

where a_n = Fourier series coefficients describing the fields in the x- and y-directions. Using (1.2) and (1.3), the field can be represented as

$$\psi(x,y,z) = \sum_{n=-\infty}^{\infty} a_n(x,y)e^{-jk_{zn}z} \tag{1.4}$$

where

$$k_{zn} = k_{z0} + \frac{2\pi n}{d}; \quad n = 0, \pm 1, \pm 2, ... \tag{1.5}$$

Equation 1.4 and 1.5 together constitute the mathematical representation of the *Bloch-Floquet Theorem* used for the analysis of periodic structures. This states that in a periodic structure the wave consists of a superposition of an infinite number of plane waves which have come to be known as *spatial harmonics*. The *fundamental wave* is the wave corresponding to $n = 0$. For positive n, we have the positive spatial harmonics and for negative n, we have the negative spatial harmonics. The Bloch-Floquet theorem is a powerful tool to analyze periodic structures since they suggest that the entire periodic structure can be analyzed simply by studying a unit cell after applying the necessary PBCs on its boundaries.

While it is true that MSs are made periodic in nature, their unique properties do not depend on the periodicity. In fact, Caloz and Itoh demonstrate in [2] that even aperiodic MSs can exhibit properties similar to periodic MSs. The reason is because MSs operate at wavelengths where the periodicity and unit cell size are both << λ where only the fundamental Bloch-Floquet wave is predominant. Suppressing the periodicity suppresses the different spatial harmonics while leaving behind the fundamental mode. However, since the MS predominantly operates in this fundamental mode region, its properties do not change drastically.

The properties of the MS depend mainly on the unit cell geometry and nature rather than the periodicity. The introduction of periodicity *is more of a convenience than a necessity*. Making the MS periodic helps immensely with the analysis since the resulting periodic MS can be very easily analyzed using the *Bloch-Floquet Theorem*. This reduces a lot of computational load. A non-uniform MS is much more difficult to analyze.

1.1.3 Unique Properties and Uses of Textured Surfaces

Textured surfaces possess a lot of interesting and unique properties which make them valuable assets in the domain of electromagnetic engineering. Some of the properties and uses of the textured surfaces presented in Fig. 1.1 will now be discussed briefly.

A. High Impedance Surfaces

Sievenpiper High Impedance Surfaces (HIS) [3] can act as Artificial Magnetic Conductors (AMCs) providing in-phase reflection [4] (in-phase reflection means that after reflection from the HIS, the initial phase of the incident wave is still preserved and no additional phase is added by the reflection phenomenon.) and/or Electromagnetic Band-gap (EBG) structures which result in surface wave suppression [5]. They can be used to design filters [6], phase shifters [7] as well as quasi-TEM waveguides [8], which have near uniform E-field distributions across the waveguide aperture.

B. Partially Reflecting Surfaces

Partially reflecting surfaces are utilized to design Fabry-Pérot Cavities (FPCs) [9]. An FPC is a cavity consisting of two walls. One of the walls is a conducting sheet which completely reflects the incident EM waves while the other is a PRS which mostly reflects the incident EM wave while also allowing a small fraction to be transmitted through it. The EM waves escaping this cavity are highly directive in nature. When an antenna is placed inside an FPC and the FPC resonance is designed to match the antenna resonance, the radiated waves from the antenna exiting the FPC are highly directive in nature. This phenomenon is used to design highly directive antenna systems [10]. The operating principle of the FPC will be discussed explicitly in Chapter 3.

C. Chiral Metasurfaces

CMSs can rotate the polarization plane of an incident EM wave. They are used mainly to design polarization rotators [11]. If certain symmetries of the unit cell are broken, CMSs can also perform an interesting phenomenon called asymmetric transmission (AT) of linearly polarized (LP) incident EM waves [12]. The essence of AT is the difference between the forward and backward cross-polarized transmission coefficients of a structure. This can be utilized to create direction of propagation dependent polarization rotators [13]. It should be noted however that the AT property is reciprocal in nature. More about this will be discussed in Chapter 3.

D. Spoof Surface Plasmon Polaritons

“Spoof” SPP [14] is very similar to the Surface Plasmon Polariton (SPP), which is a type of surface wave observed at optical and ultraviolet frequencies on metal-dielectric interfaces, and can be obtained by using 1D periodic structures. By adjusting the geometry of the periodic structures, the SSPPs can be made to exist even at microwave frequencies where normal SPPs do not exist. They are a type of TM surface wave and are confined very close to the surface while decaying exponentially in both directions away from the surface. This high field confinement property can be used to reduce crosstalk between adjacent components in a system. The SSPPs also have a much shorter wavelength compared to the free-space wavelength. This property can be used to design miniaturized circuits [15].

1.2 Motivation of the Thesis

Textured surfaces are used with antennas, in microwave circuits as well as for wave-front engineering. They have been an area of extensive research for decades and continue to be so even to this day.

In this thesis, we study and analyze such textured surfaces to better understand the underlying principles of the various unique characteristics they possess. Through analysis, these properties can then be exploited to create practical antennas and microwave systems which can prove to be useful in daily applications and which will ultimately benefit the electromagnetic society.

The chapters 4 through 9 are not inter-related since the main aim of this thesis is to investigate different types of textured surfaces and find practical applications which require their usage.

1.3 Organization of the Thesis

The remainder of this dissertation is divided the following chapters:

Chapter 2. *Literature Review* **–** The second chapter provides a literature survey report highlighting the works that have been presented by researchers throughout the ages. This literature survey acts as the foundation of the dissertation.

Chapter 3. *Analyzing the Textured Surfaces* **–** The third chapter analyzes each of the four textured surfaces and explains the origins of their unique properties.

Chapter 4. *A Dual-band AMC Reflector with UHF-RFID Reader***–** In this chapter, a practical UHF-RFID reader system is presented. It consists of a dual-band circularly polarized antenna and a dual-band AMC reflector.

Chapter 5. *An AMC having very high Angular Stability* **–** This chapter presents an AMC which has an angular stability of 88^0. This means that the operating frequency of the AMC remains fixed even for an incident angle of 88^0.

Chapter 6. *FPC Antenna with AMC ground and Reduced Cavity Height* **–** A PRS is used to create a dual-band Fabry-Pérot Cavity Antenna (FPCA). To reduce the cavity height, an AMC ground plane is used instead of a metal ground plane. The details and properties of this FPCA are discussed in this chapter.

Chapter 7. *A Multiband Multifunctional Chiral Metasurface* **–** In this chapter, an ultrathin double layered CMS is presented. It can perform both symmetric as well as asymmetric transmission of incident LP waves within different frequency bands. It can also perform asymmetric LTC polarization conversion. All the operational bands can be tuned to meet user specifications.

Chapter 8. *A Multiband Meta-Mirror* **–** An ultrathin CMS is designed which can act as a meta-mirror within five frequency bands. A meta-mirror is a mirror which does not change the handedness of an incident CP wave with respect to an observer after reflection.

Chapter 9. ***A Tri-band SSPP based End-fire Antenna*****–** In the penultimate chapter, an SSPP based antenna is presented. It exhibits end-fire radiation within three frequency bands. It can also perform beam scanning within the third band. The design and characteristics of the antenna are discussed in the chapter.

Chapter 10. ***Conclusions*** **–** In the final chapter, the main contributions of the thesis are summarized, and future scopes of research are discussed.

REFERENCES

[1] S. A. Ramakrishna, “Physics of negative refractive index materials,” *Rep. Prog. Phys.* vol. 68, pp. 449-521, 2005.

[2] C. Caloz, T. Itoh, *Electromagnetic Metamaterials: Transmission Line Theory and Microwave Applications,* 1st ed., Wiley-IEEE Press, 2005.

[3] D. Sievenpiper, Z. Lijun, R. F. Broas, N. G. Alexopoulos, and E. Yablonovitch, “High impedance electromagnetic surfaces with a forbidden frequency band,” *IEEE Trans Microw. Theory Tech.*, vol. 47, no. 11, pp. 2059–2074, Nov. 1999.

[4] M. Li, Q. L. Li, B. Wang, C. F. Zhou, and S. W. Cheung, “A low-profile dual-polarized dipole antenna using wideband AMC reflector,” *IEEE Trans. Ant. Propag.*, vol. 66, no. 5, pp. 2610–2615, May 2018.

[5] E. Rajo-Iglesias, O. Quevedo-Teruel, and L Inclan-Sanchez, “Mutual coupling reduction in patch antenna arrays by using a planar EBG structure and a multilayer dielectric substrate,” *IEEE Trans. Ant. Propag.*, vol. 56, no. 6, pp. 1648–1655, Jun. 2008.

[6] M. S. Sorkherizi and A. A. Kishk, “Completely tuned coupled cavity filters in defected bed of nails cavity,” *IEEE Trans. Compon., Packag., Manuf. Technol.*, vol. 6, no. 12, pp. 1865–1872, Dec. 2016.

[7] H. Xin, J. B. West, J. C. Mather, J. P. Doane, J. A. Higgins, H. Kazemi, and M. J. Rosker, “A two dimensional millimetre wave phase scanned lens utilizing analog electromagnetic crystal (EMXT) waveguide phase shifters,” *IEEE Trans. Ant. Propag.*, vol. 53, no. 1, pp. 151–158, Jan. 2005.

[8] Fei-Ran Yang, Kuang-Ping Ma, Yongxi Qian, and Tatsuo Itoh, “A novel TEM waveguide using uniplanar compact photonic-bandgap (UC-PBG) structure,” *IEEE Trans Microw. Theory Tech.*, vol. 47, no. 11, pp. 2092–2098, Nov. 1999.

[9] G. V. Trentini, “Partially reflecting sheet arrays,” *IRE Transactions on Antennas and Propagation*, vol. AP-4, no. 4, pp. 666–671, 1956.

[10] J. Mu, H. Wang, H. Wang, Y. Huang, “Low-RCS and gain enhancement design of a novel partially reflecting and absorbing surface antenna,” *IEEE Antennas and Wireless Propagation Letters,* vol. 16, pp. 1903–1906, 2017.

[11] V. S. Asadchy, A. Díaz-Rubio, and S. A. Tretyakov, “Bianisotropic metasurfaces physics and applications,” *Nanophotonics,* vol. 7, no. 6, pp. 1069–1094, 2018.

[12] C. Huang, Y. Feng, J. Zhao, Z. Wang, and T. Jiang, “Asymmetric electromagnetic wave transmission of linear polarization via polarization conversion through chiral metamaterial structures,” *Phys. Rev. B*, vol. 85, 195131, 2012.

[13] A. S. Schwanecke, V. A. Fedotov, V. V. Khardikov, S. L. Prosvirnin, Y. Chen, and N. I. Zheludev, “Nanostructured metal film with asymmetric optical transmission,” *Nano Lett.,* vol. 8, no. 9, pp. 2940–2943, 2008.

[14] J. B. Pendry, L. Martín-Moreno, F. J. Garcia-Vidal, “Mimicking surface plasmons with structured surfaces,” *Science*, vol. 305, 5658, pp. 847-848, 2004.

[15] Z-C. Hao, J. Zhang, L. Zhao, “A compact leaky-wave antenna using a planar spoof surface plasmon polariton structure,” *Int. J. RF Microwave Comput. Aided Eng.,* vol. 29, no. 5, e21617, 2019.

CHAPTER 2

LITERATURE REVIEW

In this chapter, the available literature on the four different types of textured surfaces discussed in Chapter 1 will be reviewed. The chapter is divided into four main sections. Sections 2.1, 2.2, 2.3 and 2.4 review the available literature on HISs, FPCs using PRS, CMSs and SSPPs respectively.

2.1 HIS

Since its inception in 1999 [1], a lot of research has been conducted on the high impedance surfaces. They have been designed for frequencies as low as 25MHz (High Frequency; HF band) [2] as reflectors in wireless power transfer (WPT) applications. An HIS surface designed to work at 263MHz (Very High Frequency; VHF band) can be found in [3]. A polarization dependent HIS surface is used as a reflector at 500MHz (Ultra High Frequency; UHF band) [4] for RF energy harvesting application. HIS structures designed in the UHF band are also found [5, 6]. While most HISs work within the upper UHF and SHF (Super High Frequency) bands (1-30GHz) [7-12], they have also been designed for 60GHz, [13, 14] which lies within the EHF (Extremely High Frequency; millimeter-wave) band (30-300GHz). Theoretically, the HIS maintains its functionality for both very low as well as very high frequencies. From a practical standpoint, as the frequency decreases (approaching the kHz range), the size of the HIS structure will increase substantially since it contains an array of multiple unit cells. If not properly miniaturized (by increasing the capacitance and/or inductance), the resulting structure will be very large in size. As the frequency increases (approaching the THz range), the size of the HIS structure will continue decreasing and after a certain point, the fabrication process of the individual unit cells will become difficult and expensive. High Impedance Surfaces usually contain periodic patches on a grounded dielectric substrate with metallic vias connecting the patches to the ground plane.

Let us consider that an HIS surface is lying in the xy plane and a plane wave is normally incident on it from the +z direction. The *E*-field of the incident wave might have a number of different orientations. It might be oriented towards the +x direction (E_x) or the +y direction (E_y) or any direction in between. If the response of the HIS surface remains the same for all incident *E*-field orientations, then it is called a polarization independent HIS surface. However, if the response of the HIS is dependent on the *E*-field orientation, then it is called a polarization dependent HIS surface [15-19]. Polarization dependence can be brought about by using rectangular patches in a square lattice [15], [19], by offsetting the position of the metallic vias or by utilizing more than one metallic via [16, 17]. Polarization dependent HIS surfaces have been used as polarization rotation/polarization conversion surfaces since they can be used to control the phase difference between the reflected phases of E_x and E_y. In [15], a horizontal dipole is placed over a polarization dependent HIS to achieve circular polarization while in [16], three different polarization states of the horizontal dipole (LHCP, RHCP and linear) are achieved by simply changing the orientation of the dipole above the polarization dependent HIS.

The AMC (in-phase reflection) property of the HIS is used to design electromagnetic reflectors, which when used with antenna systems reduce the antenna profile height and achieve a more compact antenna design [7], [9], [20-23]. This reflection mechanism is discussed elaborately in Chapter 3.

When microstrip antenna arrays are designed on grounded dielectric, surface waves which propagate along the dielectric surface cause the mutual coupling to increase between adjacent elements of the array. This leads to performance degradation of the array. The surface wave suppression property of the HIS is used to reduce this mutual coupling between the adjacent elements of such arrays [24-27].

The idea of designing a surface that reflects the impinging incident wave in-phase and counter-phase at the same time was proposed in [28]. This was achieved by using a combination of metallic cells and AMC cells. This resulted in destructive interference in the boresight direction. The incident energy will be reflected in other directions depending upon the design, thereby reducing the RCS of the object. The combination of the PEC and AMC are arranged in such a way that every PEC unit cell is surrounded by AMC unit cells and vice-versa. The resulting structure looks very similar to a checkerboard design and hence these types of surfaces are known as “Checkerboard AMC” surfaces. Significant RCS reduction has been achieved when the phase difference between the two elements is within the range $180^0 \pm 37^0$ and the directions of the scattered lobes can be found using array theory. It was later shown that the by replacing the PEC element by a different AMC element, the 10dB RCS reduction bandwidth (BW) can be further improved [29-33]. In [32], authors have further improved the RCS reduction BW by using a “blended” checkerboard surface. The simplest form of such a surface consists of two different AMC elements where one AMC element is single band while the other AMC element is dual band.

Impedance waveguides are rectangular waveguides with HIS as the sidewalls. These HIS can also be tunable in some cases. The HIS usually contains square patch Sievenpiper mushrooms with metallic vias. However, the HIS design can be varied and even the vias can be removed for some cases. Varactors can be connected between the HIS unit cells for tunability. Such waveguides show many interesting properties. In oversized impedance waveguides, mode hopping occurs; in single mode impedance waveguides, multi mode propagation occurs and in below cut-off impedance waveguides, forward as well as backward wave propagation occurs. Such properties are discussed in detail in [34] where the authors also provide an analytical model predicting the response of the impedance surface even for oblique incidences. Impedance waveguides can be used to design quasi-TEM waveguides [35], phase shifters [36, 37], filters [38] and feed quasi-optic amplifier arrays [39].

High-speed digital systems use hundreds of gates that switch simultaneously. However, a degradation of the signal occurs when the noise produced by the simultaneous switching of these gates approaches the noise tolerance of static CMOS circuits. Each digital gate on a printed circuit board (PCB) is usually connected between two power planes representing the power supply V_{DD} and the reference plane. The simultaneous switching noise (SSN) becomes acute when the noise generated by the active devices contains dominant frequency harmonics that fall within the resonant modes of the power planes. Therefore, to mitigate this SSN, the power plane resonance must be reduced. The resonance of parallel plates is usually reduced by connecting a combination of a decoupling capacitor (decap) and a series resistor [40].

However, such arrangements cannot produce sufficient suppression beyond 500MHz for most PCBs due to the dominance of the lead inductance of the capacitors. Therefore, instead of using this method, one of the plates of the power plane pair is replaced with an HIS [40-42]. The band-gap of the HIS helps in SSN mitigation.

Gap waveguide (GW) technology is one of the more recent technologies to utilize high impedance surfaces. A parallel plate waveguide when designed with a PEC top plate and a PMC bottom plate (or vice versa) and separated by a gap $< \lambda/4$ creates a stop-band for all directions in the gap [43]. In practice, the PMC plate can be replaced by an AMC/HIS plate. On placing a conducting section (ridge/groove) in the middle of the PMC region, we get a very confined TEM wave propagation [44]. This wave follows the ridge/groove outline and does not spread to the surrounding regions. GWs have also been used to design quasi-TEM waveguides [45], power splitters [43], [46, 47] and filters [48].

2.2 FPC using PRS

The FPC was first used to increase the directivity of an antenna in 1955 by G. V. Trentini [49]. Since then, numerous high gain FPCAs have been designed by researchers. Although most of the FPCAs are LP in nature, several CP FPCAs are also present [50-53]. The FPCAs presented in [53–55], are operational around 60GHz which falls within the millimeter-wave band.

In general, the PRS used to design the FPC is made of periodic metallic patterns on a dielectric substrate. However, the PRS can also be made using a pure dielectric without any metallic patterns on it. In [56], authors design an all dielectric PRS which has a stair-case profile height and use it to create a compact FPCA with high gain. In [57, 58], the PRSs of the FPCs are made of two thin flat dielectric layers spaced λ/2 apart. Although this increases the total cavity height of the antenna, it also increases the operational bandwidth of the FPCA.

Since the FPCA is inherently a resonant antenna, it has a very narrow frequency band of operation. To increase the operating frequency range, PRS layers which have a positive reflection phase gradient must be used. This ensures that the cavity resonance condition is satisfied within a larger range of frequencies. PRSs with positive reflection phase gradients have been used in [50], [52], [57], [59-61]. Such FPCAs have wide 3dB gain bandwidths.

Sometimes, the PRS is made using an absorbing surface (AS) and a reflective surface (RS). The AS mostly consists of resistors and is used to reduce the radar cross-section (RCS) of the FPCA. Such high gain and low RCS FPCAs are presented in [62, 63]. These antennas can be utilized in stealth applications. In [64], authors use a polarization conversion metasurface on top of the PRS to reduce the RCS while in [65], authors use a metamaterial ground plane for RCS reduction of the FPCA.

Several instances of active reconfigurable FPCAs are also found in literature. In [66], a reconfigurable FPCA is proposed with phase-agile reflection cells placed above the antenna ground plane to tune the operating frequency range from 5.2-5.95GHz. By using tunable HIS or PRS, beam steering can be achieved. Such beam scanning FPCAs are presented in [67-74].

The cavity height of the FPCA can be reduced by controlling the reflection phase of the ground plane. Therefore, using HIS/MMs instead of metallic reflectors can help reduce the cavity height of the FPCA. This has been demonstrated in [75, 76].

While most FPCAs found in literature operate within a single continuous frequency band, some dual-band FPCAs have also been reported [77-81].

2.3 CMS

Metasurfaces (MSs) are the 2D equivalent of metamaterials. They often possess properties which are not found in conventional materials [82]-[84]. They can modify the amplitude, phase as well as the polarization plane of an incident electromagnetic (EM) wave either in reflection [85]-[87] or transmission [88]-[90]. Chiral MSs (CMSs) can rotate the polarization plane of an incident wave.

Polarization converters have found a place in many electromagnetic applications such as antenna design, remote sensing, and imaging [91]. Linear to circular polarization converting (LTC) metasurfaces are sometimes used as partially reflecting surfaces (PRS) to create

circularly polarized (CP) Fabry-Perot cavity antennas with enhanced gain [92], [93]. Cross-polarization converters (CPC) are used to convert horizontally polarized radar antennas to vertically polarized antennas to reduce influence of ground/sea clutter. Dual band and multiband polarization converters are needed for frequency hopping radars.
In 2006, Fedotov *et al.,* [94] brought to light another interesting property possessed by certain MSs which was termed asymmetric transmission (AT). The term AT arises from the fact that the transmission coefficients in the forward and backward directions using an MS are different. For linearly polarized (LP) incident waves, the cross-polarized transmission coefficients in the forward and backward directions are different. It should be noted here that although AT resembles a nonreciprocal response to some extent, it is not truly nonreciprocal in nature. In order to achieve AT of LP incident waves, the MS must have more than one layer. Metasurfaces which exhibit AT for LP incident waves can be used like isolators. For instance, at a certain frequency, a forward incident wave having an x-directed *E*-field component (E_x) is transmitted through the MS and the outgoing wave has a y-directed *E*-field component (E_y). However, a backward incident wave having E_x is not transmitted though the MS at that frequency. Instead, it gets reflected.

Many bi-layered and multilayered MSs can be found in literature which exhibit the AT property [95-113]. The AT phenomenon has been achieved in the microwave [95], [100-104], THz [114, 115], infrared [116, 117] as well as visible [118, 119] frequency regimes. In [120, 121], MSs with broadband AT responses have been studied. While most of the reported structures exhibit the AT property over a single frequency band, MSs which exhibit AT over more than one frequency band can also be found in literature: dual-band [100, 101], [122-124] and triple-band [102, 103].

Metasurfaces with good angular stability have been reported in [95], [103, 104] and [125]. In [125], an angular stability of 70^0 has been achieved, but the CMS only works in a single narrow frequency band and has low transmission efficiency.

2.4 SSPP

Owing to their high field confinement, SSPP based transmission lines have been used to design compact antennas [126-140]. Most of the SSPP based antennas perform frequency dependent beam scanning in the broadside direction [126], [128], [132], [136], [138-139]. In [130], authors propose an SSPP based antenna which can perform continuous beam scanning in the lateral direction. In [135], a circular microstrip patch array is fed by an SSPP based transmission line and the resulting antenna can perform broad-angle beam scanning from the forward direction to the backward direction.

While it is seen that most of the SSPP based antennas radiate in the broadside direction, some end-fire SSPP based antennas have also been reported [129], [133], [137]. In [131], authors designed a bi-directional SSPP based end-fire radiating antenna by loading parasitic strips at the two ends of the SSPP transmission line.

SSPP based transmission lines have been used to design a splitter/combiner [141], circulator [142] and band-pass filter [143]. The concept of the cutoff frequency of the SSPP modes has also been used to design FSSs [144-145] which act as spatial filters. In [146], authors design a capacitor-loaded SSPP based transmission line which provides reconfigurable dispersion control and high selectivity filtering.

2.5 Conclusions

The available literature on the four types of textured surfaces discussed in Chapter 1 has been presented in this chapter. It is seen that a lot of research has been conducted on these textured surfaces and they have been used for a plethora of applications over the years.

REFERENCES

[1] D. Sievenpiper, Z. Lijun, R. F. Broas, N. G. Alexopoulos, and E. Yablonovitch, “High impedance electromagnetic surfaces with a forbidden frequency band,” *IEEE Trans. Microw. Theory Tech.*, vol. 47, no. 11, pp. 2059–2074, Nov. 1999.

[2] J. Wu, B. Wang, W. S. Yerazunis, and K. H. Teo, “Wireless power transfer with artificial magnetic conductors,” in *Proc. IEEE WPTC.,* 2013, pp. 155-157.

[3] D. J. Gregoire, C. R. White, and J. S. Colburn, “Wideband artificial magnetic conductors loaded with non-Foster negative inductors,” *IEEE Ant. Wireless Propag. Lttrs.,* vol. 10, pp. 1586-1589, 2011.

[4] H. Kamoda, S. Kitazawa, N. Kukutsu, and K. Kobayashi, “Loop antenna over artificial magnetic conductor surface and its application to dual-band RF energy harvesting,” *IEEE Trans. Ant. Prop.,* vol. 63, no. 10, pp. 4408-4417, Oct. 2015.

[5] N. M. Mohamed-Hicho, E. Antonino-Davin, M. Cabedo-Fabres, and M. Ferrando-Bataller, “A novel low-profile high-gain UHF antenna using high-impedance surfaces,” *IEEE Ant. Wireless Propag. Lttrs.,* vol. 14, pp. 1014-1017, 2015.

[6] M. E. de Cos, F. Las Heras, and M. Franco, “Design of planar artificial magnetic conductor ground plane using frequency-selective surfaces for frequencies below 1GHz,” *IEEE Ant. Wireless Propag. Lttrs.,* vol. 8, pp. 951-954, 2009.

[7] M. Li, Q. L. Li, B. Wang, C. F. Zhou, and S. W. Cheung, “A low-profile dual-polarized dipole antenna using wideband AMC reflector,” *IEEE Trans. Ant. Propag.*, vol. 66, no. 5, pp. 2610–2615, May 2018.

[8] M. E. de Cos, Y. Alvarez, and F. Las-Heras, “Novel broadband artificial magnetic conductor with hexagonal unit cell,” *IEEE Ant. Wireless Propag. Lttrs.,* vol. 10, pp. 615-618, 2011.

[9] Y. F. Cao, X. Y. Zhang and T. Mo, “Low-profile conical-pattern slot antenna with wideband performance using artificial magnetic conductors,” *IEEE Trans Ant. Propag.*, vol. 66, no. 5, pp. 2210–2218, May 2018.

[10] J. Wu, S. Yang, Y. Chen, S. Qu, and Z. Nie, “A low profile dual-polarized wideband omnidirectional antenna based on AMC reflector,” *IEEE Trans. Ant. Propag.*, vol. 65, no. 1, pp. 368–374, Jan. 2017.

[11] M. E. de Cos, Y. Alvarez, R. C. Hadrig, and F. Las-Heras, “Novel SHF-band uniplanar artificial magnetic conductor,” *IEEE Ant. Wireless Propag. Lttrs.,* vol. 9, pp. 44-47, 2010.

[12] S. M. Hasemi, M. Soleimani, “Artificial magnetic conductors realized by planar array of loaded loop for antenna applications,” in *Proc. EuCAP.,* 2011, pp. 2891-2894.

[13] M. Mavridou, K. Konstantinidis, and A. P. Feresidis, “Continuously tunable mm-wave high impedance surface,” *IEEE Ant. Wireless Propag. Lttrs.,* vol. 15, pp. 1390-1393, 2016.

[14] H. F. Contopanagos, C. A. Kyriazidou, A. P. Toda, F. D. Flaviis, and N. G. Alexopoulos, “On the projection of curved AMC reflectors from physically planar surfaces,” *IEEE Trans. Ant. Prop.,* vol. 63, no. 2, pp. 646-658, Feb. 2015.

[15] F. Yang, and Y. Rahmat-Samii, “A low profile single dipole antenna radiating circularly polarized waves,” *IEEE Trans. Ant. Prop.,* vol. 53, no. 9, pp. 3083-3086, Sep. 2005.

[16] W. Yang, K. Tam, W. Choi, W. Che, and H. T. Hui, “Novel polarization rotation technique based on an artificial magnetic conductor and its application in a low-profile circular polarization antenna,” *IEEE Trans. Ant. Prop.,* vol. 62, no. 12, pp. 6206-6216, Dec. 2014.

[17] S. Ullah, J. A. Flint, and R. D. Seager, “Polarization dependent EBG surface with an inclined sheet via,” in *Proc. 2009 Loughborough Ant. Propag. Conf.,* 2009, pp. 637-640.

[18] W. Yang, W. Che, W. Choi, and K. Tam, “A low-profile circularly polarized dipole antenna using a novel polarization rotation artificial magnetic conductor,” in *Proc. EuMC.,* 2014, pp. 374-377.

[19] F. Yang, and Y. Rahmat-Samii, “Polarization-dependent electromagnetic band gap (PDEBG) structures: designs and applications,” *Microw. Opt. Tech. Lttrs.,* vol. 41, no. 6, pp. 439-444, June 2004.

[20] N. M. Mohamed-Hicho, E. Antonino-Davin, M. Cabedo-Fabres, and M. Ferrando-Bataller, “A novel low-profile high-gain UHF antenna using high-impedance surfaces,” *IEEE Ant. Wireless Propag. Lttrs.,* vol. 14, pp. 1014-1017, 2015.

[21] J. Zhu, S. Li, S. Lao, and Q. Xue, “Wideband low-profile highly isolated MIMO antenna with artificial magnetic conductor,” *IEEE Ant. Wireless Propag. Lttrs.,* vol. 17, no. 3, pp. 458-462, Mar. 2018.

[22] H. H. Tran and I. Park, “A dual-wideband circularly polarized antenna using an artificial magnetic conductor,” *IEEE Ant. Wireless Prop. Lett.*, vol. 15, pp. 950–953, 2016.

[23] D. Feng, H. Zhai, L. Xi, S. Yang, K. Zhang, and D. Yang, “A broadband low-profile circular-polarized antenna on an AMC reflector,” *IEEE Ant. Wireless Prop. Lett.*, vol. 16, pp. 2840–2843, 2017.

[24] F. Yang, and Y. Rahmat-Samii, “Microstrip antennas integrated with electromagnetic band-gap (EBG) structures: a low mutual coupling design for array applications,” *IEEE Trans. Ant. Propag*., vol. 51, no. 10, pp. 2936–2946, Oct. 2003.

[25] M. F. Abedin, and M. Ali, “Effects of a smaller unit cell planar EBG structure on the mutual coupling of a printed dipole array,” *IEEE Ant. Wireless Prop. Lett.*, vol. 4, pp. 274–276, 2005.

[26] Z. Iluz, R. Shavit, and R. Bauer, “Microstrip antenna phased array with electromagnetic bandgap substrate,” *IEEE Trans. Ant. Propag*., vol. 52, no. 6, pp. 1446–1453, Jun. 2004.

[27] E. Rajo-Iglesias, O. Quevedo-Teruel, and L Inclan-Sanchez, “Mutual coupling reduction in patch antenna arrays by using a planar EBG structure and a multilayer dielectric substrate,” *IEEE Trans. Ant. Propag*., vol. 56, no. 6, pp. 1648–1655, Jun. 2008.

[28] M. Paquay, J. Iriarte, I. Ederra, R. Gonzalo, and P. de Maagt, “Thin AMC structure for radar cross-section reduction,” *IEEE Trans. Ant. Propag*., vol. 55, no. 12, pp. 3630–3638, Dec. 2007.

[29] J. C. I. Galarregui, A. T. Pereda, J. L. M. de Falcon, I. Ederra, R. Gonzalo, and P. de Maagt, “Broadband radar cross-section reduction using AMC technology,” *IEEE Trans. Ant. Propag*., vol. 61, no. 12, pp. 6136–6143, Dec. 2013.

[30] W. Chen, C. A. Balanis, and C. R. Birtcher, “Checkerboard EBG surfaces for wideband radar cross section reduction,” *IEEE Trans. Ant. Propag*., vol. 63, no. 6, pp. 2636–2645, Jun. 2015.

[31] D. Sang, Q. Chen, L. Ding, M. Guo and Y. Fu, “Design of checkerboard AMC structure for wideband RCS reduction,” *IEEE Trans. Ant. Propag*., vol. 67, no. 4, pp. 2604–2612, Apr. 2019.

[32] A. Y. Modi, C. A. Balanis, C. R. Birtcher, and H. N. Shaman, “Novel design of Ultrabroadband radar cross section reduction surfaces using artificial magnetic conductors,” *IEEE Trans. Ant. Propag*., vol. 65, no. 10, pp. 5406–5417, Oct. 2017.

[33] J. Xue, W. Jiang, and S. Gong, “Chessboard AMC surface based on quasi-fractal structure for wideband RCS reduction,” *IEEE Ant. Wireless Prop. Lett.*, vol. 17, no. 2, pp. 201–204, Feb. 2018.

[34] O. Luukkonen, C. R. Simovski*,* A. V. Räisänen*,* and S. A. Tretyakov, “An efficient and simple analytical model for analysis of propagation properties in impedance waveguides,” *IEEE Trans. Microw. Theory Tech.*, vol. 56, no. 7, pp. 1624–1632, July. 1999.

[35] Fei-Ran Yang, Kuang-Ping Ma, Yongxi Qian, and Tatsuo Itoh, “A novel TEM waveguide using uniplanar compact photonic-bandgap (UC-PBG) structure,” *IEEE Trans. Microw. Theory Tech.*, vol. 47, no. 11, pp. 2092–2098, Nov. 1999.

[36] J. Aiden Higgins, Hao Xin, A. Sailer, and Mark Rosker "Ka-band waveguide phase shifter using tunable electromagnetic crystal sidewalls," *IEEE Trans. Microw. Theory Tech.*, vol. 51, no. 4, pp. 1281–1288, April. 2003.

[37] H. Xin, J. B. West, J. C. Mather, J. P. Doane, J. A. Higgins, H. Kazemi, and M. J. Rosker, "A two-dimensional millimetre wave phase scanned lens utilizing analog electromagnetic crystal (EMXT) waveguide phase shifters," *IEEE Trans. Ant. Propag.*, vol. 53, no. 1, pp. 151–158, Jan. 2005.

[38] H. Xin, A. Higgins, J. Hacker, M. Kim, and M. Rosker, "Electromagnetic crystal (EMXT) waveguide band-stop filter," *IEEE Microw. Wireless Comp. Lett.*, vol. 13, no. 3, pp. 108–110, Mar. 2003.

[39] J. A. Higgins, M. Kim, J. B. Hacker, and D. Sievenpiper, "The application of photonic crystals to quasi-optic amplifiers," *IEEE Trans. Microw. Theory Tech.*, vol. 47, no. 11, pp. 2139–2143, Nov. 1999.

[40] T. Kamgaing, and O. M. Ramahi, "A novel power plane with integrated simultaneous switching noise mitigation capability using high impedance surface," *IEEE Microw. Wireless Comp. Lttrs.,* vol. 13, no. 1, pp. 21-23, Jan. 2003.

[41] S. Shahparnia and O. M. Ramahi, "Simple and accurate circuit models for high-impedance surfaces embedded in printed circuit boards," in *Proc. IEEE Ant. Propag. Soc. Symp.,* 2004, pp. 3565-3568.

[42] Jie Qin and O. M. Ramahi, "Power plane with planar electromagnetic bandgap structures for EMI reduction in high speed circuits," in *Proc. IEEE Ant. Propag. Soc. Int. Symp.*, 2006, pp. 365-368.

[43] A.Valero-Nogueira*,* M. Baquero*,* J. I. Herranz*,* J. Domenech, E. Alfonso*,* and A. Vila, "Gap waveguides using a suspended strip on a bed of nails," *IEEE Ant. Wireless Prop. Lett.*, vol. 10, pp. 1006–1009, 2003.

[44] P. S. Kildal, A. U. Zaman, E. Rajo-Iglesias, E. Alfonso, A. Valero-Nogueira, "Design and experimental verification of ridge gap waveguide in bed of nails for parallel-plate mode suppression," *IET Microw. Ant. Propag.,* vol. 5, no. 3, pp. 262-270, 2011.

[45] D. C. Li*,* F. Boone*,* M. Bozzi*,* L. Perregrini*,* and K. Wu*,* "Concept of virtual electric/magnetic walls and its realization with artificial magnetic conductor technique," *IEEE Microw. Wireless Comp. Lett.*, vol. 18, no. 11, pp. 743–745, Nov. 2008.

[46] E. Alfonso, M. Baquero, A. Valero-Nogueira, J. I. Herranz, and P. S. Kildal, “Power divider in ridge gap waveguide technology,” in *Proc. EuCAP.*, 2010, pp. 1-4.

[47] H. Raza and Y. Jian, “A low loss rat race balun in gap waveguide technology,” in *Proc. EuCAP.*, 2011, pp. 1230–1232.

[48] D. Sun, and J. Xu, “A novel iris waveguide Bandpass filter using air gapped waveguide technology,” *IEEE Microw. Wireless Comp. Lett.*, vol. 26, no. 7, pp. 475–477, July 2016.

[49] G. V. Trentini, “Partially reflecting sheet arrays,” *IRE Transactions on Antennas and Propagation*, vol. AP-4, no. 4, p. 666–671, 1956.

[50] N. Hussain, M. Jeong, J. Park, and N. Kim, “A broadband circularly polarized Fabry-Perot resonant antenna using a single-layered PRS for 5G MIMO applications,” *IEEE Access*, vol. 7, pp. 42897-42906, 2019.

[51] A. R. Vaidya, R. K. Gupta, S. K. Mishra, and J. Mukherjee, “Right-hand/left-hand circularly polarized high-gain antennas using partially reflecting surfaces,” *IEEE Ant. Wirless. Propag. Lttrs.,* vol. 13, pp. 431-434, 2014.

[52] W. Cao, C. Lv, Q. Wang, Y. Zhao, and X. Yang, “Wideband circularly polarized Fabry-Perot resonator antenna in Ku-band,” *IEEE Ant. Wirless. Propag. Lttrs.,* vol. 18, no. 4, pp. 586-590, April 2019.

[53] M. Akbari, S. Gupta, M. Farahani, A. R. Sebak and T.A. Denidni, “Gain enhancement of circularly polarized dielectric resonator antenna based on FSS superstrate for MMW applications,” *IEEE Trans. Ant. Propag.,* vol. 64, no. 12, pp. 5542-5546, Dec. 2016.

[54] D. Abbou, *et al.*, “High-gain wideband partially reflecting surface antenna for 60GHz systems,” *IEEE Ant. Wirless. Propag. Lttrs.,* vol. 16, pp. 2704-2707, 2017.

[55] H. Attia, M. L. Abdelghani, and T. A. Denidni, “Wideband and high-gain millimeter-wave antenna based on FSS Fabry-Perot cavity,” *IEEE Trans. Ant. Propag.,* vol. 65, no. 10, pp. 5589-5594, Oct. 2017.

[56] A. A. Baba, R. M. Hashmi, K. P. Esselle, and A. R. Weily, “Compact high-gain antenna with simple all-dielectric partially reflecting surface,” *IEEE Trans. Ant. Propag.,* vol. 66, no. 8, pp. 4343-4348, Aug. 2018.

[57] N. Wang, L. Talbi, Q. Zeng, and J. Xu, “Wideband Fabry-Perot resonator antenna with electrically thin dielectric superstrates,” *IEEE Access,* vol. 6, pp. 14966-14973, 2018.

[58] M. A. Al-Tarifi, D. E. Anagnostou, A. K. Amert, and K. W. Whites, “Bandwidth enhancement of the resonant cavity antenna by using two dielectric superstrates,” *IEEE Trans. Ant. Propag.,* vol. 61, no. 4, pp. 1898-1908, April 2013.

[59] A. Lalbakhsh, M. U. Afzal, K. P. Esselle, S. L. Smith, and B. A. Zeb, “Single-dielectric wideband partially reflecting surface with variable reflection components for realization of a compact high-gain resonant cavity antenna,” *IEEE Trans. Ant. Propag.,* vol. 67, no. 3, pp. 1916-1921, Mar. 2019.

[60] Y. Ge, K. P. Esselle, and T. S. Bird, “The use of simple thin partially reflective surfaces with positive reflection phase gradients to design wideband, low-profile EBG resonator antennas,” *IEEE Trans. Ant. Propag.,* vol. 60, no. 2, pp. 743-750, Feb. 2012.

[61] M. Asaadi, I. Afifi, and A. Sebak, “High gain and wideband high dense dielectric patch antenna using FSS superstrate for millimeter-wave applications,” *IEEE Access*, vol. 6, pp. 38243-38250, 2018.

[62] W. Pan, C. Huang, P. Chen, X. Ma, C. Hu, and Z. Luo, “A low-RCS and high-gain partially reflecting surface antenna,” *IEEE Trans. Ant. Propag.,* vol. 62, no. 2, pp. 945-950, Feb. 2014.

[63] J. Mu, H. Wang, H. Wang, and Y. Huang, “Low-RCS and gain enhancement design of a novel partially reflecting and absorbing surface antenna,” *IEEE Ant. Wirless. Propag. Lttrs.,* vol. 16, pp. 1903-1906, 2017.

[64] M. Long, W. Jiang, and S. Gong, “Wideband RCS reduction using polarization conversion metasurface and partially reflecting surface,” *IEEE Ant. Wirless. Propag. Lttrs.,* vol. 16, pp. 2534-2537, 2017.

[65] H. Jiang, Z. Xue, W. Li, W. Ren, and M. Cao, “Low-RCS high-gain partially reflecting surface antenna with metamaterial ground plane,” *IEEE Trans. Ant. Propag.,* vol. 64, no. 9, pp. 4127-4132, Sep. 2016.

[66] A. R. Weily, T. S. Bird, and Y. J. Guo, “A reconfigurable high-gain partially reflecting surface antenna,” *IEEE Trans. Ant. Propag.,* vol. 56, no. 11, pp. 3382-3390, Nov. 2008.

[67] P. Xie, G. Wang, H. Li, and J. Liang, “A dual-polarized two-dimensional beam-scanning fabry-perot cavity antenna with a reconfigurable partially reflecting surface,” *IEEE Ant. Wirless. Propag. Lttrs.,* vol. 16, pp. 2370-2374, 2017.

[68] R. Guzm´an-Quir´os, A. R. Weily, J. L. G´omez-Tornero, and Y. J. Guo, “A Fabry–P´erot antenna with two-dimensional electronic beam scanning,” *IEEE Trans. Antennas Propag.*, vol. 64, no. 4, pp. 1536–1541, Apr. 2016.

[69] A. Ourir, S. N. Burokur, R. Yahiaoui, and A. de Lustrac, “Directive metamaterial-based subwavelength resonant cavity antennas— Applications for beam steering,” *Comptes Rendus Physique*, vol. 10, no. 5, pp. 415–422, 2009.

[70] R. Guzman-Quiros, J. L. Gomez-Tornero, A. R. Weily, and Y. J. Guo, “Electronic full-space scanning with 1-D Fabry–Pérot LWA using electromagnetic band-gap,” *IEEE Antennas Wireless Propag. Lett.*, vol. 11, pp. 1426–1429, Dec. 2012.

[71] W. Xu-Chen, Z. Wen-Sheng, H. Jun, and Y. Wen-Yan, “Reconfigurable terahertz leaky-wave antenna using graphene-based high-impedance surface,” *IEEE Trans. Nanotechnol.*, vol. 14, no. 1, pp. 62–69, Jan. 2015.

[72] S. N. Burokur, G. Piau, G. Sabanowski, and A. de Lustrac, “Active metasurface for low-profile reconfigurable antennas,” in *Proc. 7th Eur. Conf. Antennas Propag. (EUCAP’13)*, 2013, pp. 1649–1652.

[73] H. Moghadas, M. Daneshmand, and P. Mousavi, “MEMS-tunable half phase gradient partially reflective surface for beam-shaping,” *IEEE Trans. Antennas Propag.*, vol. 63, no. 1, pp. 369–373, Jan. 2015.

[74] T. Debogovic, J. Bartolic, and J. Perruisseau-Carrier, “Array-fed partially reflective surface antenna with independent scanning and beamwidth dynamic control,” *IEEE Trans. Antennas Propag.*, vol. 62, no. 1, pp. 446–449, Jan. 2014.

[75] S. Wang, A. P. Feresidis, G. Goussetis, and J. C. Vardaxoglou, “High-gain subwavelength resonant cavity antennas based on metamaterial ground planes,” *IEEE Proc. Microw. Antennas Propag.,* vol. 153, no. 1, pp. 1-5, Feb. 2016.

[76] S. Wang, A. P. Feresidis, G. Goussetis, and J. C. Vardaxoglou, “Low-profile resonant cavity antenna with artificial magnetic conductor ground plane,” *IET Electronics Letters,* vol. 40, no. 7, April 2004.

[77] B. A. Zeb, Y. Ge, K. P. Esselle, *et al.*, “A simple dual-band electromagnetic band gap resonator antenna based on inverted reflection phase gradient,” *IEEE Transactions on Antennas and Propagation*, vol. 60, no. 10, pp. 4522–4529, 2012.

[78] M. L. Abdelghani, H. Attia, T. A. Denidni, “Dual- and wideband Fabry-Pérot resonator antenna for WLAN applications,” *IEEE Antennas and Wireless Propagation Letters*, vol. 16, pp. 473–476, 2017.

[79] F. Meng, S. K. Sharma, “A dual-band high-gain resonant cavity antenna with a single layer superstrate,” *IEEE Transactions on Antennas and Propagation*, vol. 63, no. 5, pp. 2320–2325, 2015.

[80] E. B. Lima, J. R. Costa, C. A. Fernandes, “Multiple-beam focal-plane dual-band Fabry-Pérot cavity antenna with reduced beam degradation,” *IEEE Transactions on Antennas and Propagation*, vol. 67, no. 7, pp. 4348–4356, 2019.

[81] J. Chen, Y. Zhao, Y. Ge, *et al*., “Dual-band high-gain Fabry- Pérot cavity antenna with a shared aperture FSS layer,” *IET Microwaves, Antennas and Propagation*, vol. 12, no. 13, pp. 2007–2011, 2018.

[82] F. Aieta *et al.,* “Aberration-free ultrathin flat lenses and axicons at telecom wavelengths based on plasmonic metasurfaces,” *Nano Lett.,* vol. 12, pp. 4932-4936, 2012.

[83] H. T. Chen, A. J. Taylor, and N. Yu, “A review of metasurfaces: Physics and applications,” *Rep. Prog. Phys.,* vol. 79, no. 7, 076401, 2016.

[84] R. X. Ning, J. Zheng, and J. Bao, “Multi-band and wide-band electromagnetically induced transparency in grapheme metasurface of composite structure,” *IET Microw. Ant. Propag.,* vol. 12, no. 3, pp. 380-384, Feb, 2018.

[85] Z. Lei and T. Yang, “Converting state of polarization with a miniaturized metasurface device,” *IEEE Photon. Technol. Lett.*, vol. 29, no. 7, pp. 615–618, Apr. 1, 2017.

[86] T. Cai, G.-M. Wang, X.-L. Fu, J.-G. Liang, and Y.-Q. Zhuang, “High efficiency metasurface with polarization-dependent transmission and reflection properties for both reflectarray and transmitarray,” *IEEE Trans. Antennas Propag.*, vol. 66, no. 6, pp. 3219–3224, Jun. 2018.

[87] X. Huang, H. Yang, D. Zhang, and Y. Luo, “Ultrathin dual-band metasurface polarization converter,” *IEEE Trans. Ant. Propag.,* vol. 67, no. 7, pp. 4636-4641, July 2019.

[88] A. K. Fahad, *et al.*, “Triple-wide-band ultra-thin metasheet for transmission polarization conversion,” *Sci. Rep.,* vol. 10, no. 10, pp.1–12, 2020.

[89] A. K. Baghel, S. S. Kulkarni, and S. K. Nayak, “Linear-to-coss-polarization transmission converter using ultrathin and smaller periodicity metasurface,” *IEEE Antennas Wireless Propag. Lett.*, vol. 18, no.7, pp. 1433–1437, July 2019.

[90] Z. Tao, X. Wan, B. C. Pan, and T. J. Cui, “Reconfigurable conversions of reflection, transmission, and polarization states using active metasurface,” *Appl. Phys. Lttr.,* vol. 110, no. 12, 121901, 2017.

[91] J. Li, J. Feng, B. Li, H. Shi, A. Zhang, and J. Chen, “Dual-Band transmissive cross-polarization converter with extremely high polarization conversion ratio using transmitarray,” *Materials*, vol. 12, no. 11, p. 1827, Jun. 2019.

[92] L. Zhang, C. Liu, C. Ni, M. Kong, and X. Wu, “Low-RCS, circular polarization, and high-gain broadband antenna based on mirror polarization conversion metasurfaces,” *Int. J. Antenn. Propag.*, 6098483, 2019.

[93] J. Ren, W. Jiang, K. Zhang, and S. Gong, “A high-gain circularly polarized Fabry–Perot antenna with wideband low-RCS property,” *IEEE Ant. Wireless Propag. Lett.,* vol. 17, no. 5, pp. 853–856, 2018.

[94] V. A. Fedotov, P. L. Mladyonov, S. L. Prosvirnin, A. V. Rogacheva, Y. Chen, and N. I. Zheludev, “Asymmetric propagation of electromagnetic waves through a planar chiral structure,” *Phys. Rev. Lett,. v*ol. 97, no.16, pp. 167401–167404, 2006.

[95] M. I. Khan *et al.,* “Efficient asymmetric transmission for wide incidence angle using bi-layered chiral metasurface,” *J. Phys. D Appl. Phys.,* vol. 53, no. 30, 305004, 2020.

[96] A. S. Schwanecke, V. A. Fedotov, V. V. Khardikov, S. L. Prosvirnin, Y. Chen, and N. I. Zheludev, “Nanostructured metal film with asymmetric optical transmission,” *Nano Lett,.* vol. 8, no. 9, pp.2940–2943, 2008.

[97] E. Plum, V. A. Fedotov, and N. I. Zheludev, “Planar metamaterial with transmission and reflection that depend on the direction of incidence,” *Appl. Phys. Lett.*, vol. 94, no. 13, 131901, 2009.

[98] R. Zhao, H. Y. Chen, L. Zhang et al., “Design and implementation of high efficiency and broadband transmission-type polarization converter based on diagonal split-ring resonator,” *Prog. Electromagn. Res.,* vol. 161, pp. 1–10, 2018.

[99] C. Huang, Y. Feng, J. Zhao, Z. Wang, and T. Jiang, "Asymmetric electromagnetic wave transmission of linear polarization via polarization conversion through chiral metamaterial structures," *Phys. Rev. B*, vol. 85, 195131, 2012.

[100] M. L. Li *et al.*, "Microwave linear polarization rotator in a bilayered chiral metasurface based on strong asymmetric transmission," *J. Opt.*, vol. 19, no. 7, 075101, 2017.

[101] S. Khan, and T. F. Eibert, "A dual-band metasheet for asymmetric microwave transmission with polarization conversion," *IEEE Access*, vol. 7, pp. 98045–98052, 2019.

[102] D. Liu, Z. Xiao, and Z. Wang, "Multi-band asymmetric transmission and 90^0 polarization rotator based on bi-layered metasurface with F-shaped structure," *Plasmonics*, vol. 12, pp. 445-452, 2017.

[103] M. I. Khan, B. Hu, Y. Chen, N. Ullah, M. J. I. Khan, and A. R. Khalid, "Multiband efficient asymmetric transmission with polarization conversion using chiral metasurface," *IEEE Ant. Wirless Prop. Lttr.,* vol. 19, no. 7, pp. 1137-1141, July 2020.

[104] S. Aisha, M. I. Khan, Y. Chen, B. Hu, and I. Khan, "An efficient chiral polarization rotator with asymmetric transmission for large incidence angles," *Journal of App. Phys.,* vol. 128, 213102, 2020.

[105] T. Cai, G. M. Wang, H. X. Xu, S. W. Tang, H. P. Li, J. G. Liang, and Y. Q. Zhuang, "Bifunctional Pancharatnam-Berry metasurface with high-efficiency helicity-dependent transmissions and reflections," *Ann. Phys.,* vol. 530, no. 1, 1700321, 2018.

[106] F. X. Li, H. Y. Chen, Q. T. He et al., "Design and implementation of metamaterial polarization converter with the reflection and transmission polarization conversion simultaneously," *J. Opt.,* vol. 21, no. 4, 045102, 2019.

[107] Y. Liu, S. Xia, H. Shi, A. Zhang, and Z. Xu, "Efficient dual-band asymmetric transmission of linearly polarized wave using a chiral metamaterial," *Progress In Electromagnetics Research C*, vol. 73, pp. 55–64, 2017.

[108] Y. Cheng, Y. Nie, X. Wang, and R. Gong, "An ultrathin transparent metamaterial polarization transformer based on a twist-split-ring resonator," *Appl. Phys. A*, vol. 111, pp. 209–215, 2013.

[109] F. Mirzamohammadi, J. Nourinia, C. Ghobadi, and R. Naderali, "A dual-wideband bi-layered chiral metamaterial to develop cross-polarization conversion and asymmetric

transmission functionalities for the linearly polarized electromagnetic waves," *AEU - Int. J. Electron. Commun.,* vol. 111, 152916, 2019.

[110] M. Kim, K. Yao, G. Yoon, I. Kim, Y. M. Liu, and J. Rho, "A broadband optical diode for linearly polarized light using symmetry-breaking metamaterials," *Adv. Opt. Mater.*, vol. 5, 1700600, 2017.

[111] De-jun Liu, Zhong-yin Xiao, Xiao-long Ma, Quan-wen Ma, Xiao-xue Xu, Zi-hua Wang, "Asymmetric transmission of chiral metamaterial slab with double L resonators," *Optics Comm.*, vol. 338, pp. 359-365, 2015.

[112] D. Liu, Z. Xiao, X. Ma, L. Wang, K. Xu, J. Tang, Z. Wang, "Dual-band asymmetric transmission of chiral metamaterial based on complementary U-shaped structure," *Appl. Phys. A,* vol. 118**,** pp. 787–791, 2015.

[113] L. Stephen, N. Yogesh, and V. Subramanian, "Broadband asymmetric transmission of linearly polarized electromagnetic waves based on chiral metamaterial," *J. Appl. Phys.,* vol. 123, 033103, 2018.

[114] R. H. Fan *et al*., "Freely tunable broadband polarization rotator for terahertz waves," *Advanced Materials*, vol. 27, no. 7, pp.1201-1206, 2015.

[115] J. Zhao, J. Song, T. Xu, T. Yang, and J. Zhou, "Controllable linear asymmetric transmission and perfect polarization conversion in a terahertz hybrid metal-graphene metasurface," *Opt. Express*, vol. 27, no. 7, pp. 9773–9781, 2019.

[116] G. Kenanakis, A. Xomalis, A. Selimis, M. Vamvakaki, M. Farsari, M. Kafesaki,C.M. Soukoulis, and E.N. Economou, "Three-dimensional infrared metamaterial with asymmetric transmission," *ACS Photonics*, vol. 2, no. 2, pp.287-294, 2015.

[117] Z. Li *et al*., "Broadband diodelike asymmetric transmission of linearly polarized light in ultrathin hybrid metamaterial," *Appl Phys Lett.,* vol. 105, no. 20, 201103, 2014.

[118] V. A. Fedotov, A. S. Schwanecke, N. I. Zheludev, V. V. Khardikov, and S. L. Prosvirnin, "Asymmetric transmission of light and enantiomerically sensitive plasmon resonance in planar chiral nanostructures," *Nano Lett.,* vol. 7, no. 7, pp.1996–1999, 2007.

[119] S. E. Mun, J. Hong, J. G. Yun, and B. Lee, "Broadband circular polarizer for randomly polarized light in few-layer metasurface," *Sci. Rep.*, vol. 9, no. 1, 2543, 2019

[120] F. M. Mohammadi, J. Nourinia, C. Ghobadi, and M. M. Zadeh, "A bi-layered chiral metamaterial with high-performance broadband asymmetric transmission of linearly polarized wave," *AEU Int. J. Electron. Commun.,* vol. 98, pp. 58–67, 2019.

[121] R. Zhao, H. Y. Chen, L. Zhang, F. Li, P. Zhou, J. Xie, and L.J. Deng, "Design and implementation of high efficiency and broadband transmission-type polarization converter based on diagonal split-ring resonator," *Progr. In Electro Research*, vol. 161, pp.1-10, 2018.

[122] Q. H. Song *et al.*, "Split archimedean spiral metasurface for controllable GHz asymmetric transmission," *Appl. Phys. Lett.*, vol. 114, no. 15, 151105, 2019.

[123] C. Menzel *et al*., "Asymmetric transmission of linearly polarized light at optical metamaterials," *Phys Rev Lett.,* vol. 104, 253902, 2010.

[124] D. Liu, Z. Xiao, X. Ma, and Z. Wang, "Asymmetric transmission of linearly and circularly polarized waves in metamaterial due to symmetry-breaking," *Appl. Phys. Express,* vol. 8, 052001, 2015.

[125] K. Chen *et al*., "Dynamic control of asymmetric electromagnetic wave transmission by active chiral metamaterial," *Sci. Rep.*, vol. 7, 42802, 2017.

[126] Q. Zhang, Q. Zhang, and Y. Chen, "Spoof surface plasmon polariton leaky-wave antennas using periodically loaded patches above PEC and AMC ground planes," *IEEE Ant. Wirless. Propag. Lttrs.,* vol. 16, pp. 3014-3017, 2017.

[127] A. Kandwal, Q. Zhang, X. Tang, L. W. Liu, and G. Zhang, "Low-profile spoof surface plasmon polaritons traveling-wave antenna for near-endfire radiation," *IEEE Ant. Wirless. Propag. Lttrs.,* vol. 17, no. 2, pp. 184-187, Feb. 2018.

[128] X. Liu, B. Chen, J. Zhang, "Frequency-scanning planar antenna based on spoof surface plasmon polariton," *IEEE Ant. Wirless. Propag. Lttrs.,* vol. 16, pp. 165-168, 2017.

[129] X. Du, H. Li, and Y. Yin, "Wideband fish-bone antenna utilizing odd-mode spoof surface plasmon polaritons for endfire radiation," *IEEE Trans. Ant. Propag.,* vol. 67, no. 7, pp. 4848-4853, July 2019.

[130] L. Liu, M. Chen, J. Cai, X. Yin, and L. Zhu, "Single-beam leaky-wave antenna with lateral continuous scanning functionality based on spoof surface plasmon transmission line," *IEEE Access*, vol. 7, pp. 25225-25231, 2019.

[131] W. Feng, Y. Feng, W. Yang, W. Che, and Q. Xue, "High-performance filtering antenna using spoof surface plasmon polaritons," *IEEE Trans. Plasma Sc.*, vol. 47, no. 6, pp. 2832-2837, Jun. 2019.

[132] D. Guan, P. You, Q. Zhang, Z. Lu, S. Yong, and K. Xiao, "A wide-angle and circularly polarized beam-scanning antenna based on microstrip spoof surface plasmon polariton transmission line," *IEEE Ant. Wirless. Propag. Lttrs.,* vol. 16, pp. 2538-2541, 2017.

[133] J. Y. Yin *et al.,* "Endfire radiations of spoof surface plasmon polaritons," *IEEE Ant. Wirless. Propag. Lttrs.,* vol. 16, pp. 597-600, 2017.

[134] D. Tian, R. Xu, G. Peng, J. Li, Z. Xu, A. Zhang, and Y. Ren, "Low-profile high-efficiency bidirectional endfire antenna based on spoof surface plasmon polaritons," *IEEE Ant. Wirless. Propag. Lttrs.,* vol. 17, no. 5, pp. 837-840, May 2018.

[135] J. Y. Yin, "Frequency-controlled broad-angle beam scanning of patch array fed by spoof surface plasmon polaritons," *IEEE Trans. Ant. Propag.,* vol. 64, no. 12, pp. 5181-5189, Dec. 2016.

[136] A. Kianinejad, Z. N. Chen, and C-W Qiu, "A single-layered spoof-plasmon-mode leaky wave antenna with consistent gain," *IEEE Trans. Ant. Propag.,* vol. 65, no. 2, pp. 681-687, Feb. 2017.

[137] L. Liu, M, Chen, and X. Yin, "Single-layer high gain endfire antenna based on spoof surface plasmon polaritons," *IEEE Access*, vol. 8, pp. 64139-64144, 2020.

[138] G. S. Kong, H. F. Ma, B. G. Cai, and T. J. Cui, "Continuous leaky-wave scanning using periodically modulated spoof plasmonic waveguide," *Sci. Rep.,* vol. 6, 29600, pp. 1-9, July 2016.

[139] J. J. Xu, H. C. Zhang, Q. Zhang, and T. J. Cui, "Efficient conversion of surface-plasmon-like modes to spatial radiated modes," *App. Phys. Lttrs.,* vol. 106, 021102, 2015.

[140] Y. Han, S. Gong, J. Wang, Y. Li, Y. Fan, J. Zhang, and S. Qu, "Shared-aperture antennas based on even- and odd-mode spoof surface plasmon polaritons," *IEEE Trans. Ant. Propag.,* vol. 68, no. 4, pp. 3254-3258, Apr. 2020.

[141] S. Zhou *el al.,* "Four-way spoof surface plasmon polaritons splitter/combiner," *IEEE Microw. Wireless Comp. Lttrs.,* vol. 29, no. 2, pp. 98-100, Feb. 2019.

[142] T. Qui, J. Wang, Y. Li, and S. Qu, "Circulator based on spoof surface plasmon polaritons," *IEEE Ant. Wirless. Propag. Lttrs.,* vol. 16, pp. 821-824, 2017.

[143] J. J. Wu *et al.,* “Bandpass filter based on low frequency spoof surface plasmon polaritons,” *IET Electronics Letters,* vol. 48, no. 5, Mar. 2012.

[144] Y. Pang, Y. Li, J. Zhang, Z. Xu, and S. Qu, “Design of frequency selective surface based on spoof surface plasmon polariton modes,” *IEEE Ant. Wirless. Propag. Lttrs.,* vol. 17, no. 6, pp. 1123-1126, Jun. 2018.

[145] C. Wang *et al.,* “Frequency-selective structure with transmission and scattering deflection based on spoof surface plasmon polariton modes,” *IEEE Trans. Ant. Propag.,* vol. 67, no. 10, pp. 6508-6514, Oct. 2019.

[146] X. Tang, Q. Zhang, S. Hu, A. Kandwal, T. Guo, and Y. Chen, “Capacitor-loaded spoof surface plasmon for flexible dispersion control and high-selectivity filtering,” *IEEE Microw. Wireless Comp. Lttrs.,* vol. 27, no. 9, pp. 806-808, Sep. 2017.

CHAPTER 3

ANALYZING THE TEXTURED SURFACES

This chapter provides an analysis of each of the four textured surfaces mentioned in the previous chapter. It will be divided into 4 main sections. Section 3.1 describes the HIS, Section 3.2, describes the PRS, Section 3.3 describes the CMS and Sec. 3.4 describes the SSPP. A conclusion section is added at the end to summarize the contents of the chapter.

3.1 High Impedance Surface - HIS

The High Impedance Surface, abbreviated popularly as HIS, was first introduced to the microwave community by Daniel F. Sievenpiper in 1999 [1]. It possesses unique properties by virtue of its geometry and periodicity which makes it very useful in multiple applications. Ever since its introduction in 1999, the HIS has continued to grow in popularity and usefulness throughout the years.

3.1.1 Analysis

The Sievenpiper HIS consists of a 2D array of metallic patches placed above a metallic ground plane. To make the arrangement robust, the metallic patches are usually placed on a grounded dielectric layer. Each metallic patch is connected to the ground plane by a metallic via (Fig. 3.1). When the *periodicity of this 2D array is much smaller compared to the wavelength of operation*, this whole arrangement can be described using an effective medium model and its qualities can be represented by a single parameter, the *surface impedance* (Z_s).

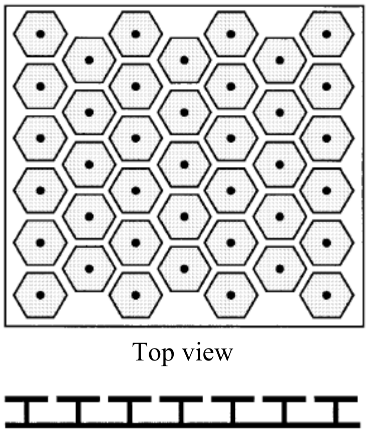

Fig. 3.1. Mushroom type HIS [1].

A. Lumped Equivalent Circuit Model of the HIS

On examining the HIS unit cells, it can be seen that the gap between the neighboring metallic patches gives rise to a *capacitance, C,* while the current along adjacent patches gives rise to an *inductance, L* (Fig. 3.2(a)). The equivalent circuit of the HIS is similar to a parallel RLC circuit (Fig. 3.2(b)). The equivalent surface impedance of the HIS can be written approximately as:

$$Z_s = \frac{j\omega L}{1-\omega^2 LC} \tag{3.1}$$

with a resonance frequency $$\omega_0 = \frac{1}{\sqrt{LC}} \ . \tag{3.2}$$

Similar to parallel RLC circuits, the impedance of the HIS is inductive at low frequencies and capacitive at high frequencies. At resonance ($\omega = \omega_0$), the surface impedance becomes infinite and thus the array of grounded patches exhibits very high impedance.

(a) (b)

Fig. 3.2 (a) Capacitance and inductance of the unit cells and (b) equivalent lumped circuit model.

3.1.2 Unique properties of the HIS

A. Surface wave suppression (EBG Property)

Consider a surface having permittivity ε, permeability μ and surface impedance Z_s placed along the yz plane as shown in Fig. 3.3. There are two types of surface waves which can exist on such an impedance surface. These are the TM (Transverse Magnetic) and TE (Transverse Electric) surface waves.

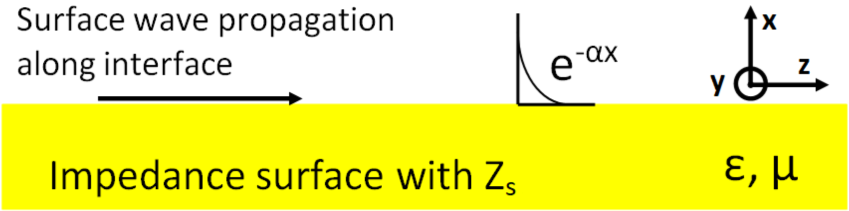

Fig. 3.3. Surface wave propagation along an impedance surface.

They have different field distributions which are illustrated in Fig. 3.4. Both the surface waves will decay exponentially (with decay constant α) away from the surface.

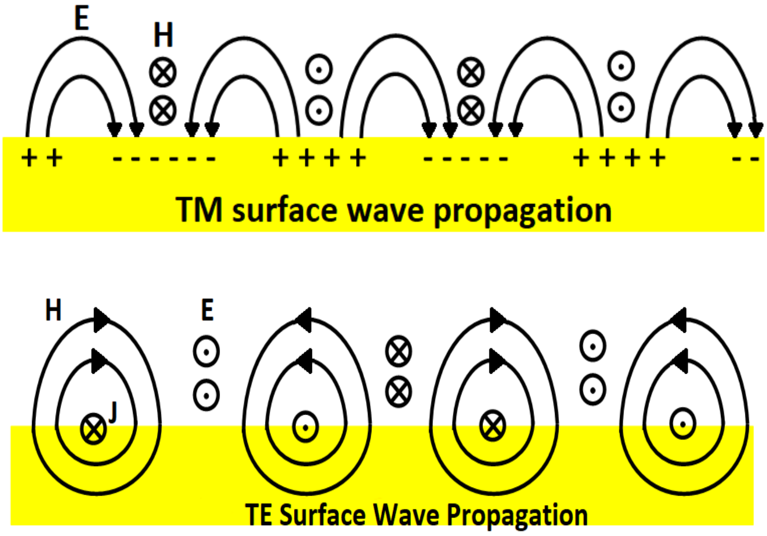

Fig. 3.4. Field arrangements of the TM and TE surface waves propagating along the impedance surface. (J = surface current density)

For TM surface waves ($H_x = H_z = E_y = 0$), the surface impedance of the arbitrary impedance surface turns out to be [1]:

$$Z_s(TM) = \frac{E_z}{H_y} = \frac{j\alpha}{\omega\varepsilon}. \tag{3.3}$$

Similarly, for TE surface waves ($E_x = E_z = H_y = 0$), the surface impedance of the arbitrary impedance surface turns out to be [1]:

$$Z_s(TE) = \frac{-E_y}{H_z} = \frac{-j\omega\mu}{\alpha} . \tag{3.4}$$

From (3.3) and (3.4), it can be seen that an impedance surface can *support a **TM surface wave** only when its surface impedance is **inductive*** while it can *support a **TE wave** only when its surface impedance is **capacitive***.

Revisiting the expression for the surface impedance Z_s of an HIS (equation 3.1), it is clear that the HIS supports TM waves at low frequencies and TE waves at high frequencies. At frequencies near resonance, the surface exhibits very high impedance (ideally infinite) which is modeled as an open circuit. Neither the TM nor the TE surface wave is allowed to propagate within this band of frequencies. The HIS therefore acts as an electronic filter and prevents propagation of surface waves within this “stop-band”. *Thus, an HIS is often referred to as an Electromagnetic Band Gap (EBG) structure.*

To illustrate this stop band, an HIS unit cell (Fig. 3.5) is simulated in CST Microwave Studio and analyzed using the Eigenmode Solver of CST with periodic boundary conditions (PBCs) on all four sides of the plane of the unit cell. The dispersion diagram is shown in Fig. 3.6. The waves located to the left of the light line are fast waves ($\beta < k_0$; β = phase constant of the wave along the HIS and k_0 = vacuum wavenumber). They are weakly bound to the surface and radiate away as leaky waves.

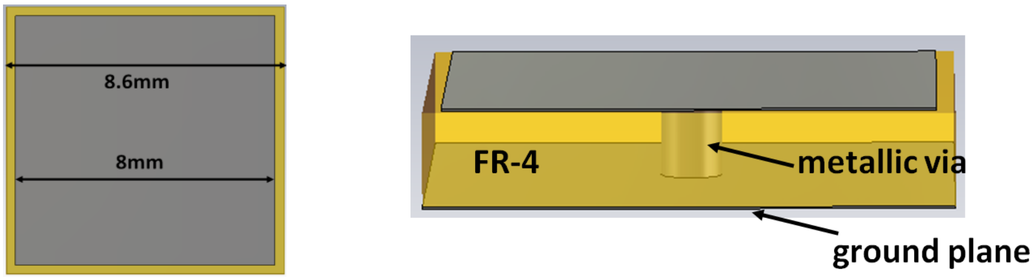

(a) (b)

Fig. 3.5. (a) An HIS unit cell consisting of a square metallic patch on a grounded dielectric substrate. (b) The patch is connected to the ground plane with a metallic via. The substrate used is FR-4 (ε_r=4.3, tanδ =0.02) with a thickness of 1.52mm.

The waves located to the right of the light line are slow waves ($\beta > k_0$) and they are tightly bound to the surface. They propagate along the surface with very little radiation.

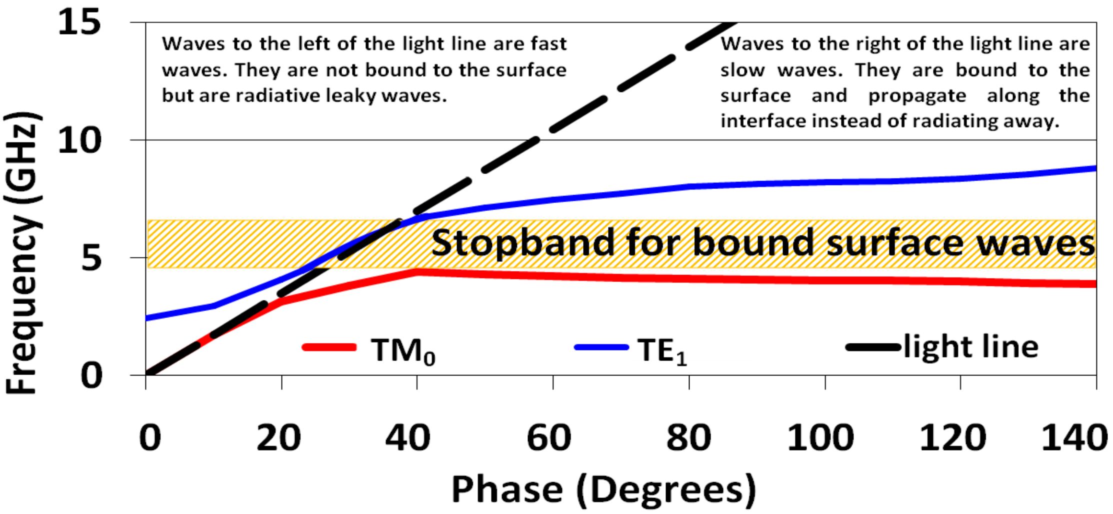

Fig. 3.6. Dispersion diagram of a typical HIS.

The region highlighted in Fig. 3.6 is a frequency band where neither the TM_0 surface wave nor the TE_1 surface wave can propagate along the surface. The portion of the TE_1 surface wave which falls within this stop-band lies to the left of the light line and hence radiates away as a leaky wave with little propagation along the surface.

B. In-phase reflection (AMC Property)

Consider that a plane wave is incident on the impedance surface shown in Fig. 3.3. Near the surface, standing waves are formed by the interactions between the forward wave (incident wave; E_f and H_f) and the backward wave (reflected wave; E_b and H_b). The standing waves can be expressed as:

$$E(x) = E_f e^{-jkx} + E_b e^{-jkx}, \quad H(x) = H_f e^{-jkx} + H_b e^{-jkx}. \tag{3.5}$$

The surface impedance Z_s can be obtained from the boundary condition on the interface (x = 0) as:

$$\frac{E(x=0)}{H(x=0)} = \frac{E_f + E_b}{H_f + H_b} = Z_s . \tag{3.6}$$

However, for both the forward and backward waves, we have

$$\frac{E_f}{H_f} = -\frac{E_b}{H_b} = Z_0 = 377\Omega . \tag{3.7}$$

The reflection phase of such an impedance surface is nothing but the phase difference between the forward and backward waves. This can be expressed as:

$$\phi = \mathrm{Im}\left[\ln\left(\frac{E_b}{E_f}\right)\right]. \tag{3.8}$$

Using (3.6) and (3.7) with (3.8), the final expression for the reflection phase (ϕ) is written as:

$$\phi = \mathrm{Im}\left[\ln\left(\frac{Z_s - Z_0}{Z_s + Z_0}\right)\right]. \tag{3.9}$$

When $|Z_s| = |Z_0|$, the reflection phase crosses ± π/3. When the surface has very high impedance ($Z_s \to \infty$), the reflection phase turns out to be zero. Since an HIS has $Z_s \to \infty$ at resonance, it exhibits a zero reflection phase at resonance. In many papers [2-6], the reflection phase bandwidth of the HIS is defined as the range of frequencies where $-\pi/2 \leq \phi \leq \pi/3$. Some authors [7-9] have also defined this range as $-\pi/4 \leq \phi \leq \pi/4$.

The in-phase reflection property of the HIS is exploited to design reflectors which can be placed very close to antenna systems. For conventional reflectors (which are made using good conductors), the distance between the antenna and the reflector must be $\lambda/4$ (where λ is the wavelength corresponding to the operating frequency of the antenna) in order to achieve constructive interference between the direct wave and the reflected wave. To understand why this happens, let us look at Fig. 3.7(a). The EM wave radiated by the antenna travels in both the forward (towards the right) and backward (towards the left) directions in Fig. 3.7(a). By the time the backward wave reaches the reflector, it has gained an additional phase = $(2\pi/\lambda)*(\lambda/4) = \pi/2$. When it gets reflected by the conductor, a phase shift of $\pm\pi$ is added to it as well. Finally, when this reflected wave reaches the position of the antenna, it again gains a phase = $(2\pi/\lambda)*(\lambda/4) = \pi/2$. Therefore, the total phase gained by the reflected wave = $\pi/2 + \pi/2 \pm\pi$, which is 0 when reflector phase shift is taken to be $-\pi$ and 2π when the reflector phase shift is taken to be $+\pi$. This leads to the constructive interference between the direct and reflected EM waves.

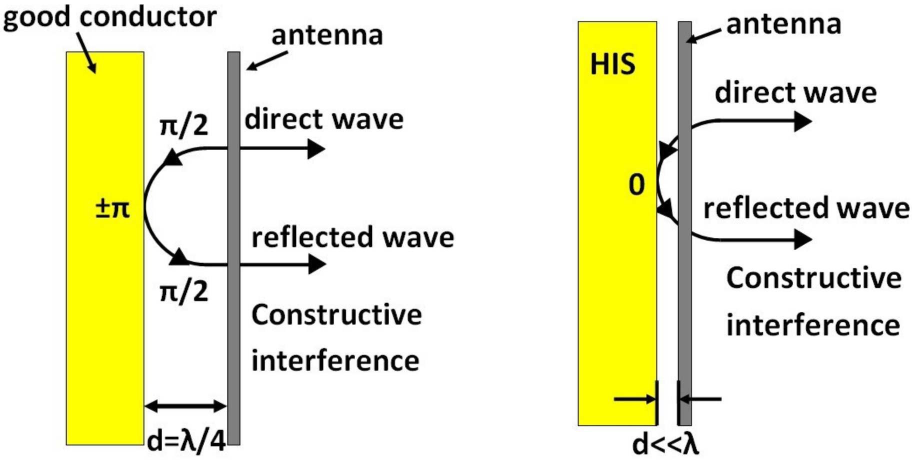

(a) (b)

Fig. 3.7 (a) Antenna with conventional reflector, (b) antenna with HIS reflector.

However, in case of an AMC/ HIS reflector, the phase shift introduced by the reflector = 0^0 at the design frequency. If the reflector is now placed very close to the antenna ($d \ll \lambda$) the reflected wave undergoes a negligible phase shift throughout its round trip. Therefore, the AMC reflector can be placed very close to the antenna and still achieve constructive interference between the direct and reflected wave as shown in Fig. 3.7(b). Using an AMC reflector in place of a conventional reflector leads to an overall reduction in the height of the antenna system. This is also clear from Fig. 3.7.

C. Steps to determine the reflection phase

To analyze the unit cell in CST, periodic boundary conditions (PBCs) are applied on all four sides of the unit cell as shown in Fig. 3.8(a). The two Floquet ports located above and below the unit cell can launch EM plane waves whose electric and magnetic fields are uniform over the unit cell. Since AMC unit cells have a ground plane on the bottom of the substrate, only the information from the upper port of Fig. 3.8(a) is needed to extract the reflection phase of the AMC. Now, the phase reference plane of this arrangement is located somewhere in the space between the upper port and the top surface of the unit cell. So, the location of the AMC unit cell surface and the phase reference plane are different. In order to get the correct value of the AMC reflection phase from this arrangement, a PEC surface, located at the same position as the AMC unit cell, must be used as a reference. The phase reference plane is the same for both the AMC surface as well as the PEC surface. Therefore, we need to perform two simulations separately. For the first simulation, the AMC unit cell is used and the simulated values of the reflection phase ϕ_{AMC} are noted. For the next simulation, the AMC unit cell is replaced by a PEC surface at the same location and the simulated values of the PEC reflection phase ϕ_{PEC} are noted. Finally, to get the actual reflection phase of the AMC unit cell, we use the equation $\phi_{AMC,\ Normalized} = \phi_{AMC} - \phi_{PEC} + 180^0$ [10]. The 180^0 is added to consider the PEC reflection phase. In this way, the propagation phase between the phase reference plane and the AMC surface is cancelled. So, $\phi_{AMC,\ Normalized}$ is the actual phase we are looking for. Even during the measurement process, the fabricated AMC has to be replaced by a metal layer having the same dimensions as the AMC and the reflection phase of the metal layer has to be noted. Then, the above equation has to be utilized to get the normalized AMC phase.

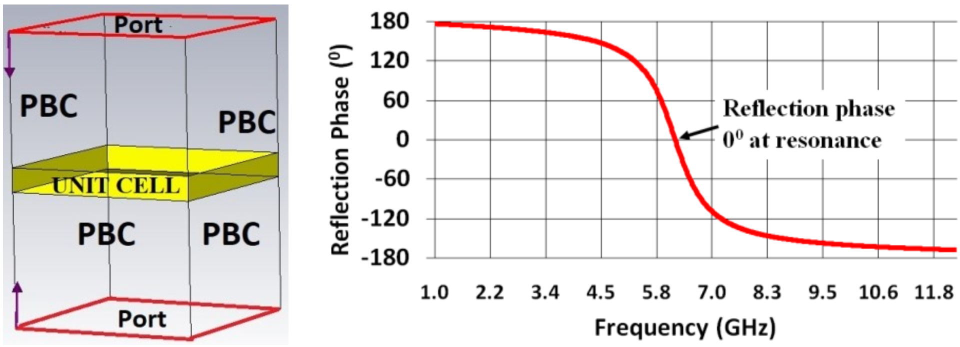

(a) (b)

Fig. 3.8 (a) PBCs and Ports during CST analysis. (b) Reflection phase diagram of the HIS of Fig. 3.5.

To demonstrate the in-phase reflection property, the reflection phase versus frequency curve of the AMC designed in Fig. 3.5 is shown in Fig. 3.8(b). The reflection phase is 0^0 at around 6.2GHz.

A perfect electric conductor (PEC) has zero surface impedance and is similar to a short circuit. It has a reflection phase of $\pm \pi$ and no tangential *E*-field can exist on its surface ($E_{tan} = 0$). Similarly, a perfect magnetic conductor (PMC) has infinite surface impedance and is similar to an open circuit. It has a reflection phase of 0 and no tangential H-field can exist on its surface ($H_{tan} = 0$). Based on these properties, it can be seen that an HIS also acts as a PMC, but only at its resonance frequency. On moving away from the resonance, the reflection phase no longer remains zero, the surface impedance decreases gradually and H_{tan} eventually gains some non-zero value. Since the HIS mimics the PMC only within a definite range of frequencies, it is often called an artificial magnetic conductor (AMC). The properties of the PEC, PMC and AMC are summarized in Table 3.1. It should be noted that the reflection magnitude of the PEC, PMC as well as AMC lie very close to 1 since all three of them are essentially reflectors. The reflected wave of the PEC is completely out of phase with the incident wave while the reflected waves of the PMC and AMC (at resonance) are completely in phase with the incident waves.

Table 3.1. Comparing the PEC, PMC and AMC.

Properties	**PEC**	**PMC**	**AMC**
Surface Impedance	0	∞	very high (at resonance)
Reflection Phase	$\pm \pi$	0	0 (at resonance)
Tangential Fields	$E_{tan} = 0$	$H_{tan} = 0$	$H_{tan} = 0$ (at resonance)

3.1.3 Effects of the metallic vias on the EBG and AMC properties

In [11], George Goussetis et al., study a 2D periodic metallic array of patches printed on a grounded dielectric substrate and show that the AMC and EBG properties of the HIS are influenced by two distinct resonance phenomena. It is the presence of the vias (connecting the metallic patches to the ground plane) that impose an EBG at the same frequency as the AMC property. This statement can be verified by observing the reflection phase diagram (Fig. 3.8) and the dispersion diagram (Fig. 3.6) of the HIS designed in Fig. 3.5. The ± π/2 reflection phase bandwidth lies within 5.6-6.8GHz while the surface wave stop-band lies within 4.5-6.7GHz.

When an array of metallic patches (a Frequency Selective Surface; FSS) is kept close to a ground plane (without any metallic vias), there are two types of resonance phenomena which occur:

i. *Array resonance* –This is similar to the resonance of the FSS in free space where the surface currents excited on the array elements are in phase with the incident wave and the wave reflected by the FSS undergoes a phase reversal. It is responsible for the EBG property.

ii. *Fabry-Pérot type resonance* – This resonance occurs at a different frequency due to the cavity formed between the ground plane and the FSS. It excites much stronger surface currents on the array elements which are not in phase with the incident wave. The reflected wave does not undergo any phase shift. This is responsible for the AMC property (in-phase reflection property).

To demonstrate the existence of the two types of resonance, the authors in [11] design a square patch FSS with unit cell dimension = 6.9mm and square patch length = 6.1mm placed on a grounded dielectric substrate with thickness 1.13mm and $\varepsilon_r = 3.2$ as shown in Fig. 3.9. There are no metallic vias connecting the patches to the ground plane. A plane wave is incident on this surface. The reflection phase, induced current magnitude and induced current phase are then plotted by the authors till 50GHz. The natures of all these curves are plotted in Fig. 3.10. The in-phase reflection (AMC) phenomenon occurs near 17GHz while the EBG phenomenon occurs near 40GHz. While it is obvious that the AMC and EBG properties are far apart, they can be made to overlap by adjusting the periodicity of the array as well as the substrate thickness. As the array periodicity increases, the AMC frequency increases while the EBG frequency decreases. Similarly, as the substrate thickness decreases, the AMC frequency decreases while the EBG frequency increases. Therefore, the two frequencies can be made to overlap by

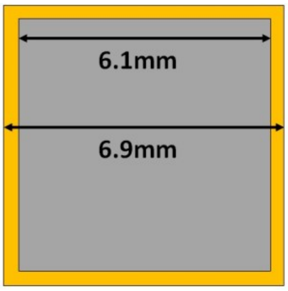

Fig. 3.9. Unit cell.

carefully choosing the periodicity of the patch array and the substrate thickness as the authors demonstrate in [11].

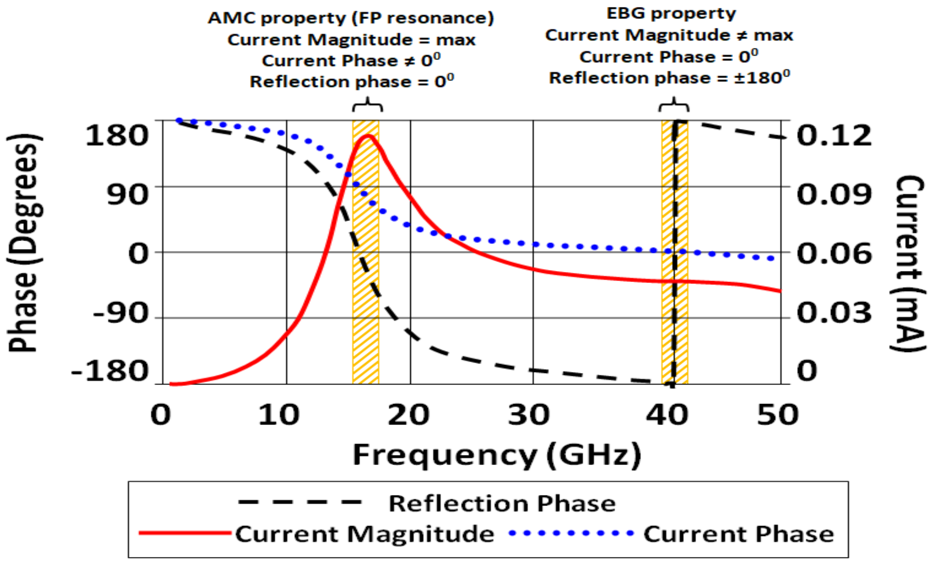

Fig. 3.10. Reflection phase, induced current magnitude and induced current phases of the 2D array of metallic patches on a grounded dielectric without the presence of vias.

3.1.4 Effect of angle of incidence on the AMC property

Consider that an AMC surface is present on the xy plane and a plane wave is normally incident on it from the +z direction. In this case, the angle of incidence (say θ) = 0^0. For oblique incidence ($\theta \neq 0^0$), the wave is either TM polarized or TE polarized (Fig. 3.11).

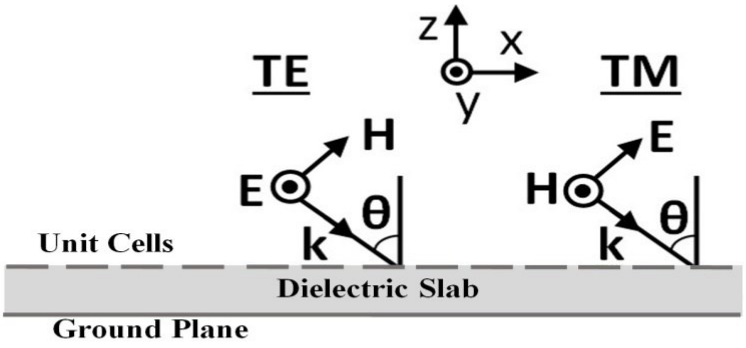

Fig. 3.11. TE and TM polarized oblique incident waves.

The surface impedance seen by a TM polarized incident wave differs from that of a TE polarized wave [12]. Moreover, the surface impedance also varies as θ changes. This leads to shifting in the in-phase reflection frequency and forces the AMC structure to operate within a narrow range of incident angles [3, 10]. Therefore, one of the inherent disadvantages of the HIS is its low angular stability.

3.2 Partially Reflecting Surface – PRS

A PRS is a highly reflective sheet usually made using a frequency selective surface (FSS). An FSS is a 2D periodic sheet which is capable of providing EM pass-bands stop-bands. FSSs are usually used to design spatial EM wave filters.

In 1899, Charles Fabry and Alfred Pérot introduced a resonator consisting of two thin highly reflective parallel plane mirror segments [13, 14]. Optical waves could only pass through the cavity if they satisfied the resonance condition of the cavity. It later became popular as the Fabry- Pérot Interferometer or Fabry- Pérot Cavity (FPC) Resonator. It was mainly used in the field of laser optics and spectroscopy.

3.2.1 Working Principle of the FPC made using PRS

In 1955, Giswalt von Trentini demonstrated that by placing an antenna inside an FPC with one cavity wall made of a metallic reflector (PEC) and the other cavity wall made of a PRS, the directivity and gain of the antenna can be improved significantly [15]. Figure 3.12 sheds light into the working of the FPC. A PEC sheet and a PRS are placed parallel to each other. The distance between them is '*L*' units. This creates the FPC. Now, a radiating source, i.e., an antenna, is placed within the FPC.

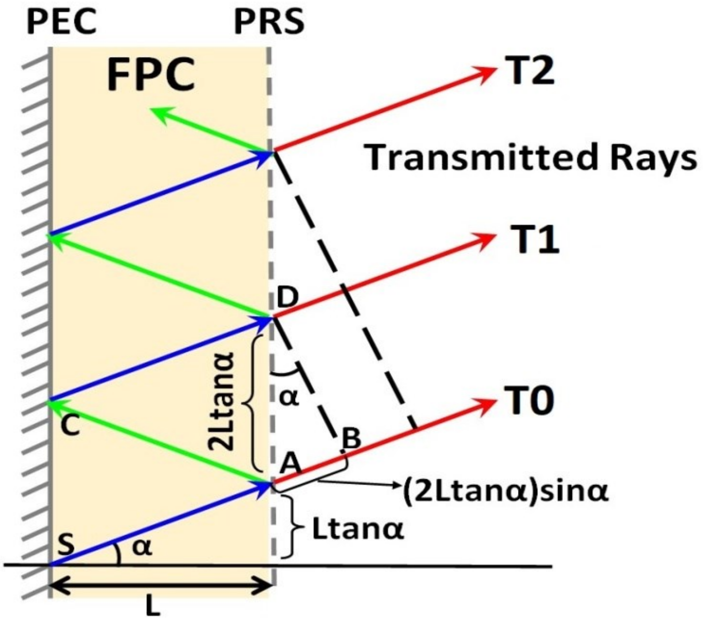

Fig. 3.12. Ray diagram demonstrating working principle of an FPC.

The radiated waves originating from the antenna bounce back and forth inside the cavity and a portion of the waves is also transmitted through the PRS as T0, T1, T2, etc. Considering that the phase of the PRS at the operating frequency φ_{PRS} and the phase of the PEC is $-\pi$ radians, the phase difference between Ray 0 and Ray 1 ($\Delta\varphi_1$) can be expressed as:

$$\Delta\varphi_1 = (\frac{2\pi}{\lambda})2L\tan\alpha\sin\alpha - (\frac{2\pi}{\lambda})2L\sec\alpha - \pi + \varphi_{PRS} \tag{3.10}$$

where λ = wavelength corresponding to the operating frequency. The 1st term in the RHS of (3.10) arises due to the path difference AB, the 2nd term arises due to the two additional reflection paths AC and CD, the 3rd term is the phase added after reflection from the PEC while the final term is the phase added after reflection from the PRS. The transmitted waves T0 and T1 also undergo a phase shift after transmission but the phase shift is same for both rays and hence does not show up in the phase difference of (3.10). The phase difference between T0 and Tn can similarly be written as:

$$\begin{aligned}\Delta\varphi_n &= (\frac{2\pi n}{\lambda})2L\tan\alpha\sin\alpha - (\frac{2\pi n}{\lambda})2L\sec\alpha - n\pi + n\varphi_{PRS} \\ &= n\left[(-\frac{4\pi}{\lambda})L\cos\alpha - \pi + \varphi_{PRS}\right] = n\varphi\end{aligned} \tag{3.11}$$

Considering the reflection coefficient of the PRS as $Re^{j\varphi_{PRS}}$, the magnitudes of T0, T1 and Tn are $\sqrt{(1-R^2)}$, $R\sqrt{(1-R^2)}$ and $nR\sqrt{(1-R^2)}$ respectively. Assuming that the PEC and PRS are infinite, the E-field in the far-field region can be expressed as an infinite sum of these partial transmissions as

$$E = \sum_{n=0}^{\infty} F(\alpha)E_oR^n e^{j\Delta\varphi_n}\sqrt{1-R^2} = \sum_{n=0}^{\infty} F(\alpha)E_o(\mathrm{Re}^{j\varphi})^n\sqrt{1-R^2} \tag{3.12}$$

where $F(\alpha)$ is the antenna element pattern. Since $R < 1$, $\sum_{n=0}^{\infty}(Re^{j\varphi})^n = 1/(1-Re^{j\varphi})$. Putting this into (3.12), the magnitude of the E-field can then be expressed as

$$|E| = |E_o|F(\alpha)\sqrt{\frac{1-R^2}{1+R^2-2R\cos\varphi}} \tag{3.13}$$

and the power pattern $$S = \frac{1-R^2}{1+R^2-2R\cos\varphi}\,F^2(\alpha) \qquad (3.14)$$

To ensure maximum power radiation, the denominator of (3.14) must be made minimum and the condition $\cos\varphi = 1$ ($\varphi = 2N\pi$; $N = 0, 1, 2\ldots$) must be satisfied. To ensure maximum radiation in the $\alpha = 0^0$ direction, the condition that needs to be satisfied is

$$(-\frac{4\pi}{\lambda})L - \pi + \varphi_{PRS} = 2\mathrm{N}\pi. \qquad (3.15)$$

This is the Fabry-Pérot cavity resonance condition, and it ensures maximum radiation in the broadside direction ($\alpha = 0^0$). In the most general case, when the ground plane is not a PEC, the resonance condition can be modified as

$$(-\frac{4\pi}{\lambda})L + \varphi_{GND} + \varphi_{PRS} = 2\mathrm{N}\pi \qquad (3.16)$$

where φ_{GND} = reflection phase of the ground plane at the frequency corresponding to λ.

For the condition of maximum power radiation,

$$S = \left(\frac{1+R}{1-R}\right)F^2(\alpha) \qquad (3.17)$$

and the directivity/gain enhancement factor $(1 + R)/(1 - R)$ is determined by the reflection coefficient magnitude of the PRS.

3.2.2 Narrow operating region due to resonance condition

In general, the phase of the PRS, φ_{PRS}, and the ground plane, φ_{GND}, decrease with increasing frequency. This means that the resonance condition of (3.16) is satisfied for a very narrow range of frequencies. Therefore, the FPC is inherently narrowband in nature.

3.3 Chiral Metasurface – CMS

The word *chirality* originates from the Greek *χείρ* which is used to mean ‘hand’. A structure is said to be chiral when it has mirror-asymmetry. This means that the image is always different from the object irrespective of its orientation. Our left and right hands are perfect examples of chiral structures. A chiral medium is one whose constituent molecules are chiral in nature. Such a medium can exhibit optical activity, which is the rotation of the polarization plane of EM waves traveling through it. This phenomenon was initially observed many years ago (in the early 1800s) by Arago and Biot in the optical frequency domain [16]. It was also observed in the microwave domain by Bose [17] in 1898. However, since the chirality was a consequence of the molecular arrangements and orientations, they could not be controlled at will. This changed after the advent of MMs and MSs. It was seen that on using appropriate unit cell geometries, MSs and MMs could exhibit chirality and optical activity which could be controlled by controlling the unit cell geometry. Such MSs are often called chiral MSs or CMSs.

3.3.1 Polarization plane rotation

CMSs can exhibit both magnetoelectric coupling (bianisotropy) and polarization rotation. In a generalized bianisotropic medium, the relations between the induced dipole moments and external fields at that location are given as

$$p_e = \bar{\bar{\alpha}}_{ee} \cdot E + \bar{\bar{\alpha}}_{em} \cdot H \quad \text{and} \quad p_\mathrm{m} = \bar{\bar{\alpha}}_{me} \cdot E + \bar{\bar{\alpha}}_{mm} \cdot H, \tag{3.18}$$

where p_e = electric dipole moment, p_m = magnetic dipole moment, E = local electric field, H = local magnetic field and $\bar{\bar{\alpha}}_{ee}, \bar{\bar{\alpha}}_{em}, \bar{\bar{\alpha}}_{me}, \bar{\bar{\alpha}}_{mm}$ are the electric, electro-magnetic, magneto-electric, and magnetic polarizability tensors respectively. When the periodicity and size of the unit cells are much smaller than the operating wavelength, the microscopic dipole moments p_e and p_m can be averaged in space and orientation to get the corresponding macroscopic E and H polarization densities. These average densities can then be related to the tensor susceptibilities of the medium, $\bar{\bar{\chi}}_{ab}$. After doing this, the constitutive relations can be written in the most general form as [30]

$$D = \bar{\bar{\varepsilon}} \cdot E + \bar{\bar{\xi}} \cdot H \quad \text{and} \quad B = \bar{\bar{\zeta}} \cdot E + \bar{\bar{\mu}} \cdot H, \tag{3.19}$$

with

$$\begin{pmatrix} \bar{\bar{\varepsilon}} & \bar{\bar{\xi}} \\ \bar{\bar{\zeta}} & \bar{\bar{\mu}} \end{pmatrix} = \begin{pmatrix} \varepsilon_0(\bar{\bar{I}} + \bar{\bar{\chi}}_{ee}) & \sqrt{\varepsilon_0\mu_0}\,\bar{\bar{\chi}}_{em} \\ \sqrt{\varepsilon_0\mu_0}\,\bar{\bar{\chi}}_{me} & \mu_0(\bar{\bar{I}} + \bar{\bar{\chi}}_{mm}) \end{pmatrix} \tag{3.20}$$

where $\bar{\bar{I}}$ = identity tensor, ε_0 = free space permittivity, μ_0 = free space permeability, D = electric response of the medium and B = magnetic response of the medium. Therefore, each of the electric and magnetic responses of the medium depends upon both the electric and magnetic excitations.

It should be noted however that bianisotropy does not always cause polarization rotation. If the electrical and magnetic responses of the material are parallel to the corresponding electric and magnetic excitations, then there is no polarization plane rotation despite magnetoelectric coupling. It is only when the electric and/or magnetic responses are perpendicular to the corresponding electric and magnetic excitations that the polarization plane of the incident wave is rotated. Since CMSs can exhibit polarization rotation as well as magnetoelectric coupling, a part of the electric and/or magnetic responses in such MSs are perpendicular to the electric and magnetic field excitations. Therefore, using a CMS will ensure polarization plane rotation.

3.3.2 Asymmetric Transmission of LP and CP waves

Let us consider an EM wave travelling along the z-direction with its *E*-field oriented along the x- or y-direction. For a reciprocal medium lying in the xy plane, the forward ($\hat{T}^f$) and backward ($\hat{T}^b$) transmission matrices relating the incident and transmitted *E*-fields can be expressed in the linear basis as

$$\hat{T}^f = \begin{pmatrix} T_{xx} & T_{xy} \\ T_{yx} & T_{yy} \end{pmatrix} \quad \text{and} \quad \hat{T}^b = \begin{pmatrix} T_{xx} & -T_{yx} \\ -T_{xy} & T_{yy} \end{pmatrix} \tag{3.21}$$

where T_{ij} corresponds to the transmission coefficient of an *i*-directed *E*-field component due to an incident *j*-directed *E*-field component. In the circular basis, the transmission coefficients can be expressed as

$$\hat{T}^{circ} = \begin{pmatrix} T_{rr} & T_{rl} \\ T_{lr} & T_{ll} \end{pmatrix} = \begin{pmatrix} T_{xx} + T_{yy} + i(T_{xy} - T_{yx}) & T_{xx} - T_{yy} + i(T_{xy} + T_{yx}) \\ T_{xx} - T_{yy} - i(T_{xy} + T_{yx}) & T_{xx} + T_{yy} - i(T_{xy} - T_{yx}) \end{pmatrix} \tag{3.22}$$

where the subscripts '*l*' and '*r*' correspond to left-hand CP (LHCP) and right-hand CP (RHCP) respectively.

The phenomenon of asymmetric transmission (AT) was first demonstrated by Fedotov *et al.* [18] in 2006 for incident CP waves using a periodic tilted fish-scale metallic pattern etched on one side of a substrate. It should be remembered that ***AT is a reciprocal phenomenon***.

A. AT for CP waves

In order for a structure to exhibit AT for CP waves, we must have $T_{rl} \neq T_{lr}$. If we consider an MS lying in the xy plane, then it achieves AT for CP waves only if its unit cells

(i) do not have any mirror symmetry with respect to the xz- or yz- plane and

(ii) do not have C4 (90^0) rotational symmetry.

If (i) is not satisfied, then we have $T_{xy} = T_{yx} = 0$ and hence $T_{rl} = T_{lr}$. If (ii) is not satisfied, then we have $T_{xx} = T_{yy}$ and $|T_{xy}| = |T_{yx}|$. This also leads to $T_{rl} = T_{lr}$. When both the conditions are satisfied, the MS can exhibit AT for CP waves. A single patterned metallic sheet can exhibit AT for CP waves if the unit cells satisfy (i) and (ii). The asymmetry parameter, Δ^i, is used to measure the degree of asymmetry of the structure. For CP waves, Δ^i_{circ} (i = l or r) is given as

$$\Delta^{l}_{\mathrm{circ}} = \left|T_{\mathrm{rl}}\right|^2 - \left|T_{\mathrm{lr}}\right|^2 = -\Delta^{\mathrm{r}}_{\mathrm{circ}} \quad . \tag{3.23}$$

B. AT for LP waves

In order to achieve AT for LP incident waves, we must have $T_{\mathrm{xy}} \neq 0$, $T_{\mathrm{yx}} \neq 0$ and $|T_{\mathrm{xy}}| \neq |T_{\mathrm{yx}}|$. To satisfy these conditions, we need to break certain symmetries of the MS unit cell which is again assumed to lie in the xy plane. These are listed as follows:

(i) The unit cell cannot have any mirror symmetry with respect to the xz- or yz- planes.

(ii) The unit cell cannot have any C4 (90^0) rotational symmetry.

(iii) The unit cell cannot possess any mirror symmetry with respect to a plane perpendicular to the z-axis.

All three of these conditions must be met simultaneously to ensure AT of LP waves.

While (i) and (ii) are satisfied using a single layered anisotropic unit cell metallization, (iii) tells us that the symmetry of the unit cell along the direction of wave propagation (z-direction) must be broken as well. Although this can be done by patterning the metal on a substrate, the resulting AT is negligible. Therefore, an additional metallic pattern has to be incorporated at the bottom of the substrate to ensure noticeable AT for LP waves. This means that more than one layer of metallization is needed to successfully achieve the AT of LP waves. A double layered chiral metasurface (CMS) lacking C4 rotational symmetry can satisfy all the necessary conditions mentioned above. For LP waves, the asymmetry parameter, $\Delta^{i}_{\mathrm{lin}}$, (i = x or y) is given as

$$\Delta^{x}_{\mathrm{lin}} = \left|T_{\mathrm{yx}}\right|^{2} - \left|T_{\mathrm{xy}}\right|^{2} = -\Delta^{y}_{\mathrm{lin}} \quad . \tag{3.24}$$

3.4 Spoof Surface Plasmon Polariton – SSPP

3.4.1 Surface Plasmon Polaritons

Surface Plasmons (SPs) are coherent delocalized electron oscillations which exist only at interfaces across which the sign of the permittivity changes, i.e., Re{ε} changes sign. Metals can usually be characterized by a negative permittivity at optical and infrared frequencies. So, SPs usually exist at air-metal interfaces at these frequencies. Since they are primarily charge oscillations, they also produce EM fields. The motions of the charges as well as the corresponding EM fields are together called surface plasmon polaritons (SPPs). These are a type of surface waves which are guided along the air-metal interface. Photons and electrons are capable of exciting SPPs. However, in case of photons, a prism/grating/defect in the metal surface is also required to match the SPP and photon wave vectors (i.e., their, momentum). For a surface wave to propagate along a metal surface, the *E*-field has to be polarized perpendicular to the surface. Otherwise, the boundary conditions imposed by Maxwell's equations will require the *E*-field to be zero. Therefore, only a TM type surface wave can exist on the air-metal interface with its *H*-field parallel to the surface and *E*-field perpendicular to the surface. Hence, the SPP is a TM type surface wave.

A. Dispersion Relation

The dispersion relation of the SPP can be derived from the Fresnel reflection coefficient for TM incidence (Γ_{TM}). Consider the illustration shown in Fig. 3.13. It shows the interface between two media. Medium 1 has a permittivity and permeability of ε_1 and μ_0 respectively while Medium 2 has a permittivity and permeability of ε_2 and μ_0 respectively. We have $\varepsilon_1 = \varepsilon_0\varepsilon_{r1}$, $\varepsilon_2 = \varepsilon_0\varepsilon_{r2}$ and $c = 1/\sqrt{\mu_0\varepsilon_0}$ where ε_{r1} and ε_{r2} are the relative permittivity of Medium 1 and 2 respectively while ε_0 and μ_0 are the free space permittivity and permeability respectively.

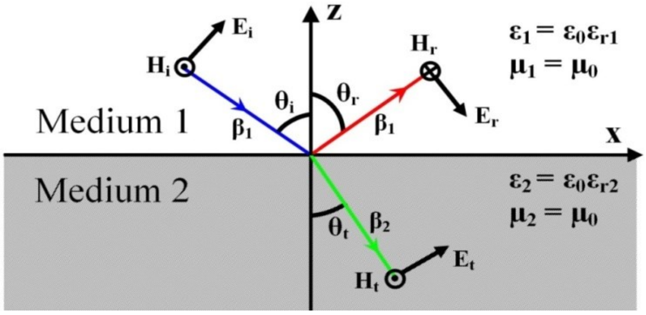

Fig. 3.13. Field configurations for TM incidence at the interface between two media.

E_i and H_i are the incident E and H fields, E_r and H_r are the reflected E and H fields while E_t and H_t are the transmitted E and H fields. The propagation constant in Medium 1 is β_1 ($\beta_1 = \omega\sqrt{\mu_0\varepsilon_1}$) and the propagation constant in Medium 2 is β_2 ($\beta_2 = \omega\sqrt{\mu_0\varepsilon_2}$). The incident angle is θ_i, the reflected angle is θ_r and the transmitted angle is θ_t. The reflection coefficient can then be written as

$$\Gamma_{TM} = \frac{\sqrt{\dfrac{\mu_0}{\varepsilon_2}}\cos\theta_t - \sqrt{\dfrac{\mu_0}{\varepsilon_1}}\cos\theta_i}{\sqrt{\dfrac{\mu_0}{\varepsilon_2}}\cos\theta_t + \sqrt{\dfrac{\mu_0}{\varepsilon_1}}\cos\theta_i} = \frac{\dfrac{\beta_{2z}}{\varepsilon_2} - \dfrac{\beta_{1z}}{\varepsilon_1}}{\dfrac{\beta_{2z}}{\varepsilon_2} + \dfrac{\beta_{1z}}{\varepsilon_1}}, \tag{3.25}$$

where we have utilized the fact that $\beta_{1z} = \beta_1\cos\theta_i$ and $\beta_{2z} = \beta_2\cos\theta_t$. For the plasmonic resonance and propagation mode generation at the interface, we set $\Gamma_{TM} \rightarrow \infty$. This implies that a reflected wave exists when there is no incident wave and is often encountered in resonance systems. For this case, the denominator of (3.25) → 0 and we have

$$\frac{\beta_{2z}}{\varepsilon_2} + \frac{\beta_{1z}}{\varepsilon_1} = 0 \tag{3.26}$$

If we consider Medium 1 to have a positive permittivity, i.e., ε_1 = positive, then the 2nd term of (3.26) is positive. Therefore, the 1st term must be negative in order to satisfy (3.26). This means that ε_2 has to be negative (i.e., ε_{r2} has to be negative). Taking the 2nd term of (3.26) to the right hand side and squaring both sides, we get

$$\varepsilon_2{}^2\beta_{1z}{}^2 = \varepsilon_1{}^2\beta_{2z}{}^2,$$

or

$$\varepsilon_2{}^2(\beta_1{}^2 - \beta_{1x}{}^2) = \varepsilon_1{}^2(\beta_2{}^2 - \beta_{2x}{}^2). \tag{3.27}$$

In order to satisfy the phase matching condition at the interface, we have $\beta_{1x} = \beta_{2x} = \beta_x$. Continuing with (3.27),

$$\varepsilon_2^{\ 2}(\beta_1^{\ 2} - \beta_x^{\ 2}) = \varepsilon_1^{\ 2}(\beta_2^{\ 2} - \beta_x^{\ 2}),$$

or
$$\beta_x^{\ 2}(\varepsilon_1^{\ 2} - \varepsilon_2^{\ 2}) = \varepsilon_1^{\ 2}\beta_2^{\ 2} - \varepsilon_2^{\ 2}\beta_1^{\ 2},$$

or
$$\beta_x^{\ 2}(\varepsilon_1 - \varepsilon_2)(\varepsilon_1 + \varepsilon_2) = \varepsilon_1^{\ 2}\omega^2\mu_0\varepsilon_2 - \varepsilon_2^{\ 2}\omega^2\mu_0\varepsilon_1,$$

or
$$\beta_x = \frac{\omega}{c}\sqrt{\frac{\varepsilon_{r1}\varepsilon_{r2}}{\varepsilon_{r1} + \varepsilon_{r2}}}. \tag{3.28}$$

Equation 3.28 is the dispersion relation of the SPP. Since ε_{r2} is negative, we must have $\varepsilon_{r1} + \varepsilon_{r2}$ = negative in order to ensure that the square root term of (3.28) is positive and β_x = *purely real.* This corresponds to a guided wave propagating along the x-direction. Then we have

$$\beta_{1z} = \sqrt{\beta_1^{\ 2} - \beta_x^{\ 2}} = \frac{\omega}{c}\sqrt{\varepsilon_{r1}\left(1 - \frac{\varepsilon_{r2}}{\varepsilon_{r1} + \varepsilon_{r2}}\right)}, \tag{3.29}$$

and
$$\beta_{2z} = \sqrt{\beta_2^{\ 2} - \beta_x^{\ 2}} = \frac{\omega}{c}\sqrt{\varepsilon_{r2}\left(1 - \frac{\varepsilon_{r1}}{\varepsilon_{r1} + \varepsilon_{r2}}\right)}. \tag{3.30}$$

Since ε_{r2} = negative, in (3.29), we have $\varepsilon_{r2}/(\varepsilon_{r1} + \varepsilon_{r2}) > 1$ and β_{1z} = *purely imaginary.* This means that the wave gets attenuated as we move away from the interface along the z-direction in medium 1. In (3.30), β_2^2 = negative and so β_{2z} *is also purely imaginary*. In fact, β_{2z} is an even larger imaginary number compared to β_{1z} indicating that the SPP decays more rapidly (with respect to the decay rate in medium 1) as we move away from the surface within medium 2 which has a negative permittivity.

The resultant wave corresponds to a wave trapped along the interface while decaying exponentially as we move away from the interface. An illustration of an SPP wave existing in the air-metal interface is presented in Fig. 3.14. The SPP is a combination of the electron oscillations within the metal and the EM mode that exists in air. It decays exponentially away from the surface along both the +z and –z directions. The *E*-fields are perpendicular to the interface while the *H*-fields are parallel to the interface. The attenuation of the SPP along the z-direction is shown to the right of Fig. 3.14. The wave falls off rapidly within the metal while it falls of relatively slowly in air.

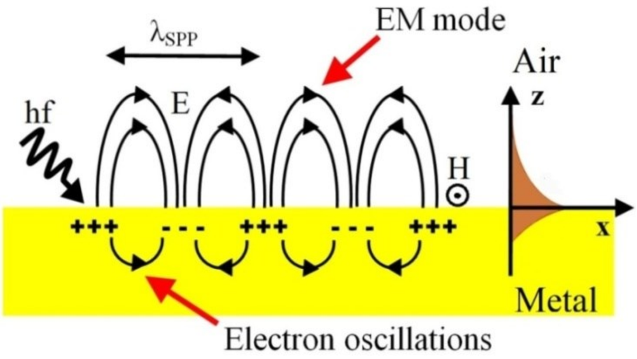

Fig. 3.14. Illustration of an SPP wave existing in air-metal interface.

While working close to the resonance, $\varepsilon_{r1} + \varepsilon_{r2} \rightarrow 0$ and β_x becomes very large. This in turn implies that the wavelength of the SPP becomes very short while both β_{1z} and β_{2z} become very large imaginary numbers. The SPP mode then becomes very tightly confined to the surface of the metal. Since the SPP mode is highly confined to the surface, it can be used in circuits to reduce cross-talk and interference between adjacent circuit elements. Since the wavelength of the SPP mode is much smaller than the free space wavelength, it can be used to design miniaturized circuits.

Using the Drude model of electrical conductivity, the relative permittivity of a metal at very high frequencies can be approximated as $\varepsilon_{r2} = 1 - (\omega_P/\omega)^2$ where ω_P is the plasma frequency of the metal with $\omega_P = \sqrt{ne^2/m\varepsilon_0}$ (n = electron density; e = electron charge; m = effective electron mass; ε_0 = free-space permittivity). When $\omega > \omega_P$, ε_{r2} becomes positive and the metal becomes transparent to EM radiations. To calculate the value of the asymptotic frequency limit of the dispersion relation, we solve (3.28) for $k_x \rightarrow \infty$. We then have

$$\varepsilon_{r1} + \varepsilon_{r2} = 0$$

or

$$\varepsilon_{r1} + (1 - \left(\frac{\omega_P}{\omega}\right)^2) = 0$$

or

$$\omega = \omega_{SP} = \frac{\omega_P}{\sqrt{1 + \varepsilon_{r1}}} \tag{3.31}$$

The asymptotic frequency limit is considered to be ω_{SP} (SP for surface plasmon) and its value is given by (3.31). When medium 1 is air, $\varepsilon_{r1} = 1$ and we have $\omega_{SP} = \omega_P/\sqrt{2}$.The dispersion relation graph of the SPP at an air-metal interface is shown in Fig. 3.15.

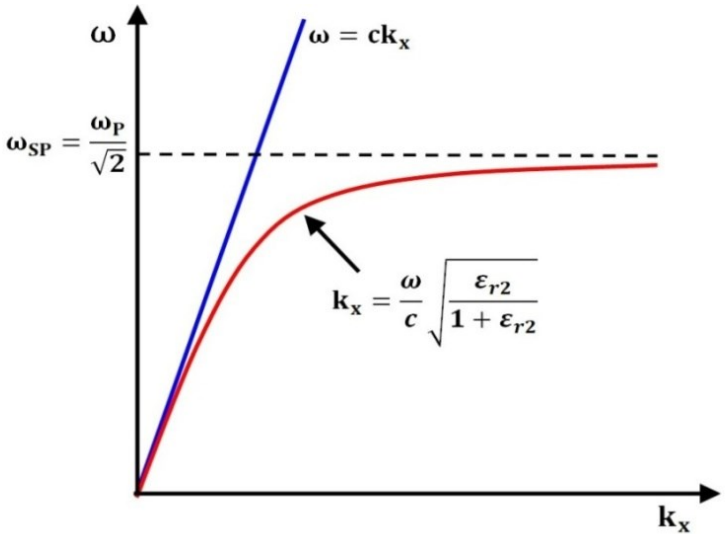

Fig. 3.15. Dispersion curve for an SPP wave existing in air-metal interface.

The blue line ($\omega = ck_x$) in Fig. 3.15 is the light-line which corresponds to no dispersion. As k_x increases, the dispersion curve (red line) moves further away from the light-line and the dispersion becomes noticeable. The fact that the curve is located to the right of the light-line implies that the SPP is a bound mode with a phase velocity less than the velocity of light in free space.

3.4.2 Spoof Surface Plasmon Polaritons

In 2004, Pendry *et al*. [19] demonstrated that drilling holes in a periodic fashion on a PEC surface introduces a bound surface state on the PEC which mimics the SP mode, provided that the periodicity and hole dimensions are much smaller than the operating wavelength. This “spoof” surface plasmon exhibits a dispersion relation similar to the SP discussed in the previous subsection. The authors also demonstrated that by adjusting the dimensions of the holes, the frequency of the surface plasmons can be shifted and changed to regions where they do not exist naturally. Therefore, the authors showed that it is possible to design a structured surface such that it can exhibit this “spoof” surface plasmon behavior even in microwave frequencies. These “Spoof” Surface Plasmons Polaritons (SSPPs), mimicking the nature of the actual SPPs, can be obtained by using periodic engineered surfaces. These SSPPs share the high field confinement and miniaturized wavelength properties possessed by the actual SPPs.

3.5 Conclusions

The four different types of textured surfaces that are the primary focus of this dissertation are analyzed in this chapter. The origins of their unique properties are also discussed. In the following chapters, these properties will be exploited and utilized to design textured surfaces which can be used for different applications within the microwave frequency domain.

REFERENCES

[1] D. Sievenpiper, Z. Lijun, R. F. Broas, N. G. Alexopoulos, and E. Yablonovitch, “High impedance electromagnetic surfaces with a forbidden frequency band,” *IEEE Trans. Microw. Theory Tech.*, vol. 47, no. 11, pp. 2059–2074, Nov. 1999.

[2] M. Li, Q. L. Li, B. Wang, C. F. Zhou, and S. W. Cheung, “A low-profile dual-polarized dipole antenna using wideband AMC reflector,” *IEEE Trans. Ant. Propag.*, vol. 66, no. 5, pp. 2610–2615, May 2018.

[3] M. E. de Cos, Y. Alvarez, and F. Las-Heras, “Novel broadband artificial magnetic conductor with hexagonal unit cell,” *IEEE Ant. Wireless Propag. Lttrs.,* vol. 10, pp. 615-618, 2011.

[4] N. M. Mohamed-Hicho, E. Antonino-Davin, M. Cabedo-Fabres, and M. Ferrando-Bataller, “A novel low-profile high-gain UHF antenna using high-impedance surfaces,” *IEEE Ant. Wireless Propag. Lttrs.,* vol. 14, pp. 1014-1017, 2015.

[5] Y. F. Cao, X. Y. Zhang and T. Mo, “Low-profile conical-pattern slot antenna with wideband performance using artificial magnetic conductors,” *IEEE Trans Ant. Propag.*, vol. 66, no. 5, pp. 2210–2218, May 2018.

[6] J. Zhu, S. Li, S. Lao, and Q. Xue, “Wideband low-profile highly isolated MIMO antenna with artificial magnetic conductor,” *IEEE Ant. Wireless Propag. Lttrs.,* vol. 17, no. 3, pp. 458-462, Mar. 2018.

[7] J. Wu, S. Yang, Y. Chen, S. Qu, and Z. Nie, “A low profile dual-polarized wideband omnidirectional antenna based on AMC reflector,” *IEEE Trans Ant. Propag.*, vol. 65, no. 1, pp. 368–374, Jan. 2017.

[8] Y. F. Cao, and X. Y. Zhang, “A wideband beam-steerable slot antenna using artificial magnetic conductors with simple structure,” *IEEE Trans Ant. Propag.*, vol. 66, no. 4, pp. 1685–1694, Apr. 2018.

[9] A. Monorchio, G. Manara, and L. Lanuzza, “Synthesis of artificial magnetic conductors by using multilayered frequency selective surfaces,” *IEEE Ant. Wireless Propag. Lttrs.,* vol. 1, pp. 196-199, 2002.

[10] M. E. de Cos, Y. Alvarez, R. C. Hadarig and F. Las-Heras, “Novel SHF-Band uniplanar artificial magnetic conductor,” *IEEE Antennas and Wireless Propagation Letters*, vol. 9, pp. 44-47, 2010.

[11] G. Goussetis*,* A. P. Feresidis*,* and J. C. Vardaxoglou*,* “Tailoring the AMC and EBG characteristics of periodic metallic arrays printed on grounded dielectric substrate,” *IEEE Trans. Ant. Prop.,* vol. 54, no. 1, pp. 82-89, Jan. 2006.

[12] C. R. Simovski, P. de Maagt, and I. V. Melchakova, “High-impedance surfaces having stable resonance with respect to polarization and incident angle,” *IEEE Trans. Ant. Prop.,* vol. 53, no. 3, pp. 908-914, Mar. 2005.

[13] C. Fabry, A. Perot, “Theorie et applications d'une nouvelle methode de spectroscopie interferentielle,” *Ann. Chim. Phys*. vol. 16, no. 7, pp. 115-144, 1899.

[14] A. Perot, C. Fabry, “On the Application of Interference Phenomena to the Solution of Various Problems of Spectroscopy and Metrology,” *Astrophysical Journal*, vol. 9, pp. 87, Feb. 1899.

[15] G. V. Trentini, “Partially reflecting sheet arrays,” *IRE Transactions on Antennas and Propagation*, vol. AP-4, no. 4, pp. 666–671, 1956.

[16] C. Caloz and A. Sihvola, "Electromagnetic Chirality, Part 1: The Microscopic Perspective [Electromagnetic Perspectives],” *IEEE Antennas and Propagation Magazine*, vol. 62, no. 1, pp. 58-71, Feb. 2020.

[17] J. A. Kong, “Theorems of bianisotropic media,” *Proc. IEEE*, vol. 60, no. 9, pp. 1036–1046, Sept. 1972.

[18] V. A. Fedotov *et al.,* “Asymmetric propagation of electromagnetic waves through a planar chiral structure,” *Phys. Rev. Lett., v*ol. 97, no.16, pp. 167401–167404, 2006.

[19] J. B. Pendry, L. Martín-Moreno, F. J. Garcia-Vidal, “Mimicking surface plasmons with structured surfaces,” *Science*, vol. 305, 5658, pp. 847-848, 2004.

CHAPTER 4

A DUAL-BAND AMC REFLECTOR WITH UHF-RFID READER

4.1 Introduction to RFID

The radio frequency identification (RFID) technique has emerged as a low cost and effective technique for tagging and tracking items in various industries in the market [1]. The UHF-RFID band is one of the most extensively used frequency bands for RFID operations. The RFID system usually consists of an RFID tag and an RFID reader. Both have in-built antennas which help them communicate wirelessly with each other. The tag is usually connected to the item which has to be marked/ tracked and the reader acts as an interrogator to identify and locate the tag.

Although both the tag and the reader antennas can be linearly polarized (LP), this often leads to orientation mismatch loss when the tag and reader antennas are not aligned properly. In the worst case, when the *E*-field principle planes of the tag and reader are oriented orthogonally, the reader will receive no information from the tag. To mitigate this issue, it is desirable to equip either the reader or tag with a circularly polarized (CP) antenna. Since the RFID tags are usually small in size, it is often more convenient to equip the reader with a CP antenna. Such CP reader antennas can detect tags irrespective of the tag orientation. Dual-band reader antennas (UHF-RFID/WLAN) can then send information received from tags to data centers via the WLAN channel. Most of the CP RFID reader antennas in literature cover only a single band. In [2]–[7], single-band CP UHF-RFID reader antennas are designed. Chen *et al.* [8] use stacked annular rings to achieve CP at the UHF-RFID band. A dual-band CP antenna is also presented in [9]. A compact dual-band CP antenna is presented by authors in [10], but the antenna has low gain in the UHF-RFID band.

4.2 Objective

The main aim of this chapter is to design a dual-band RFID reader antenna that radiates CP waves within both the UHF-RFID band (902-928MHz with a center frequency of 915MHz) and the 2.45GHz WLAN band with good gains in both operating bands. The 915MHz channel can be used by the reader for UHF-RFID tag detection while the 2.45GHz channel can be used to transmit the acquired information to the necessary base-stations.

4.3 Antenna and AMC design

A. Circular Patch Antenna

The geometries of the top and bottom layers of the deigned antenna are shown in Fig. 4.1 with Lv = 14.3 mm, Lh = 15.8 mm, W = 2 mm, R = 79 mm, L = 100 mm, L1 = 9 mm and W1 = 6 mm. The basic antenna design revolves around a circular patch with a radius of 79 mm having a primary resonance near 1GHz. Two perpendicular slots are introduced on the patch (Fig. 4.1(a)) which shift the first resonance to 915MHz and introduce a second resonance at 2.45GHz. All the simulations in this chapter are performed using the CST Studio Suite software. The substrate used is FR-4 (ε_r = 4.2, tanδ = 0.02) with a thickness of 1.52 mm. The metal layer used is Copper with $\sigma = 5.8 \times 10^7$ S/m.

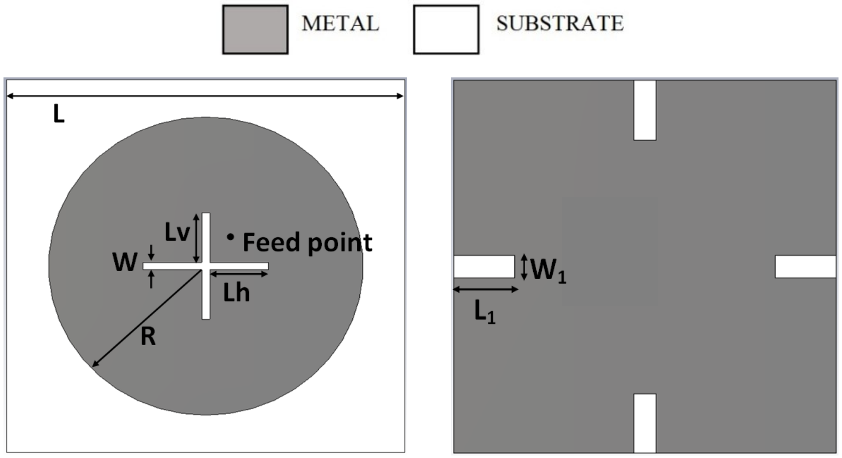

(a) (b)

Fig. 4.1. Circular patch antenna (a) top and (b) bottom.

Crossed dipoles are also used to introduce circular polarization [11]. As stated in [11], the main principle of operation for generating CP consists of two orthogonal elements having lengths such that:

i. the real parts of their admittances are equal;
ii. the angles of the admittances differ by 90°.

This principle has been extended to the orthogonal slots etched on the circular patch in the presented design. A similar principle has been used in [12]. It should be noted that the CP at 915MHz is not produced due to the crossed slots. It is produced because of the circular patch along with its feeding point location. The effect of the crossed slots on this first band is only the frequency shift due to the increased current path lengths. The second band CP (at 2.45GHz) is influenced by the crossed slots. The cross-slot lengths are designed and optimized such that their admittances satisfy the above two conditions at 2.45GHz. This is illustrated in Fig. 4.2. At 2.45GHz, the current primarily flows along the horizontal and vertical slots. The optimized lengths and admittances of the slots allow the horizontal and vertical components of the current to generate a 90° phase shift between them leading to CP behavior.

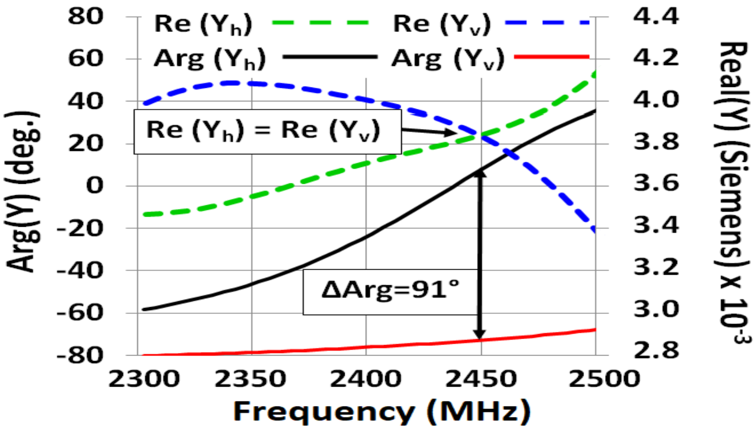

Fig. 4.2. Real part and argument of the individual slot admittances (subscript h = horizontal slot; subscript v = vertical slot).

It is found after simulation that the 3dB axial ratio (AR) bandwidth (BW) at the UHF-RFID band is low (as will be seen in Fig. 4.5(b)). To increase the AR-BW, four slits are introduced on the ground plane (Fig. 4.1(b)). This enhances the AR-BW at 915MHz. Varying Lv keeps the second band fixed and shifts the first band. Varying L1 and W shift the first band while keeping the second band fixed. Varying Lh affects both the bands. Therefore, the two required resonances of the antenna can be tuned independently. Considering the circular patch center to be at the origin of the rectangular coordinate system with x along the horizontal and y along the vertical, the feed point is at x = 9 mm, y = 9 mm.

B. Dual-Band AMC Unit Cell

The four slits on the antenna ground plane result in unwanted radiation below the antenna plane (as will be seen in Fig. 4.7(a)). To mitigate this issue, a dual-band AMC is designed to act as a reflector with two reflection phase nulls near 915MHz and 2.45GHz simultaneously. As discussed in Chapters 2 and 3, the AMC can be placed very close to an antenna and still act as a good reflector owing to its reflection magnitude of 1 and reflection phase of 0^0 at resonance. This ultimately reduces the height of the antenna system and makes it more compact. The top view of designed unit cell is shown in Fig. 4.3(a). FR-4 is used as the substrate of the AMC with a thickness of 1.52 mm. On the bottom of the substrate is the metal ground plane. Since the unit cell is symmetric about the x- and y-axes, it is independent of the orientation of the *E*-field in the xy plane, i.e., independent of the azimuth angle ϕ.

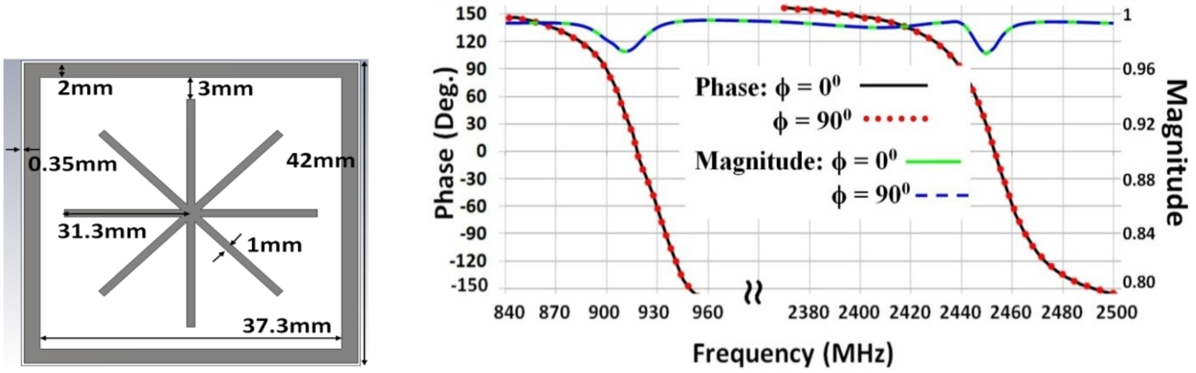

(a) (b)

Fig. 4.3. (a) AMC until cell (Grey = metal, white = substrate). (b) Reflection phase and magnitude plot.

The reflection phase graphs of the unit cell illustrated in Fig. 4.3(b) show the dual band nature and ϕ independence of the presented AMC structure. Increasing/decreasing the inner structure width shifts the second resonance of the AMC to the left/right.

Varying the gap between the inner and outer structure also affects the second resonance while the first resonance remains fixed. Increasing the length of the outer loop while keeping the unit cell dimensions same (decreasing the inter-element spacing) affects only the first resonance while the second remains fixed. Therefore, independent tuning of the two resonances of the AMC is possible.

A 5 × 5 array of unit cells is designed and placed 30 mm ($\lambda_{915MHz}/11$; λ_{915MHz} = free-space wavelength at 915MHz) below the patch antenna to function as a reflector.

4.4. Antenna Characteristics

To verify the simulation results, a prototype of the antenna is designed along with the AMC reflector consisting of 25-unit cells. The fabricated prototype with feeding mechanism is shown in Fig. 4.4.

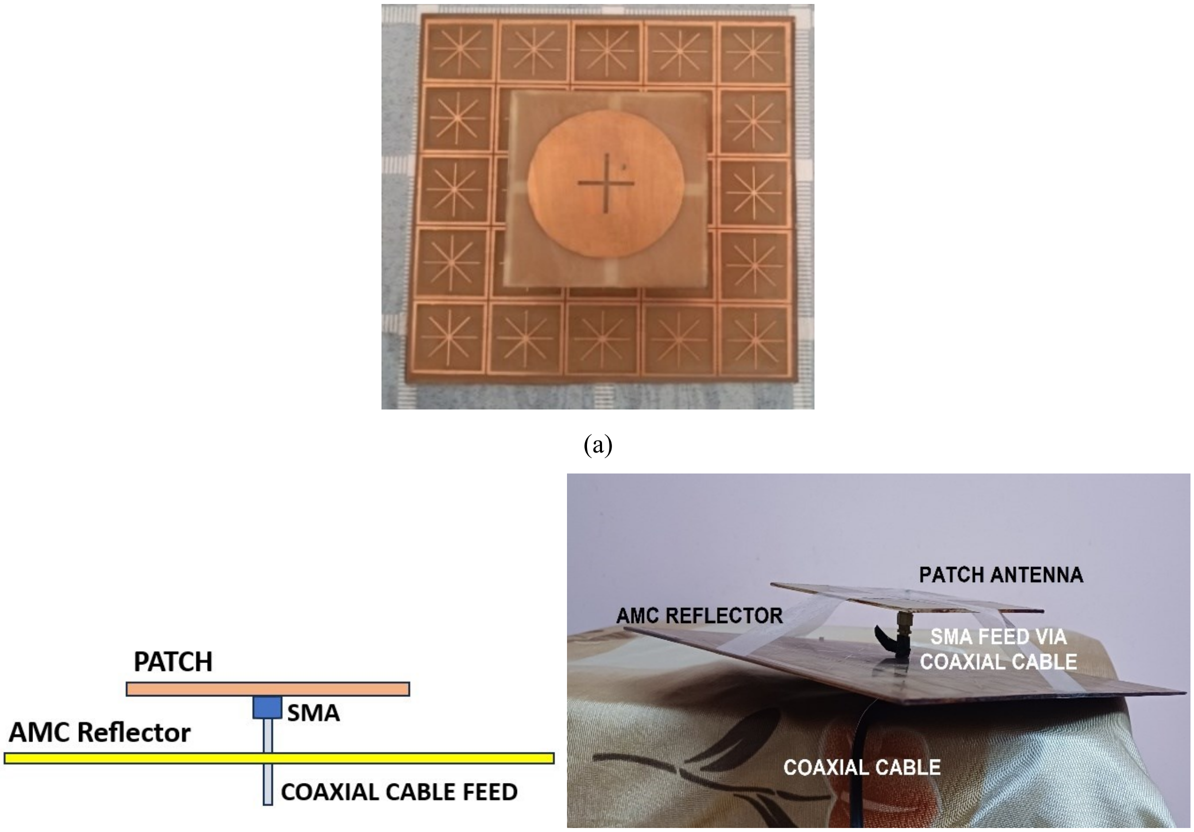

(a)

(b)

(c)

Fig. 4.4. Fabricated antenna with AMC reflector containing 25-unit cells (a) Top View, (b) Side view illustration and (c) 3D view.

Measurements are performed inside an anechoic chamber. A VNA is used for measurements. A wideband TEM horn antenna connected with the VNA is used to measure the radiation pattern characteristics of the patch + AMC antenna. The S_{11} is measured by connecting the patch + AMC antenna to a single VNA port and noting the S_{11} data. The radiation pattern and axial ratio are measured by using the horn antenna as a transmitting antenna and the patch + AMC as a receiving antenna. The different configurations of measurement are illustrated in Fig. 4.5 (a). The practical measurement setup is shown in Fig. 4.5 (b). The port extension feature of the VNA is used to bring the reference plane to the tip of the coaxial cables connecting the SMA connectors of the two antennas.

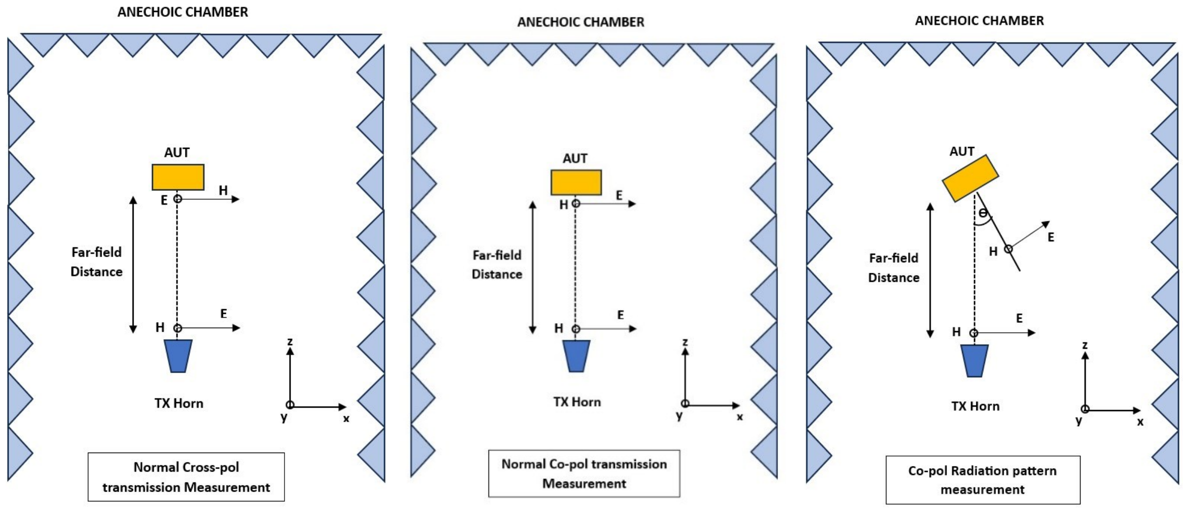

(a)

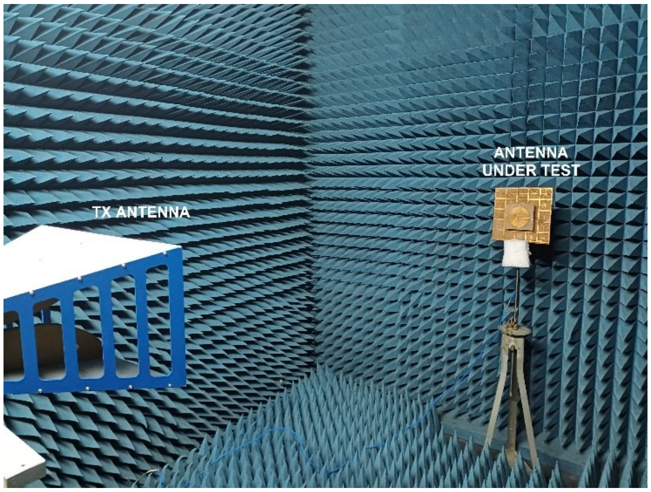

Fig. 4.5 (a) Different measurement configurations. (b) Practical setup for performing the measurements.

The axial ratio is measured using both the S_{21} magnitude and the S_{21} phase data. AT first, the co- and cross-pol S_{21} magnitudes are taken. These correspond to E_y, E_x and φ_y, φ_x respectively. Then, the difference between the two orthogonal phases $\Delta\varphi$ (φ_y - φ_x) is calculated. Assuming that the transmitting horn antenna has good polarization purity, the difference between the two phases gives an approximation of the difference between the two orthogonal polarizations. Using the magnitude and phase information, the Axial Ratio (linear) can be calculated as done in [14] by using the following formula:

$$AR = \sqrt{\frac{Ex^2 + Ey^2 + \sqrt{(Ex^4 + Ey^4 + 2Ey^2Ex^2\cos{(\Delta\varphi)}}}{Ex^2 + Ey^2 - \sqrt{(Ex^4 + Ey^4 + 2Ey^2Ex^2\cos{(\Delta\varphi)}}}} \quad (4.1)$$

The AR can be then be converted to dB. The sense of polarization can be understood from the sign of the phase difference $\Delta\varphi$. If it is positive, the sense is LHCP and if it is negative, the sense is RHCP. [14]. A reading is also taken by rotating the patch + AMC antenna by 45^0 about the z-axis. This is used to confirm that the phase is indeed reducing (for RHCP) and increasing (for LHCP). The handedness of the CP can also be determined by using Stokes parameters as discussed in Chapter 7.

The reflection coefficient graphs for the standalone patch (patch without any AMC) and the patch + AMC structure are similar in nature with both showing good matching at the UHF-RFID band and WLAN band, as seen in Fig. 4.6(a). It can also be seen from this figure that measured −10 dB S11 BWs of 24MHz (903–927 MHz) and 48MHz (2424–2472 MHz) are obtained at the UHF-RFID and WLAN bands, respectively. This results in percentage BWs of 2.6% (UHF-RFID) and 2% (WLAN) with center frequencies of 915MHz and 2.45GHz.

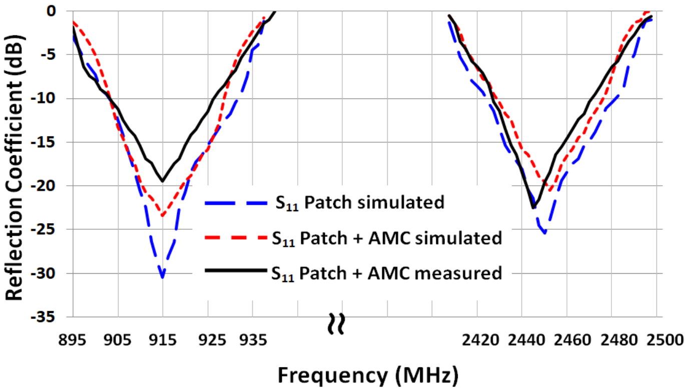

(a)

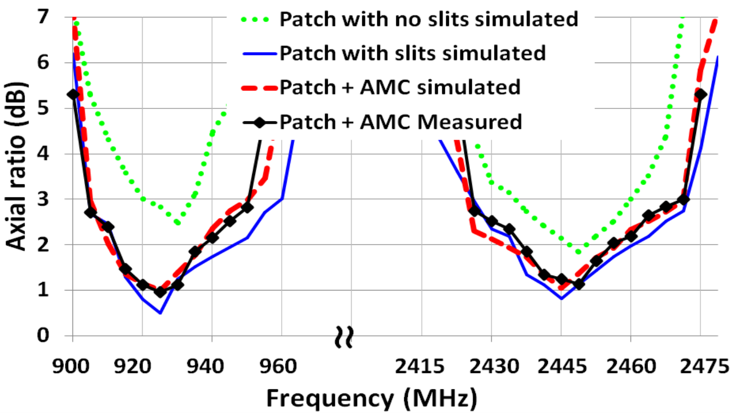

(b)

Fig. 4.6 (a) Reflection coefficient magnitude vs. frequency. (b) Axial ratio (AR) vs. frequency.

The AR versus frequency plots of Fig. 4.6(b) display the effects of the ground slits in enhancing the 3dB AR-BW, especially in the UHF-RFID band. This can be explained by observing that at 915MHz, a significant portion of the current is concentrated along the patch circumference (Fig. 4.7(a)). This means that they are concentrated along the ground slits. As the currents move along the horizontal slits, they produce a horizontal component. While they circulate along the vertical slits, they produce a vertical component.

These horizontal and vertical components have similar magnitudes but a phase difference of 90°. It can be seen from Fig. 4.7(a) (four marked areas) that the current bends away from the circumference while they move over the location of the ground slits. Therefore, the presence of the slits affects the current flow along the circumference. This leads to a significant enhancement of the AR at 915MHz. However, for 2.45 GHz, the current magnitudes are comparatively lower along the patch circumference as seen from Fig. 4.7(b). This means the ground slits have a smaller impact on the AR enhancement at 2.45GHz. This is exactly what is observed from Fig. 4.6(b).

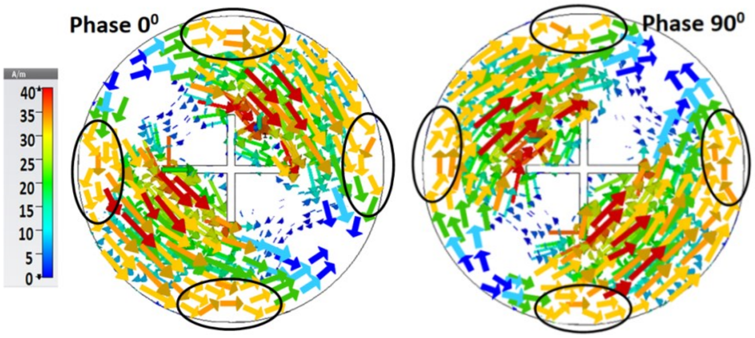

(a)

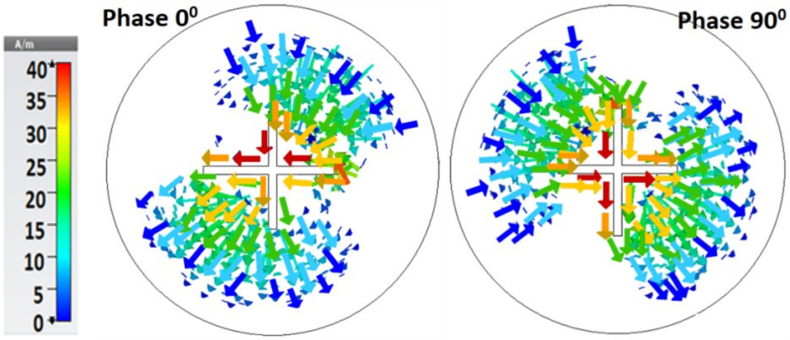

(b)

Fig. 4.7. Simulated surface current distributions (A/m) at (a) 915MHz and (b) 2.45GHz.

It can also be noted from Fig. 4.7(b) that at 2.45GHz, the induced surface currents are concentrated more along the horizontal slot length Lh. Therefore, Lh affects the second band more significantly at 2.45GHz. It is the presence of the horizontal slot which is mainly responsible for the second band at 2.45GHz. Lh and Lv are tuned to ensure that the orthogonal current components at 2.45GHz have similar amplitudes and 90^0 phase difference. At 915MHz, the current distribution is spread throughout the circular patch. Therefore, introducing the slots affects the current path length significantly. The induced surface currents at this frequency are distributed along both the horizontal and vertical slots (Lv and Lh). Therefore, both Lv and Lh affect the first resonance band. Addition of the AMC reflector does not significantly affect the axial ratio. Measured 3dB AR-BWs of 48MHz (902–950MHz) and 47 MHz (2423–2470MHz) are obtained at the UHF-RFID and WLAN bands, respectively, resulting in BWs of 5.25% (UHF-RFID) and 2% (WLAN).

The standalone patch exhibits significant radiation below the ground plane, especially at 915MHz, due to the presence of the four slits. This also results in very low gain in the positive broadside direction (+*z*-direction) above the patch antenna. The dual-band AMC reflector placed $\lambda_{915\text{MHz}}/11$ (30 mm) below the ground plane helps reduce the back-lobe level and results in constructive interferences to increase the main lobe gain.

The far-field radiation patterns are shown in Fig. 4.8. There is a significant change in the 915MHz radiation pattern after adding the AMC reflector. The gain increases from 0.58dBi (simulated; standalone patch) to 3.1dBi (measured; patch + AMC). The back-lobe maximum decreases from −4 to −14.1dBi. The improvement is similar in both the xz and yz planes.

The change in the radiation pattern at 2.45GHz is less prominent, with the gain increasing from 6.12dBi (simulated; standalone patch) to 6.2dBi (measured; patch + AMC). The back-lobe maximum decreases from around −12dBi to around −24dBi. The simulated cross-pol (opposite handedness) radiation pattern at 915MHz is presented in Fig. 4.8(c) while the simulated as well as measured cross-pol radiation patterns at 2.45GHz are shown in Fig. 4.8(d).

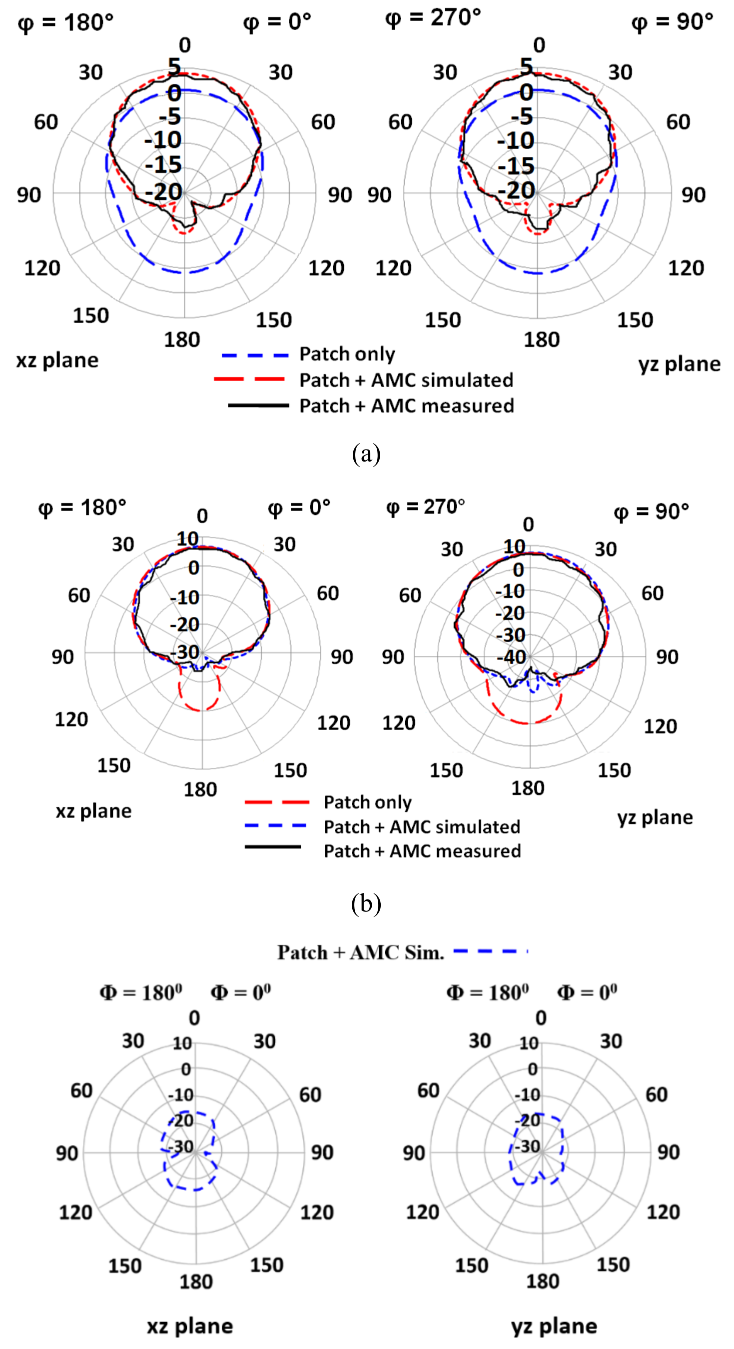

(a)

(b)

(c)

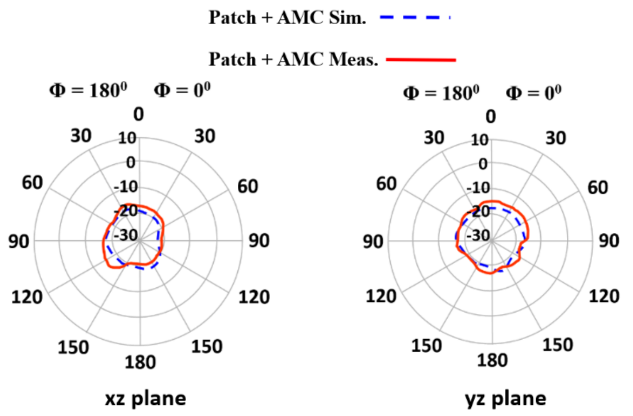

(d)

Fig. 4.8. Radiation patterns at (a) Co-pol 915MHz, (b) Co-pol 2.45GHz, (c) Cross-pol 915MHz and (d) Cross-pol 2.45GHz. Vertical markings are in dBi.

Table 4.1. Effects of introducing the AMC reflector.

Property	Frequency	Patch Only	Patch + AMC (25 unit cells)	Patch + AMC (16 unit cells)
Size (mm^2)		100 x 100	210 x 210	168 x 168
Gain	915MHz	0.58dBi (simulated)	3.1dBi (measured)	1.87dBi (simulated)
	2.45GHz	6.12dBi (simulated)	6.2dBi (measured)	6.18dBi (simulated)
Radiation Efficiency (simulated)	915MHz	55.8%	57.14%	55.93%
	2.45GHz	73.74%	74.31%	73.87%
Back-lobe maximum	915MHz	-4dBi (simulated)	-14.1dBi (measured)	-8.1dBi (simulated)
	2.45GHz	-10.28dBi (simulated)	-24.5Bi (measured)	-24.1dBi (simulated)

A comparison between the standalone patch and the final structure (patch + AMC) is presented in Table 4.1. The table also shows how the properties of the antenna system are affected when 16 unit cells of the AMC are used (Patch + AMC 16 unit cells) instead of 25.

It can be seen that the gain of the antenna using 16 unit cells reduces significantly (when compared to the 25 unit cells case) at 915MHz while the back-lobe maximum also increases. In applications where the antenna must be smaller in size, the AMC unit cells can be reduced from 25 to 16. In doing so, the total antenna size reduces from 210mm×210mm to 168mm × 168mm. This does not affect the matching or the AR-BW much. However, the penalty of reducing the system size is the reduction of gain at 915MHz from 3.1dBi to 1.87dBi and the increase in the back-lobe maximum from -14.1dBi to −8.1dBi.

The AR versus elevation angle (theta) is presented in Fig. 4.9. The measured AR remains below 3 dB up to at least ±60° in both the xz and yz plane for both 915MHz and 2.45GHz. This gives the antenna a good broadside angular range for circular polarization operation at both the frequency bands. The antenna radiates RHCP waves and has a gain of 2.91dBic and 6.05dBic at 915MHz and 2.45GHz, respectively.

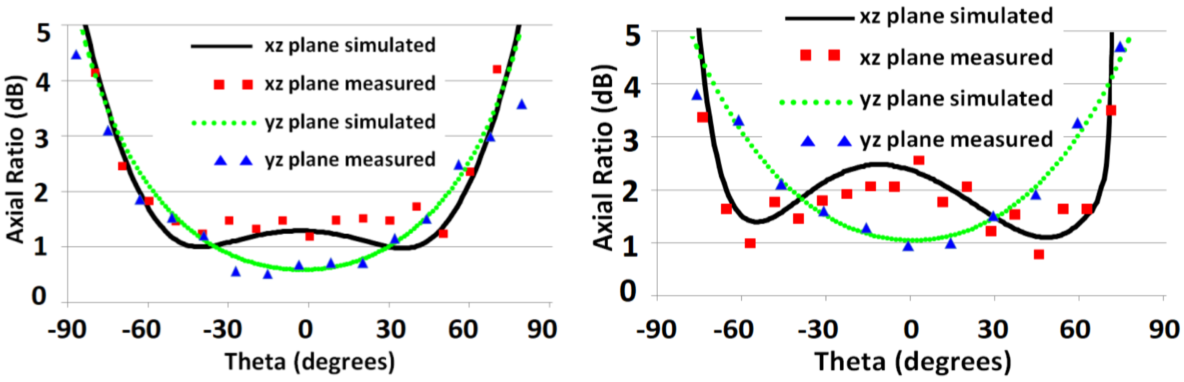

(a) (b)

Fig. 4.9. Simulated axial ratio (dB) versus angular variations at (a) 915MHz and (b) 2.45GHz.

Seeing that the reflector does not affect the antenna characteristics much at 2.45GHz, it might be assumed that a single band AMC reflector (at 915MHz) will give similar results.

However, using a single band AMC leads to a degradation in the AR versus angular (theta) variation plot at 2.45GHz in both the xz and yz planes. This can be seen from Fig. 4.10. In the xz and yz planes, the 3dB AR range reduces to θ = ±50° and θ = ±42° (for single band AMC) from the values of ±75° and ±60° (for dual-band AMC). This means that the fields present within the region θ = +45° to +90° and θ = -45° to -90° interact with the second band of the AMC reflector. Therefore, the dual-band AMC is used.

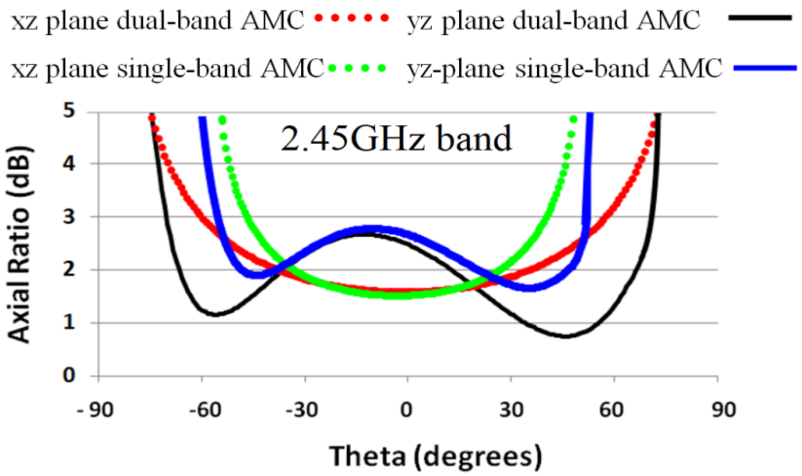

Fig. 4.10. Comparisons of AR vs. elevation angle between dual-band AMC and single-band AMC.

Table 4.2. Comparisons with other dual-band UHF-RFID readers present in literature.

Property	Ref. [10]	Ref. [13]	Patch + AMC
Size	0.18λ x 0.18λ x 0.02λ	0.67λ x 0.67λ x 0.08λ	0.64λ x 0.64λ x 0.09λ
No. of ports	2	2	1
AR BW	3.1% (915MHz) 0.9% (2.45GHz)	4.4% (920MHz) 8.2% (2.45GHz)	5.25% (915MHz) 2% (2.45GHz)
Gain	-0.6dBic (915MHz) 1.2dBic (2.45GHz)	6.6dBic (920MHz) 7.9dBic (2.45GHz)	2.91dBic (3.1dBi) (915MHz) 6.05dBic (6.25dBi) (2.45GHz)
Radiation Efficiency (simulated)	45% (915MHz) 34% (2.44GHz)	Not given	57.14% (915MHz) 74.31% (2.44GHz)

In Table 4.2, the presented structure has been compared with two papers presenting dual-band CP antennas radiating at 915 MHz and 2.45GHz [10], [13]. Both use FR-4 substrates and have two ports. The sizes of the antennas are presented in terms of the operating wavelength at 915MHz. While [10] is compact, it has vias and shorting pins which make fabrication cumbersome. Although [13] has higher gain and AR BW in the WLAN band, it has two ports and a very complex design while being larger in size than the presented structure (Patch + AMC). The Patch + AMC structure is simple to design and fabricate while also having a single port and good antenna gains at both bands. The efficiencies of the presented antenna can be increased by using a lower loss substrate.

4.5 Conclusions

In this chapter, a circular patch antenna with dual-band circular polarization at the UHF-RFID and WLAN bands is presented. Two perpendicular slots are etched on the patch to down-shift the first resonance to 915MHz (UHF-RFID band) and introduce a new resonance at 2.45GHz (WLAN band). Four slits are etched on the ground plane to improve axial ratio (AR) mainly in the first band. A dual-band AMC reflector having 25-unit cells is placed a small distance below the patch to reduce the back-lobe level and improve the gain at both bands. The antenna radiates RHCP waves at both bands. Measured 3dB AR bandwidths of 5.25% and 2% are achieved at UHF-RFID and WLAN bands respectively with gains of 2.91dBic (3.1dBi) (UHF-RFID) and 6.05dBic (6.25dBi) (WLAN). The antenna can be used with RFID readers for detecting tags and sending the information via the WLAN band.

REFERENCES

[1] K. Finkenzeller, *RFID Handbook: Fundamentals and Applications in Contactless Smart Cards, Radio Frequency Identification and Near-Field Communication.*, 3rd ed., Hoboken, NJ, USA: Wiley, Jun. 2010.

[2] R. Cao and S.-C. Yu, “Wideband compact CPW-fed circularly polarized antenna for universal UHF-RFID reader,” *IEEE Trans. Antennas Propag.*, vol. 63, no. 9, pp. 4148–4151, Sep. 2015.

[3] P. Janpangngern and C. Phongcharoenpanich, “Circularly polarized singlefedwide-slot antenna for UHF RFID reader,” in *Proc. ISAP*, 2017, pp. 1–2.

[4] M. H. Hoang, T. Q.V. Hoang, H. P. Phan, and T. P. Vuong, “ Cavity-backed circular-polarized compact slot antenna for handheld UHF RFID reader,” *IEEE Antennas Wireless Propag. Lett.*, vol. 14, pp. 1439–1442, 2015.

[5] W.-H. Zhang, P. Cheong, W.-J. Lu, and K.-W. Tam, “Planar endfire circularly polarized antenna for low profile handheld RFID reader,” *IEEE J. Radio Freq. Identif.*, vol. 2, no. 1, pp. 15–22, Mar. 2018.

[6] Z. Wang, R. She, J. Han, S. Fang, and Y. Liu, “Dual-band dual-sense circularly polarized stacked patch antenna with a small frequency ratio form UHF RFID reader applications,” *IEEE Access*, vol. 5, pp. 15260–15270, 2017.

[7] J. Li, H. Liu, S. Zhang, M. Luo, Y. Zhang, and S. He, “A wideband single-fed, circularly-polarized patch antenna with enhanced axial ratio bandwidth for UHF RFID reader applications,” *IEEE Access*, vol. 6, pp. 55883–55892, 2018.

[8] X. Chen, G. Fu, S.-X. Gong, Y.-L.Yan, and W. Zhao, “Circularly polarized stacked annular-ring microstrip antenna with integrated feeding network for UHF RFID readers,” *IEEE Antennas Wireless Propag. Lett.*, vol. 9, pp. 542–545, 2010.

[9] C. Jaehoon, K. Uisheon, U. Youngman, and S. Dongmin, “Design of antennas for the UHF RFID system,” in *Proc. Int. Workshop Antenna Technol.: Small Antennas Novel Metamater.*, 2008, pp. 75–78.

[10] R. Caso, A. Michel, M. Rodriguez-Pino, and P. Nepa, “Dual-band UHFRFID/ WLAN circularly polarized antenna for portable RFID readers,” *IEEE Trans. Antennas Propag.*, vol. 62, no. 5, pp. 2822–2826, May 2014.

[11] M. F. Bolster, “A new type of circular polarizer using crossed dipoles,” *IRE Trans. Microw. Theory Techn.*, vol. MTT-9, no. 5, pp. 385–388, Sep. 1961.

[12] M. N. Osman, M. K. A. Rahim, M. F. M. Yussof, M. R. Hamid, and H. A. Majid, “Polarization reconfigurable cross-slots circular patch antenna,” in *Proc. Int. Symp. Antenna Propag.*, 2013, pp. 1252–1255.

[13] Y.-K. Jung and B. Lee, “Dual-band circularly polarized microstrip RFID reader antenna using metamaterial branch-line coupler,” *IEEE Trans. Antennas Propag.*, vol. 60, no. 2, pp. 786–791, Feb. 2012.

[14] G. G. S. Forte, G. Fontgalland and S. E. Barbin, "Antenna Polarization Characterization with Vector Network Analyzer Measurements," *2018 International Conference on Electromagnetics in Advanced Applications (ICEAA)*, Cartagena, Colombia, 2018, pp. 597-600.

CHAPTER 5

AN AMC HAVING VERY HIGH ANGULAR STABILITY

5.1 Objective

In this chapter we focus on the angular dependence of AMC structures. While AMCs operate well under the normal incidence of a plane EM wave, the resonant frequency f_0 tends to shift for oblique incidence as discussed in Chapter 3. This usually degrades the in-phase reflection property and the AMCs are forced to operate within a very narrow range of wave incident angles [1, 2].

The main aim of this chapter is to design an AMC structure which has very good angular stability. Self-complementary unit cells (SCUCs) are used to design the proposed AMC. SCUCs form a series resonant grid/self-resonant grid (SRG), which tends to have good angular stability as reported in [3–5]. The structure in this chapter is optimized such that f_0 remains fixed with variations of the incident E-field polarization angle, ϕ.

5.2 AMC unit cell geometry and Equivalent Circuit

The unit cell has been designed and analyzed using CST Studio Suite. The unit cell dimensions are shown in Fig. 5.1(a). The conductor layer is copper with $\sigma = 5.8 \times 10^7$ S/m., and the dielectric substrate is FR-4 ($\varepsilon_{rd} = 4.4$; $\tan\delta = 0.02$; thickness = 1.52 mm). The left and right parts of the unit cell are complements of one another.

Considering the asymmetry of the structure about the x and y axes, the equivalent circuit seen by an incident wave with x-directed *E*-field (E_x) will differ from that seen by an incident wave with y-directed *E*-field (E_y). The equivalent circuits along these two orthogonal directions are shown in Figs. 5.1(b), (c).

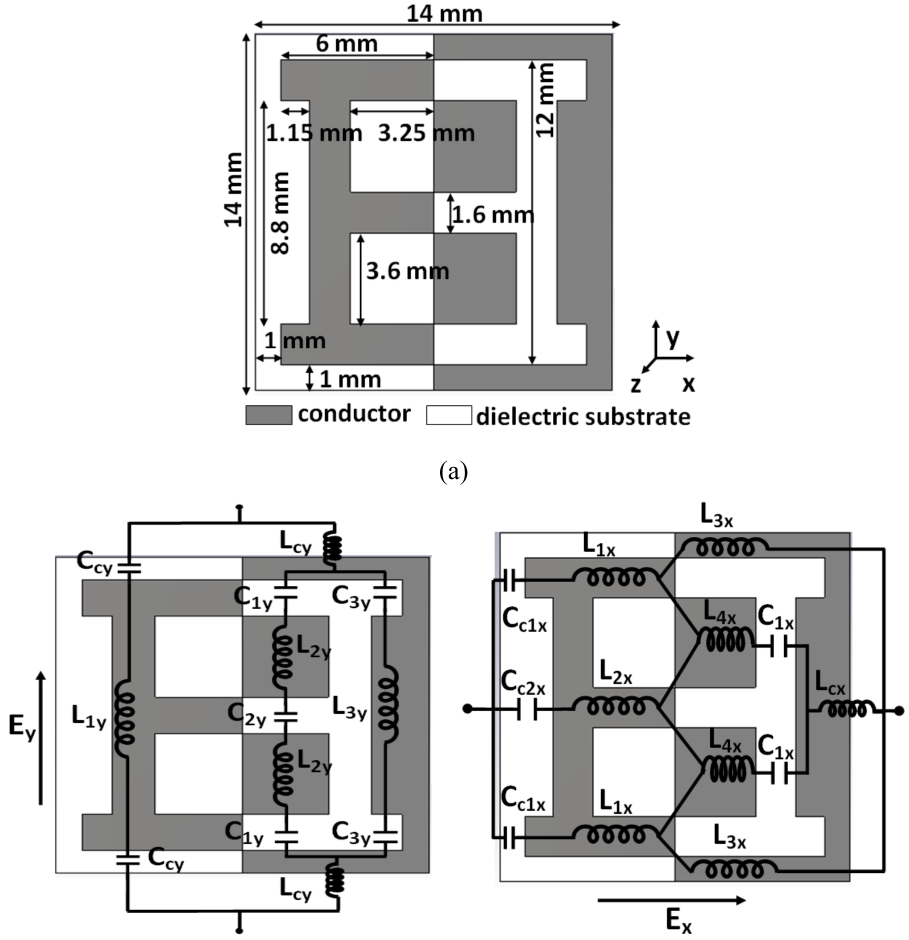

(a)

(b) (c)

Fig. 5.1 (a) Unit cell geometry. Equivalent circuit of unit cell for (b) E_y incidence and (c) E_x incidence.

As discussed in [9], an AMC structure such as a Jerusalem cross having both an inductance and capacitance within the unit cell can attain high angular stability when the vias to the ground plane are removed. It is also shown that the resonant frequencies obtained for such SRGs are independent of the incident field angles for both transverse electric (TE) and transverse magnetic (TM) incidence.

Considering that self-complementary structures inherently possess both a capacitance as well as inductance, they are good candidates for SRGs. C_{cy}, C_{c1x}, C_{c2x} and L_{cy}, L_{cx} are the capacitances and inductances coupled between adjacent unit cells (Figs. 5.1(b) and (c)). If we take the inductive impedance of the grounded dielectric layer to be Z_d, then the total impedance seen by the incident wave of Fig. 5.2(a) is $Z_i = Z_{unit\_i} \parallel Z_d$.

Z_{unit_i} is the impedance of the unit cell. For E_x incidence, $Z_i = Z_x$ and $Z_{unit\_i} = Z_{unit\_x}$. For E_y incidence, $Z_i = Z_y$ and $Z_{unit\_i} = Z_{unit\_y}$.

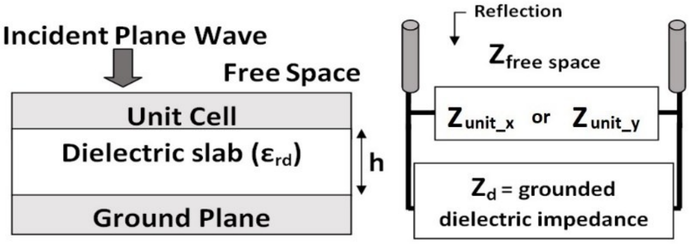

(a) (b)

Fig. 5.2 (a) Plane wave incidence on the AMC. (b) Parallel connection between cell impedance and grounded dielectric impedance.

The capacitances (C_{1y}, C_{2y}, C_{3y}) of the equivalent circuit dominate the impedance for E_y incidence while the inductances (L_{1x}, L_{2x}, L_{3x}, L_{4x},) dominate for E_x incidence. Considering that the ±90° reflection phase bandwidth (BW) depends upon the square root of the ratio of L/C [3, 4]; the structure should exhibit larger BW for E_x incidence as compared to E_y incidence. For incident waves having both E_x and E_y components, the BW will increase as E_x increases and decrease as E_y increases. For E_x, the major impedance contribution comes from the inductances of the left-side complement, while for E_y, the major contributions come from the capacitances of the right-side complement. For E_x, the equivalent circuits of the two complements of the cell are connected in series while for E_y, they are connected in parallel. For both cases, they ultimately form an SRG. To maintain the same f_0 along the x and y directions, the product of the equivalent L and C contributing to the resonance in both directions must match. The proposed structure is designed and optimized in such a way that the above condition is satisfied. Therefore, changing the basic structure will result in the loss of the polarization-independent response.

5.3 Simulated response of the AMC

In order to analyze the AMC unit cell, periodic boundary conditions (PBCs) are added to all four sides of the unit cell in the xy plane as discussed in Subsection 3.12 C of Chapter 3.

The AMC unit cell is subjected to a normally incident plane wave (theta, $\theta = 0°$) and the E-field polarization angle phi, ϕ, is varied. For $\phi = 0°$, the normally incident wave has E-field along y-axis while for ϕ = 90°, the *E*-field lies along x-axis. Fig. 5.3(a) shows that f_0, which is 6.48GHz, remains constant for all these variations. As analyzed in the previous section, the BW increases as the value of ϕ increases from ϕ = 0° (85MHz) when *E* lies entirely along the y-axis, to ϕ = 90° (500MHz) when E lies entirely along the x-axis. The response of the structure to both TE and TM polarized waves for various incident angles (θ) is presented in Fig. 5.3(b). It can be seen that the BW decreases with an increase in θ for TE waves, and increases with an increase in θ for TM waves. This observation is similar to [6, 7].

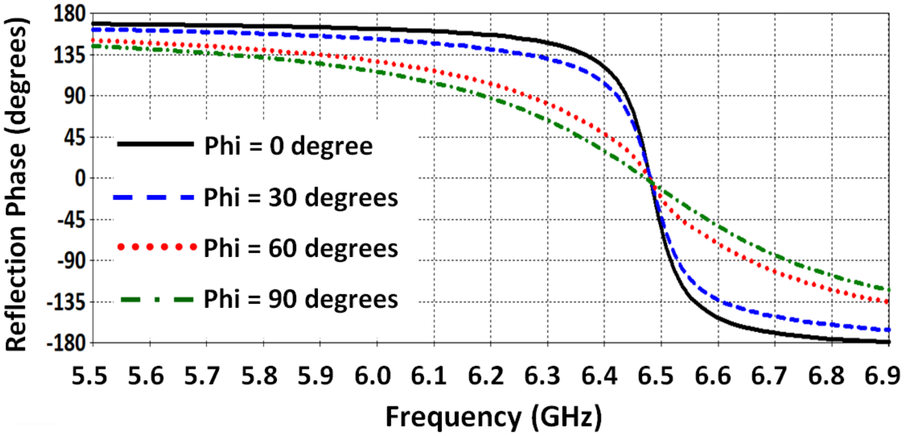

(a)

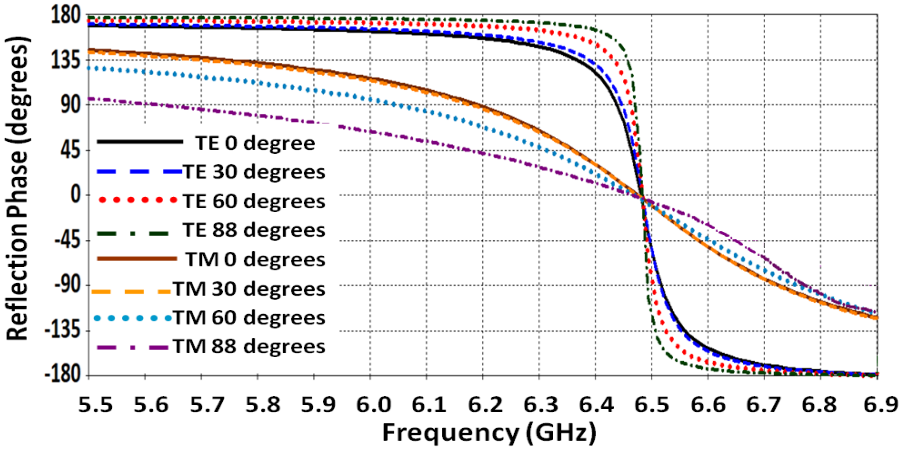

(b)

Fig. 5.3 (a) Simulated reflection phase for different E-field polarization angles phi (ϕ) and normal incidence (θ = 0°). (b) Simulated TE/TM reflection phase for different incident angles (θ).

It can also be seen from Fig. 5.3(b) that for TE incidence, f_0 remains fixed at 6.48 GHz with varying θ. The ±90° reflection phase BW decreases from 85 MHz (θ = 0°) to 33 MHz (θ = 88°). For TM incidence, f_0 also remains constant throughout the angular variations at 6.48

GHz. The ±90° reflection phase BW increases from 500 MHz ($\theta = 0°$) to 1.15 GHz ($\theta = 88°$). The reflection phase magnitudes in all the cases of Fig. 5.3 are very close to 1 and are not plotted separately.

5.4 Evaluation of the Equivalent Circuit Parameters

The values of the inductances and capacitances of the unit cell shown in Figs. 5.1(b) and (c) are obtained in this section. The approximate values of the inductances (L) are calculated using the following equation [9]

$$L(nH) = 2\times10^{-4}\times10^{3}\times l\times[\ln\left(\frac{l}{w+t}\right)+1.193+0.2235\left(\frac{w+t}{l}\right)]K_g$$

(5.1)

with $$K_g = 0.57 - 0.145\ln\frac{w}{h}; \quad \frac{w}{h} > 0.05,$$

where l = length of the conducting strip, w = width of the conducting strip, t = metallization thickness = 0.035mm and h = substrate thickness = 1.52mm. The value of the inductance of the grounded dielectric can be calculated approximately as $L_d = \mu_0 h$, where μ_0 = free-space permittivity. The approximate values of the capacitances (C) are calculated using the following equation [10]

$$C = e\left[\varepsilon_0\frac{K'(k)}{K(k)} + \varepsilon_0\frac{(\varepsilon_r - 1)}{2}\frac{K'(k_1)}{K(k_1)}\right]$$

(5.2)

with $$K'(k) = K(k'); \quad k = \frac{g}{g+2w}; \quad k'^2 = 1-k^2 \text{ and } k_1 = \frac{\sinh(\pi g/4h)}{\sinh(\pi(g+2w)/4h)}.$$

K(k) = complete elliptic integral of the first kind, e = length of the capacitor, g = gap between the plates, w = width of the conductor and h = dielectric thickness.

The calculated values of the equivalent circuit parameters for both E_x and E_y incidence using (5.1) and (5.2) are shown in Table 5.1. The equivalent circuits of Figs. 5.1(b) and (c) are then drawn in Advanced Design System (ADS) and the theoretical values calculated in Table 5.1

are plugged into the circuits. The responses of the circuits are then observed. Finally, the values of the inductances and capacitances are optimized so that the equivalent circuit response for E_y incidence matches the phi = 0^0 curve of Fig. 5.3(a) and the equivalent circuit response for E_x incidence matches the phi = 90^0 curve of Fig. 5.3(b).

Table 5.1. Approximate theoretical values of the equivalent circuit parameters.

For E_y incidence (Fig. 5.1(b))		
C_{cy} = 0.71pF (g=2mm, w=1.6mm, e=1.6mm)	L_{1y} = 2.5nH (w=1.6mm, l=8.8mm)	L_{cy} = 0.5nH (w=1.6mm, l =2mm)
C_{1y} = 2.21pF (g=1.6mm, w=2mm, e=3.25mm)	L_{2y} = 0.49nH (w=3.25mm, l=3.6mm)	C_{2y} = 1.6pF (g=1.6mm, w=3.6mm, e=1.6mm)
C_{3y} = 1pF (g=1.6mm, w=5.4mm, e=1.15mm)	L_{3y} = 2.1nH (w=2.15mm, l = 8.8mm)	L_d=1.8nH
For E_x incidence (Fig. 5.1(c))		
C_{c1x} = 1.48pF (g=2mm, w=6mm, e=1.6mm)	C_{c2x} = 0.5pF (g=4.3mm, w=1.6mm, e=1.6mm)	L_{1x} = 2nH (w=1.6mm, l =6mm)
L_{2x} = 0.72nH (w=1.6mm, l =3.25mm)	L_{3x} = 2.77nH (w=1mm, l=7mm)	L_{4x} = 0.4pF (w=3.6mm, l=3.25mm)
C_{1x} = 1.9pF (g=1.6mm, w=2.2mm, e=3.6mm)	L_{cx} = 0.45nH (w=1.6mm, l =2.15mm)	L_d=1.8nH

Table 5.2. Optimized values of the equivalent circuit parameters.

For E_y incidence (Fig. 5.1(b))		
C_{cy} = 0.79pF	L_{1y} = 0.7nH	L_{cy} = 1.3nH
C_{1y} = 2.1pF	L_{2y} = 0.46nH	C_{2y} = 1.49pF
C_{3y} = 1.1pF	L_{3y} = 1.15nH	L_d = 1.54nH
For E_x incidence (Fig. 5.1(c))		
C_{c1x} = 1.6pF	C_{c2x} = 0.32pF	L_{1x} = 7.1nH
L_{2x} = 0.65nH	L_{3x} = 3.46nH	L_{4x} = 1.15pF
C_{1x} = 1.16pF	L_{cx} = 2.8nH	L_d =1.54nH

The optimized values of the circuit parameters are now presented in Table 5.2. The theoretical and optimized values of the capacitances are quite close to one another.

However, it is noted that the values of some of the inductances after optimization are very different from the theoretical value of Table 5.1. This is because Equation 5.1 gives the inductance of a metallic strip when it is isolated and has a uniform current throughout its length. However, in case of the unit cell of Fig. 5.1(a), the individual metallic strips are interconnected, and the currents induced along them do not necessarily have uniform magnitudes along the entire lengths of the strips. So, (5.1) is used simply to get a rough estimate of the inductance values with the aim of optimizing them through ADS to get the desired responses.

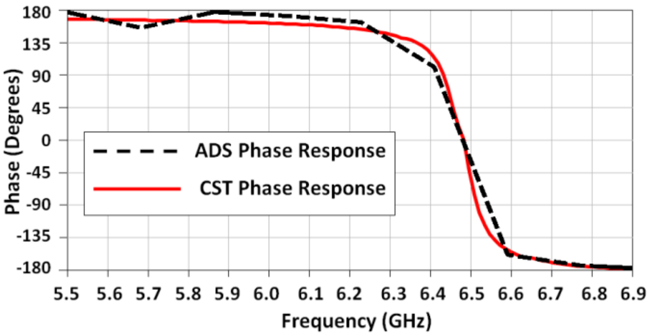

(a)

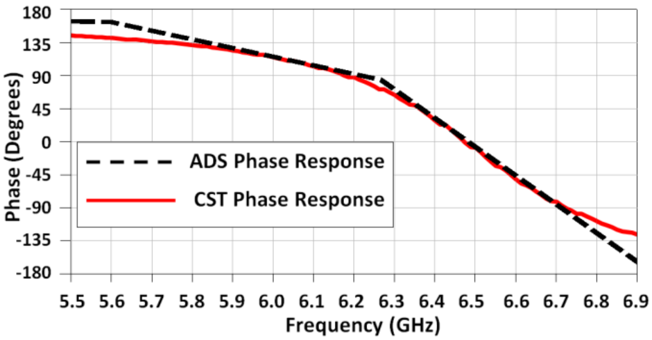

(b)

Fig. 5.4. CST and ADS response comparison for (a) E_y incidence and (b) E_x incidence.

The comparisons between the ADS and CST unit cell responses using the optimized circuit parameters are plotted in Fig. 5.4. It is seen that the circuits designed using the optimized parameters give an ADS response which is very close to its CST counterpart for both the E_x and E_y equivalent circuits.

5.5 Experimental Verifications

The measurements of the proposed AMC structure reflection phase are carried out in an anechoic chamber with two horn antennas working in the C band. A metal sheet of similar dimensions as the AMC structure is also used to normalize the reflection phase. The structure is placed in the far-field of the antennas and measurements are carried out. The measurement configurations are illustrated in Fig. 5.5 (a) and (b).

The two horn antennas are connected to the VNA ports. The Port extension feature of the VNA is used bring the reference planes to the horn antenna feed locations. In order to get the phase measurements of the metasurface, two sets of measurements have to be taken. First, the phase of the metasurface kept at a distance *d* from the horn antennas is taken for normal incidence as shown in Fig. 5.5(a) left. This is considered φ_{MS}. Then, the metasurface is replaced by a metal sheet having the same dimensions as the metasurface and kept exactly at the same location as the metasurface as shown in Fig. 5.5(a) right. The phase is again measured. This is considered φ_{PEC}. In order to get the phase response of the metasurface, we perform $\varphi_{MS} - \varphi_{PEC} + \pi$. The π is added to account for the reflection phase. This gives us the reflection phase of the metasurface. The measurement configurations for TE and TM measurements are shown in Fig. 5.5(b). For each angle Θ, the metasurface is replaced with the metal sheet to get the reference phase like the normal incidence case.

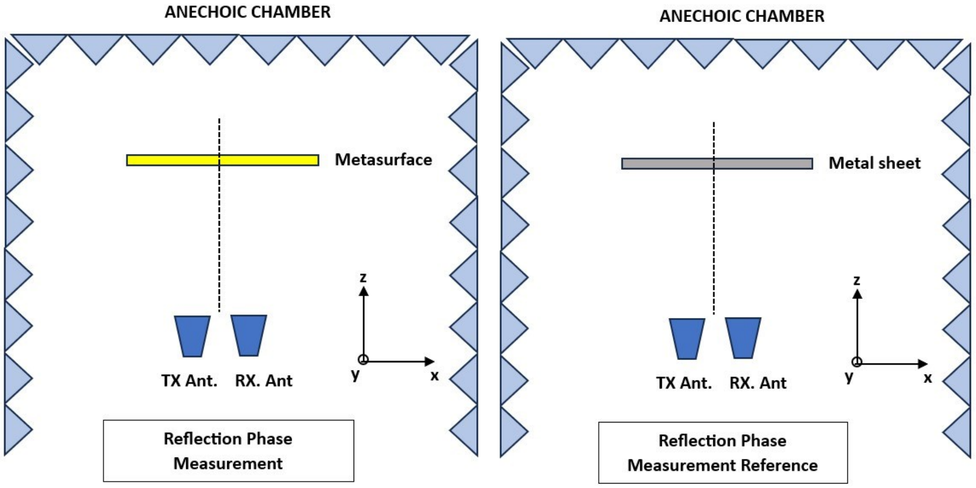

(a)

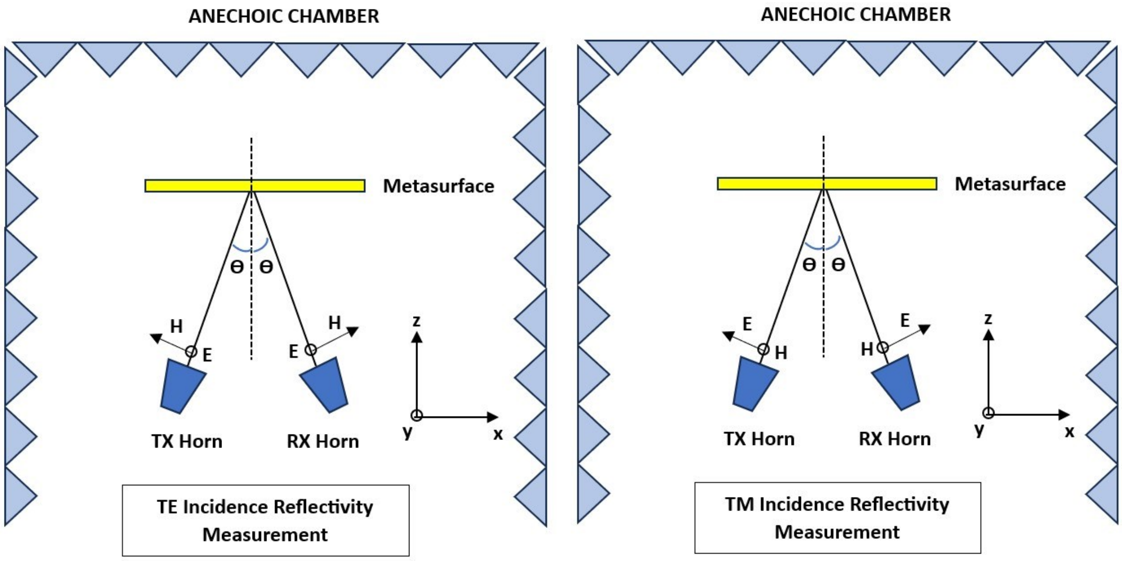

(b)

Fig. 5.5 (a) Phase measurement configurations for normal incidence. (b) TE and TM incidence phase measurement configurations.

In order to experimentally verify the simulation results, a prototype of the AMC with 14 x 14 unit cells (196mm x 196mm) is fabricated as shown in Fig. 5.6(a).

The polarization independent behavior of the structure is confirmed by the measured plots of Fig. 5.6(b). A constant resonant frequency of 6.48GHz is maintained while ϕ changes from 0° to 90°. The ±90° reflection phase BW also increases from 87MHz (1.4%) for $\phi = 0°$ to 521MHz (8%) for $\phi = 90°$. The angular stability for both TE and TM waves is also confirmed from Fig. 5.6(c), which shows that there is no shift in resonant frequency f_0 for both TE and TM polarized waves.

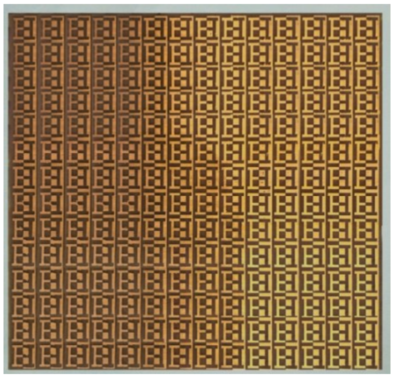

(a)

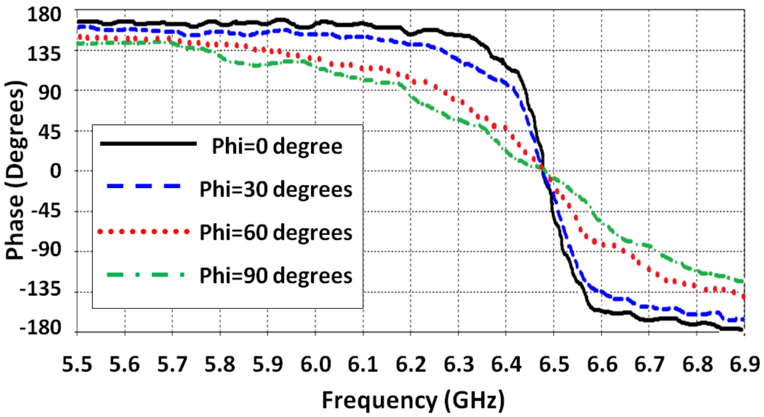

(b)

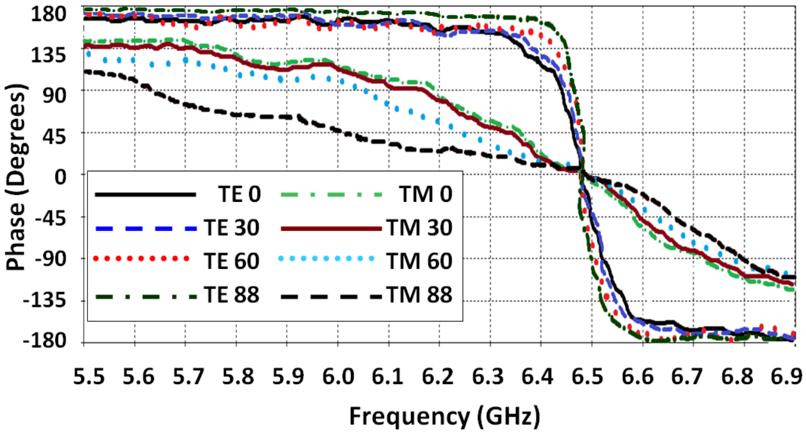

(c)

Fig. 5.6 (a) Fabricated prototype with 196 unit cells. Measured reflection phases for (b) various phi and (c) various TE and TM oblique incidence angles.

The TE BW decreases from 87MHz (1.4%) to 36MHz (0.6%) with f_0 = 6.48GHz while the TM BW increases from 521MHz (8%) to 1.18GHz (18.21%) with f_0 = 6.48GHz as θ varies from 0° to 88°. The AMC exhibits large BW for TM polarized waves while the BW is relatively narrow for TE waves.

A comparison of the angular stability of the presented structure with the best angular stabilities reported in the literature is provided in Table 5.3 with λ_0 = free space wavelength at the frequency where reflection phase = 0^0. It is noted that the SCUC has higher angular stability than other previous works.

Table 5.3. Comparisons with previous works.

Ref.	ε_r	Unit cell size	Thickness, h	Angular stability
[3]	10.2	$\lambda_0/10.5$	$\lambda_0/24$	76^0
[4]	13	$\lambda_0/6.5$	$\lambda_0/34$	75^0
[4]	13	$\lambda_0/10.6$	$\lambda_0/30$	80^0
[6]	10.2	$\lambda_0/17$	$\lambda_0/57$	75^0
[8]	13	$\lambda_0/7.2$	$\lambda_0/37$	77^0
This work	4.4	$\lambda_0/3.4$	$\lambda_0/30.4$	88^0

5.6 Conclusions

This chapter presents an artificial magnetic conductor (AMC) with self-complementary unit cells (SCUCs). The use of SCUCs results in very high angular stability of the structure; up to an incident angle of 88° for both transverse electric and transverse magnetic polarized incident waves with no shift in the resonant frequency f_0. No other structure in literature has zero frequency shifts throughout the whole range of incident angle variations. Another interesting feature of this structure is the gradual increase of the ±90° reflection phase bandwidth with an increase in E-field polarization angle from $\phi = 0°$ to $\phi = 90°$ while maintaining the same f_0. These two features make the structure unique and useful in applications where angular stability and polarization independent f_0 are the primary concerns.

REFERENCES

[1] M. E. de Cos, Y. Alvarez, R. C. Hadarig, et al., "Novel SHF-band uniplanar artificial magnetic conductor," *IEEE Antennas Wirel. Propag. Lett.*, vol. 9, pp. 44–47, 2010.

[2] M. E. de Cos, Y. Alvarez, and F. Las-Heras, "Novel broadband artificial magnetic conductor with hexagonal unit cell," *IEEE Antennas Wirel. Propag. Lett.*, vol. 10, pp. 615–618, 2011.

[3] M. Hosseini, A. Pirhadi, and M. Hakkak, "Design of an AMC with little sensitivity to angle of incidence using an optimized Jerusalem cross FSS," *Proc. IEEE Int. Workshop on Antenna Technology Small Antennas and Novel Metamaterials*, White Plains, NY, USA, March 2006, pp. 245–248.

[4] M. Hosseini, A. Pirhadi, and M. Hakkak, “Design of a novel AMC with little sensitivity to the angle of incidence and very compact size,” *IEEE Antennas and Propagation Society Int. Symp*., Albuquerque, NM, USA, July 2006, pp. 1939–1941.

[5] C. R. Simovski, P. de Maagt, and I. V. Melchakova, “High-impedance surfaces having stable resonance with respect to polarization and incident angle,” *IEEE Trans. Antennas Propag*., vol. 53, no. 3, pp. 908–914, 2005.

[6] R. C. Hadarig, M. E. de Cos, and F. Las-Heras, “Novel miniaturized artificial magnetic conductor,” *IEEE Antennas Wirel. Propag. Lett*., vol. 12, pp. 174–177, 2013.

[7] G. Gampala, and A. B. Yakovlev, “Wideband high impedance surface for X-band antenna applications,” *IEEE Antennas and Propagation Soc. Int. Symp*., Honolulu, HI, June 2007, pp. 1329–1332.

[8] D. J. Kern, D. H. Werner, A. Monorchio, “The design synthesis of multiband artificial magnetic conductors using high impedance frequency selective surfaces,” *IEEE Trans. Antennas Propag*., vol. 53, no. 1, pp. 8–17, 2005.

[9] K. C. Gupta, R. Garg, I. Bahl. P. Bhartia, *Microstrip Lines and Slotlines,* 2nd ed., Norwood, MA, USA: Artech House, Inc., 1996.

[10] J. D. Ortiz *et al.,* “Self-complementary metasurface for designing narrow band pass/stop filters,” IEEE Microw. and Wirless Comp. Lttrs., vol. 23, no. 6, pp. 291-293, June 2013.

CHAPTER 6

FPC ANTENNA WITH AMC GROUND AND REDUCED CAVITY HEIGHT

6.1 Objective

As discussed in Sec. 3.2 of Chapter 3, the EM radiation of an antenna placed within a resonant Fabry-Pérot Cavity (FPC) and designed to operate at the resonant frequency of the FPC is highly directive in nature. Such an antenna is called an FPC Antenna or an FPCA in short. It is used in cases where a high gain is needed, and the size of the antenna is not a major constraint.

One inherent disadvantage of the conventional FPCA is its narrow 3dB gain bandwidth. This is because the cavity resonance condition is satisfied at only a single frequency, f_r and the field interference within the cavity becomes less constructive as we move away from f_r. This leads to a reduction in the directivity of the radiated beam. The 3dB gain bandwidth (BW) is therefore an effective measure of how wideband an FPCA actually is.

One way to increase the 3dB gain BW of FPCAs is by using a PRS whose reflection coefficient phase increases with frequency. This ensures that the resonance condition is satisfied even when the frequency is increased. This method is used in [1] and [2] to achieve wider 3dB gain BWs. However, both these antennas use two or more PRS layers to achieve a wider bandwidth. This leads to an increased cavity height and bulky configuration. The positive reflection phase gradient can also be achieved by using a single PRS layer. In [3], the authors use a single PRS layer with metallization on both sides of the substrate to achieve a positive reflection phase gradient.

The main objective of this chapter is to design a dual-band FPCA with reduced cavity height which uses only a single PRS layer with positive reflection phase gradients within both operating bands - the 2.4GHz and 5.8GHz WLAN bands. The reduced cavity height and single PRS layer makes the FPCA compact and rigid while the positive reflection phase of the PRS gives it good 3dB gain BWs within both the operating bands. An AMC is used as the antenna ground plane. The cavity height is reduced by manipulating the reflection phases of both the PRS and AMC ground plane.

6.2 PRS and AMC Unit Cell designs

All simulations are performed in CST Studio Suite. The unit cells are analyzed with PBCs on all four sides of the xy plane. Both the antenna with AMC ground plane and the PRS are designed on FR-4 substrates ($\varepsilon_r = 4.2$, $\tan\delta = 0.02$, thickness = 1.52 mm). The metal layer used in all the designs is Copper with $\sigma = 5.8 \times 10^7$ S/m.

6.2.1 PRS Unit Cell

In [9], the authors use two periodic arrays of closely resonating structures, each printed on the opposite side of a dielectric substrate, to design a PRS which achieves a positive reflection phase gradient. Using the same principle, the proposed PRS also consists of two arrays of closely resonating elements printed on either side of the FR-4 substrate. However, the resonating elements used in this chapter are different from the ones used in [3]. The top and bottom unit cells of the proposed PRS are shown in Fig. 6.1.

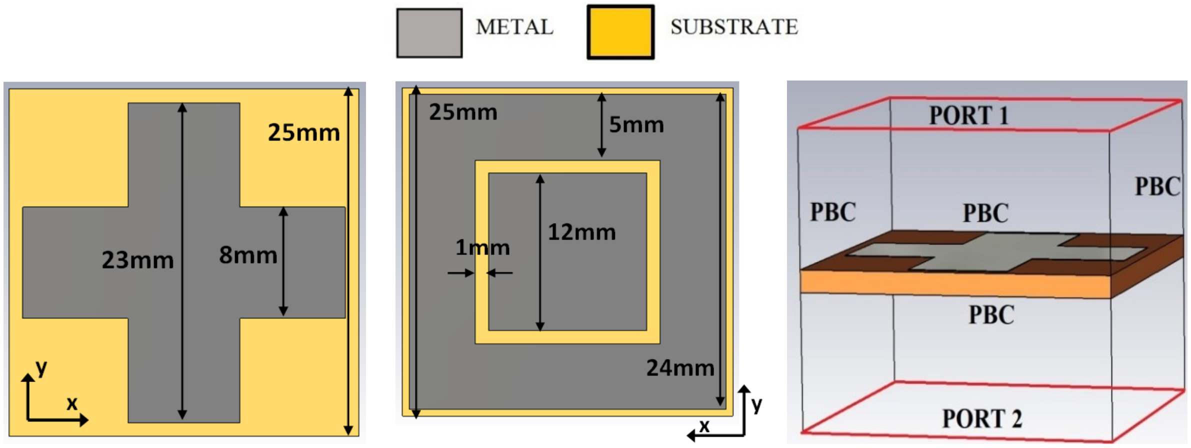

(a) (b) (c)

Fig. 6.1. PRS (a) top, (b) bottom and (c) CST analysis ports and PBCs.

The top unit cell consists of a cross-shaped printed metallic structure while the bottom unit cell consists of a square patch present inside a square loop. The resonating structures on the top (Fig. 6.1(a)) and bottom (Fig. 6.1(b)) together help in creating a positive reflection phase gradient. The dimensions of the top and bottom unit cells are optimized by varying the gaps and element dimensions until the positive reflection phase gradients lie within the two bands of operation. Since the PRS allows transmission of EM waves through it at certain frequencies, the information of both Port 1 and Port 2 of Fig. 6.1(c) are required.

The simulated phases and magnitudes of the reflection coefficients in the two bands are shown in Fig. 6.2. The positive reflection phase gradient extends from around 2.3GHz to 2.5GHz in the first band and from 5.7GHz to 5.9GHz in the second band. It can be seen that the reflection coefficient magnitudes are quite high, which should result in high gain enhancement [4].

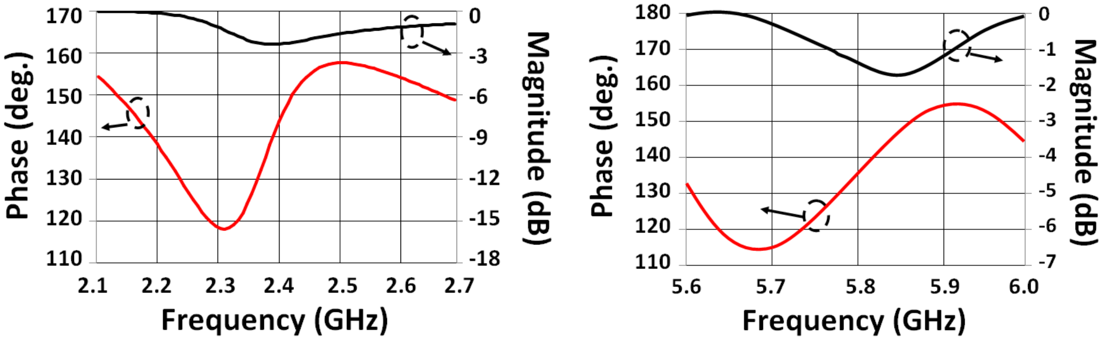

(a) (b)

Fig. 6.2. Reflection coefficient magnitudes and phases of the PRS within the (a) 2.4GHz band and (b) 5.8GHz band.

The reflection phases at 2.4GHz and 5.8GHz are 145° and 135° respectively. These values will be required in calculations performed in the following section.

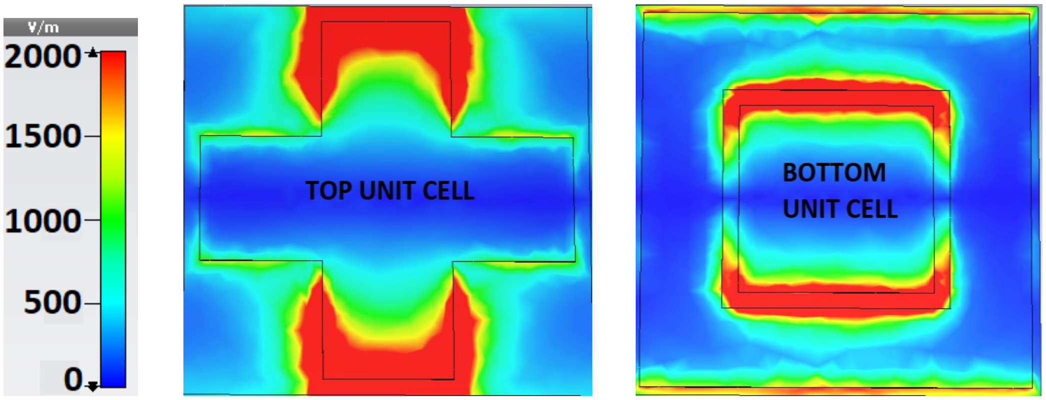

(a) (b)

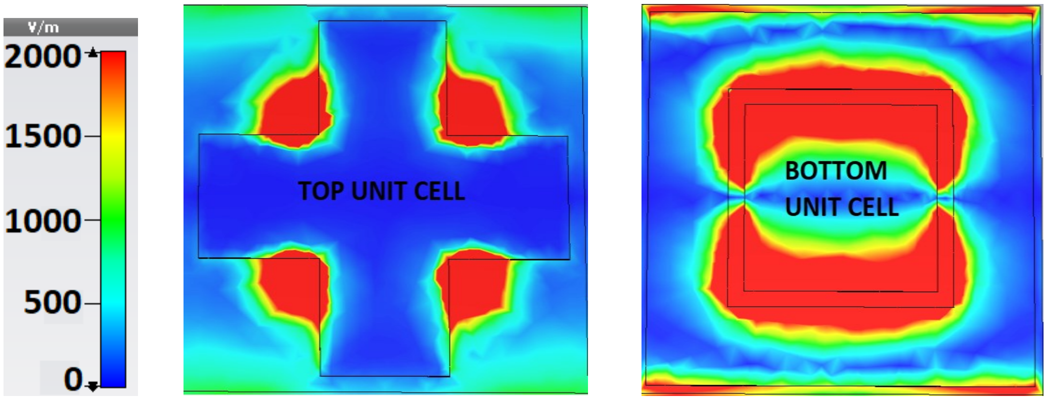

(c) (d)

Fig. 6.3. E-field distributions (V/m) at (a, b) 2.4GHz and (c, d) 5.8GHz.

The E-field distributions on the top and bottom geometries of the PRS unit cell are shown in Fig. 6.3. In the bottom geometry, most of the E-fields are concentrated in the gap between the outer square loop and inner square patch at both 2.4GHz and 5.8GHz. In the top geometry, the E-fields are concentrated along the upper and lower portions of the cross at 2.4GHz and along the four corners of the cross at 5.8GHz. The interactions of the top and bottom geometries help in generating positive reflection phase gradients at both 2.4GHz and 5.8GHz.

6.2.2 AMC Ground Plane

The resonance condition of the FPC discussed in Chapter 3 is presented here once again for convenience. The equation is as follows:

$$(-\frac{4\pi}{\lambda})L + \varphi_{GND} + \varphi_{PRS} = 2\mathrm{N}\pi; \quad \mathrm{N} = 0, \pm 1, \pm 2\ldots. \tag{6.1}$$

where L = FP cavity height, φ_{GND} = reflection phase of the ground plane and φ_{PRS} = reflection phase of the PRS layer at the frequency corresponding to λ.

Equation 6.1 tells us that the Fabry-Perot cavity height L depends on the reflection phases of both the PRS layer and the ground plane (it depends on the sum of φ_{PRS} and φ_{GND}). Therefore, L can be reduced significantly by manipulating φ_{GND} and φ_{PRS}. Variations of φ_{GND} can be achieved by using an AMC ground plane instead of the normal metallic ground plane which has a fixed φ_{GND} of -π radians. If the cavity height L, resonance frequency f_r and PRS reflection phase φ_{PRS} are fixed, then the value of φ_{GND} required to satisfy (6.1) can be calculated.

In this chapter, L is fixed at $(\lambda_{2.4\text{GHz}})/6$ (≈ 20 mm). The reflection coefficient phase of the PRS, φ_{PRS}, is 145° at 2.4GHz and 135° at 5.8GHz (obtained in Subsection 6.2.1). To calculate the required value of φ_{GND} at 2.4GHz, we put f_r = 2.4GHz, φ_{PRS} = 145°, N = 0 and L = 20 mm in (6.1). This yields φ_{GND} = –25°. The required value of φ_{GND} at 5.8GHz can be calculated similarly by putting f_r = 5.8GHz, φ_{PRS} = 135°, N = 1 and L = 20 mm in (6.1). This results in φ_{GND} = 144°. Therefore, the designed AMC ground plane should exhibit a reflection phase of –25° at 2.4GHz and 144° at 5.8GHz in order to satisfy the cavity resonance condition. The designed unit cell of the AMC ground plane and its reflection coefficients are shown in Fig. 6.4. It can be seen that the reflection phases are very close to the calculated values at both 2.4 GHz and 5.8GHz.

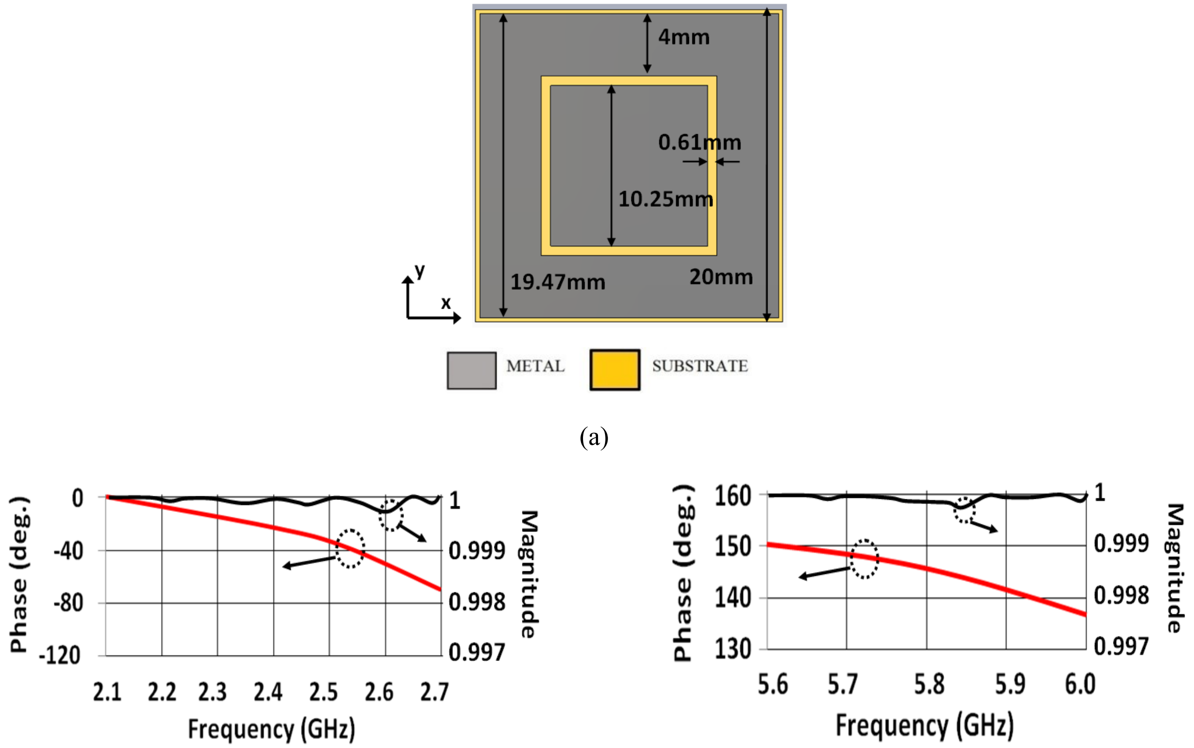

(a)

(b) (c)

Fig. 6.4 (a) AMC unit cell geometry. (b) Reflection coefficients within the (b) 2.4GHz and (c) 5.8GHz bands.

Observing the reflection phases of the PRS and the AMC within the two frequency bands from Figs. 6.2 and 6.4, it can be concluded that $\varphi_{GND} + \varphi_{PRS}$ increases with frequency from 2.3GHz to2.5GHz and from 5.7GHz to 5.9GHz.

6.3 Patch Antenna

A patch antenna with asymmetric cross slots and diagonally opposite truncated corners is designed to act as the radiator. The antenna is fed via a coaxial cable located near the edge of a microstrip line, as shown in Fig. 6.5(a).

If a patch antenna is designed with only the corner truncations, it radiates an RHCP wave near 2.5GHz. After the addition of the asymmetric cross slots, the patch radiates an RHCP wave at 2.4GHz as well as an additional LP wave at 5.8GHz. The current distributions of the patch antenna at 2.4GHz and 5.8GHz are shown in Figs. 6.5(b) and (c). The addition of the slots serves two purposes. It shifts the first band slightly to the left (from 2.5GHz to 2.4GHz; due to increased current path length) and adds a second resonance near 5.8GHz.

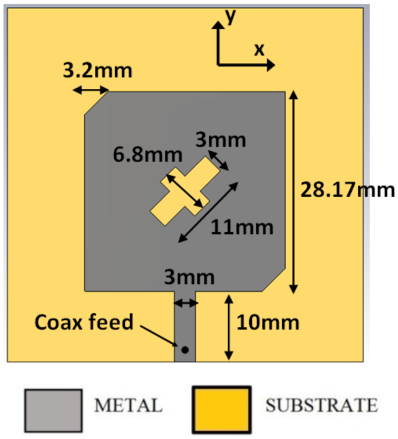

(a)

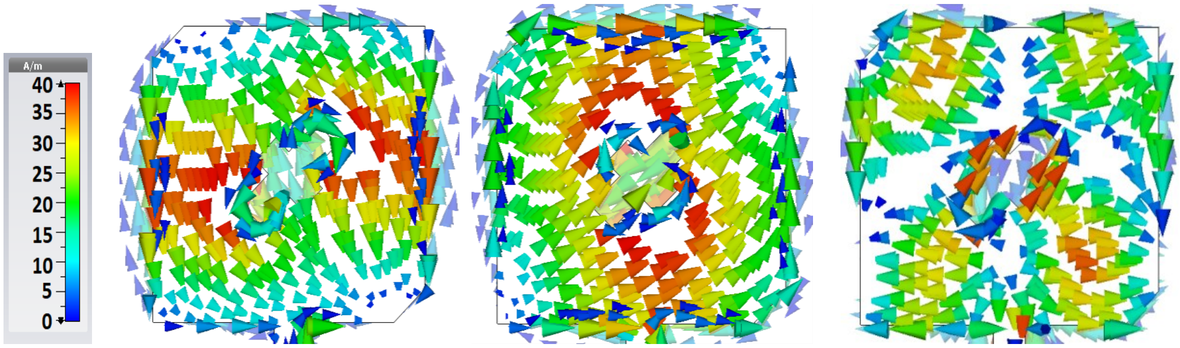

Phase 0^0

Phase 90^0

(b)

(c)

Fig. 6.5 (a) Patch antenna geometry. Induced surface currents (A/m) at (b) 2.4GHz and (c) 5.8GHz.

The widths of the slots are made equal. Increasing/decreasing the widths results in left/right shift of the first resonance due to the increased/decreased current path length. The current concentration around the slots at 5.8GHz can be observed from Fig. 6.5(c). Since the current are concentrated along both the cross slots, the lengths of both the shorter and longer slots affect the 5.8GHz band. Additionally, the longer slot also affects the 2.4GHz band. Therefore, the two bands can be adjusted and shifted by varying the lengths of the cross slots.

6.4 Fabry-Pérot Cavity Antenna

The proposed FPCA is shown in Fig. 6.6(a). The patch antenna described in the previous section is used as the primary radiator. It is placed on the AMC ground plane where it is surrounded by 40 AMC unit cells. The gaps between the patch and the AMC unit cells are shown in Fig. 6.6(a). The PRS layer, consisting of 25 unit cells, is placed above the patch antenna-AMC ground plane layer. Although the initial height of the cavity was fixed at 20mm (≈ ($\lambda_{2.4GHz}$)/6), the final cavity height was chosen to be 22.5mm after optimization. To verify the simulation results, a prototype of the simulated antenna is fabricated as shown in Fig. 6.6(b). A vector network analyzer (VNA) from Agilent Technologies having model number E5071B (300kHz to 8.5GHz) is used for all measurements. The S_{11} of the antenna under test (AUT) is measured by connecting it to the VNA. The radiation patterns, gains, and axial ratio of the AUT are measured inside an anechoic chamber. The measurement setup is shown in Fig. 6.6(c).

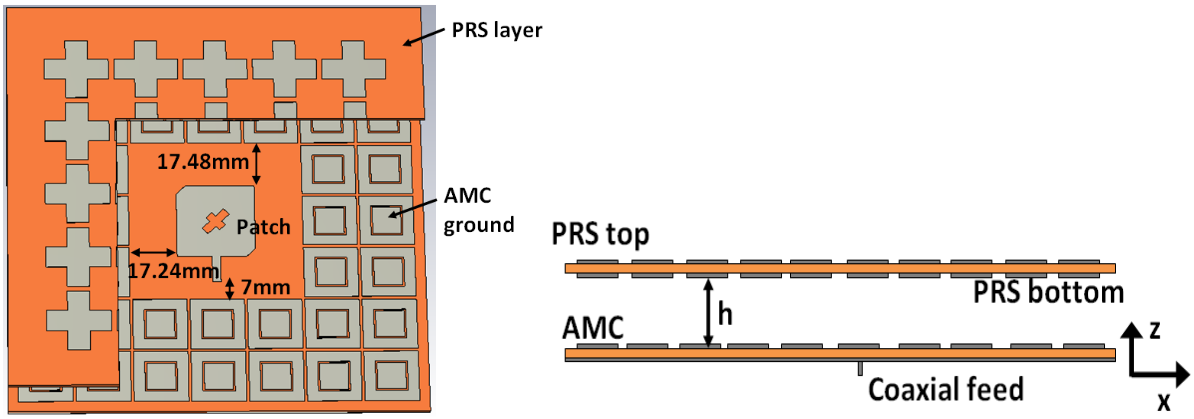

Perspective View

End View

(a)

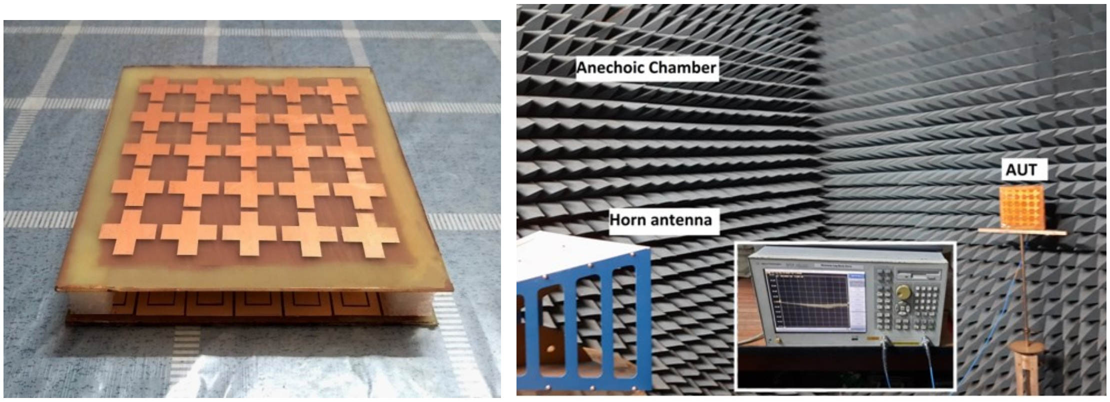

(b) (c)

Fig. 6.6 (a) Simulated FPCA. (b) Fabricated FPCA and (c) Measurement setup with inset picture of the VNA.

6.4.1 Experimental Verifications

The reflection coefficient curves of the FPCA are shown in Figs. 6.7(a) and (b). The red dashed lines labeled "Patch" in both the figures represent S_{11} of the unloaded patch antenna (described in Sec. 6.3). It can be seen that there is not much difference between S_{11} values for the unloaded patch and the FPCA. This means that the loading effect of the AMC ground plane and the PRS layer on the patch antenna is minimal. The FPCA achieves a –10dB S_{11} BW of 8.1% (2.31GHz–2.52GHz) in the 2.4GHz band and 6.1% (5.61GHz–5.96GHz) in the 5.8GHz band. It can be observed from Fig. 6.7(c) that the loading of the AMC ground and PRS layer slightly increases the AR magnitude of the patch antenna without changing the 3dB AR-BW. The FPCA achieves a 3dB AR-BW of 7.9% (2.31GHz–2.49GHz). The measurement configurations are the same as shown in Fig. 4.5 of Chapter 4. The Axial Ratio and sense of CP are measured as discussed in the first two paragraphs of page 59 (Chapter 4).

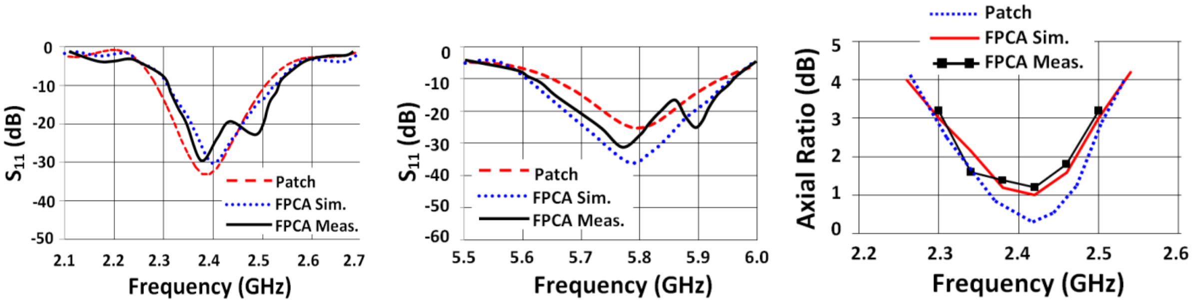

(a) (b) (c)

Fig. 6.7. S_{11} parameters of the FPCA within (a) 2.4GHz band and (b) 5.7GHz band.
(c) AR vs. freq within 2.4GHz band.

Near field contour plots shown in Fig. 6.8 demonstrate the fact that the *E*-field magnitude is uniform throughout the FP cavity at 2.4GHz while it is concentrated near the central portion of the cavity at 5.8GHz.

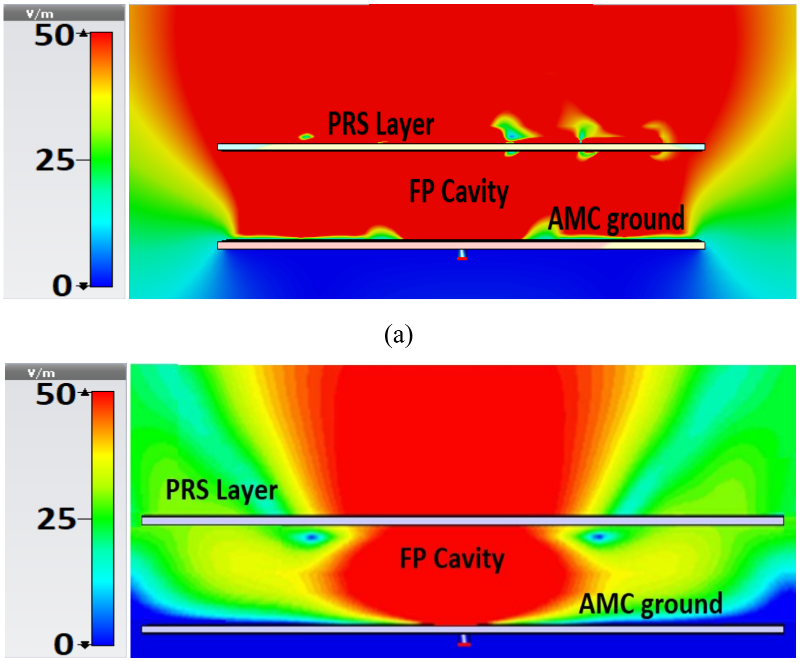

(a)

(b)

Fig. 6.8. E-field distributions (V/m) within the FP cavity at (a) 2.4GHz and (b) 5.8GHz.

The gain enhancements achieved by the FPC at both 2.4GHz and 5.8GHz are clearly visible by observing the radiation patterns of Fig. 6.9. Compared to the unloaded patch antenna, the peak gain of the FPCA is increased by around 9dB in the first band and around 8dB in the second band. The proposed antenna has a peak measured gain of 14.3dBi (14.1dBic RHCP) at 2.4GHz and 15.5dBi at 5.8GHz.

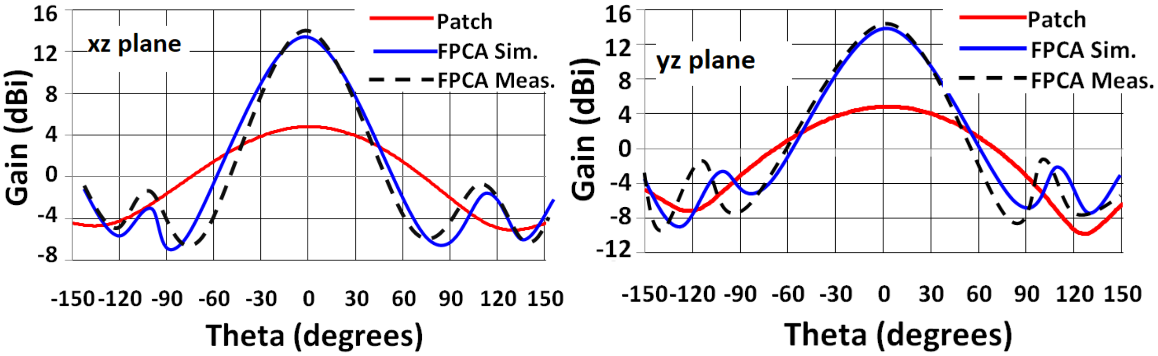

(a)

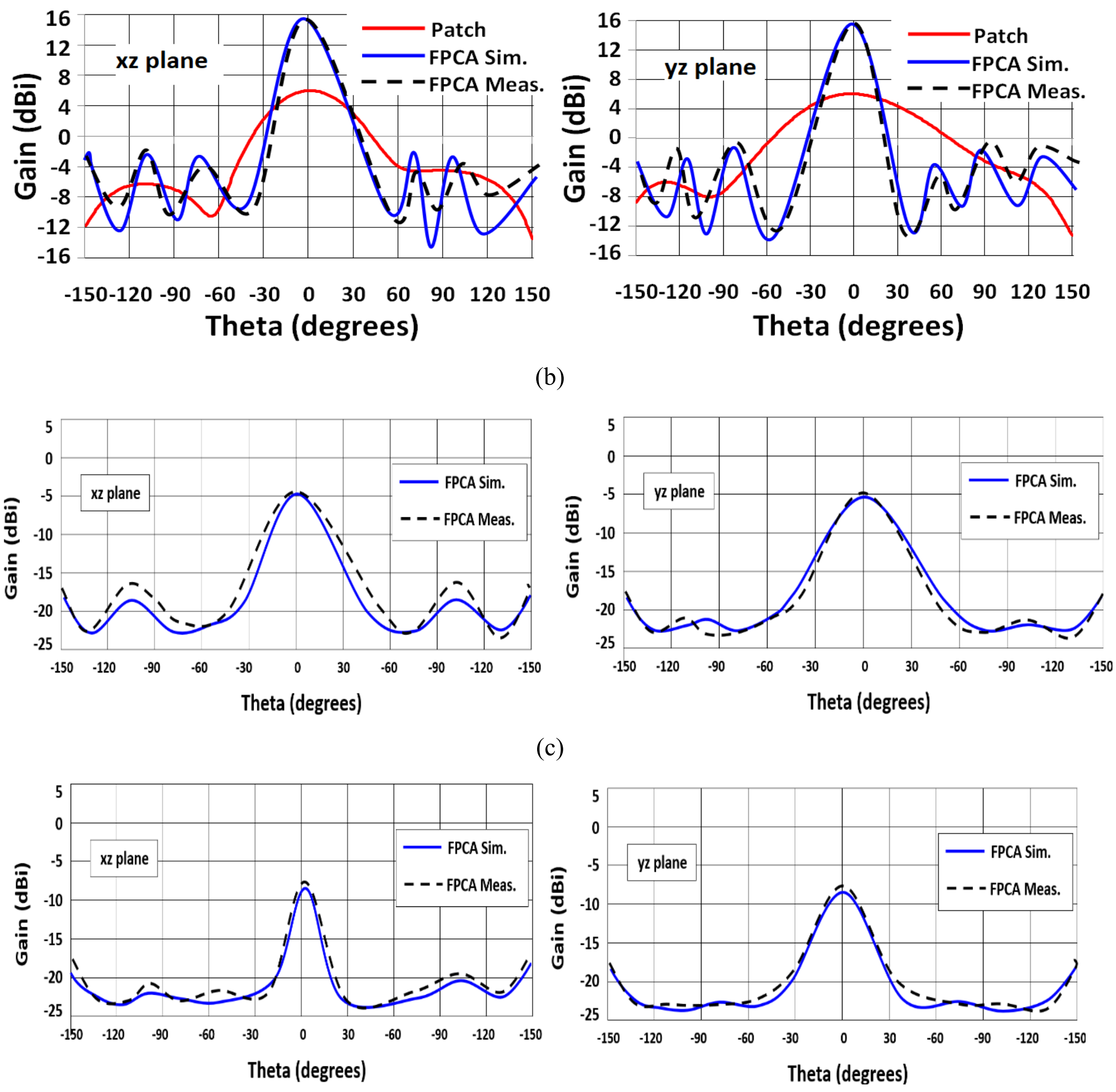

(b)

(c)

(d)

Fig. 6.9. Far field radiation patterns at (a) Co-pol 2.4GHz, (b) Co-pol 5.8GHz, (c) Cross-pol (opposite handedness) 2.4GHz and (d) Cross-pol 5.8GHz.

The cross-polarized radiation pattern at 2.4GHz is measured using a patch antenna with opposite handedness.

The antenna achieves high efficiencies within both 2.4GHz and 5.8GHz bands. The simulated efficiency of the antenna is found to be ≥ 84% within the 2.4GHz band and ≥ 87% within the 5.8GHz band. The radiation efficiency versus frequency plot is shown in Fig. 6.10(a).

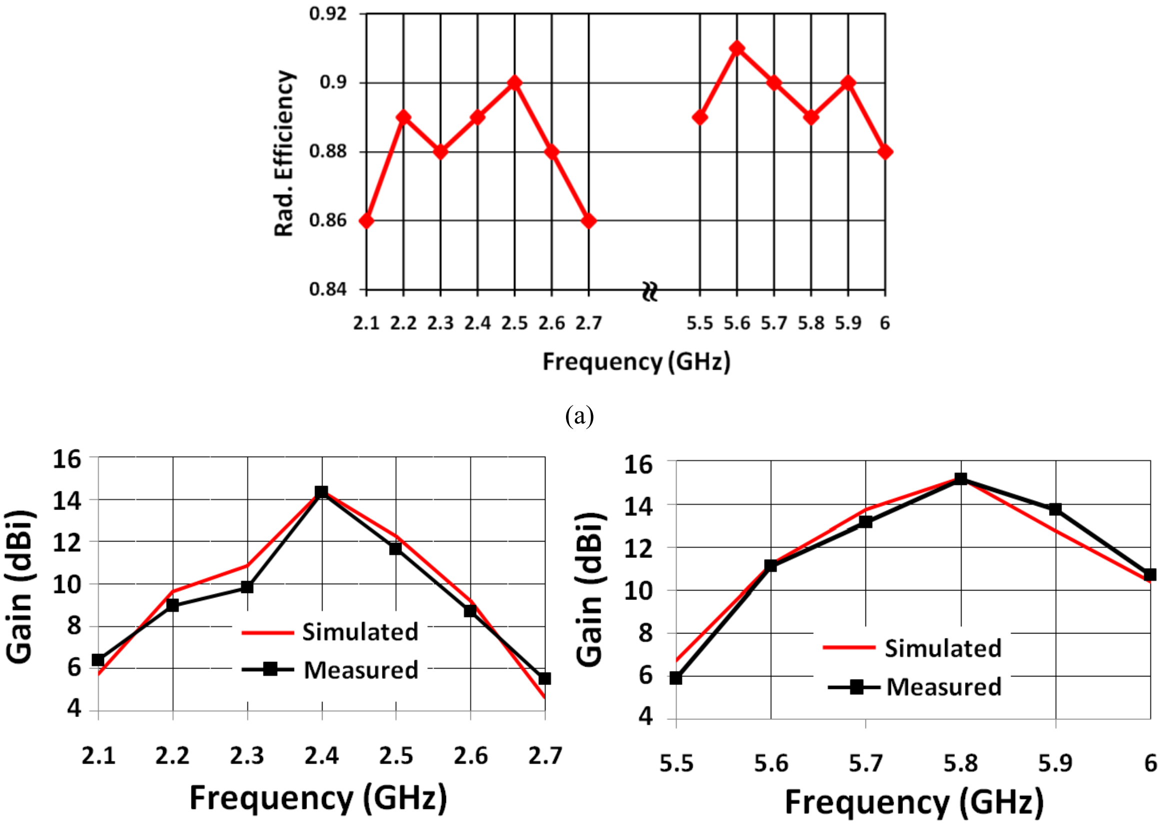

(a)

(b) (c)

Fig. 6.10. (a) Simulated radiation efficiencies within the two bands.
Peak gain vs. frequency plots within the (b) 2.4GHz band and (c) 5.8GHz band.

Figures 6.10(b) and (c) present the peak gain vs. frequency plots of the FPCA in both the frequency bands. The antenna achieves a 3dB gain BW of 7.8% (2.34GHz–2.53GHz) in the first band and 5.5% (5.64GHz–5.96GHz) in the second band. Therefore, the proposed antenna achieves good 3dB gain BWs using only a single PRS layer.

In Table 6.1, the proposed antenna is compared with other dual band FPCAs found in literature. The proposed antenna has the smallest cavity height among all the antennas presented. It also has the highest 3dB gain BW in both the bands. Only the FPCA presented in [11] has a higher 3dB gain BW in the second band. However, it uses two PRS layers to achieve this high gain BW. Therefore, the advantages of the proposed antenna over existing dual band FPCAs are clearly highlighted in the table.

Table 6.1. Comparisons of the proposed FPCA with dual-band FPCAs found in literature.

Ref.	No. of PRS layers	Frequency bands (GHz)	Cavity height (w.r.t lower band)	Lateral dimensions (w.r.t lower band)	Gain (dBi)	3dB gain BW (%)
[5]	2	10.6 13.2	$1\lambda_{10.6GHz}$	5λ x 5λ	14.5 15	4.5 4.6
[6]	2	2.45 5.6	$0.45\lambda_{2.45GHz}$	1.3λ x 1.3λ	14.9 14	7 11
[7]	1	6.95 13	$0.5\lambda_{6.95GHz}$	2.5λ x 2.5λ	16.5 20.9	1.44 3.35
[8]	1	19.75 29.75	$0.5\lambda_{19.75GHz}$	5.3λ x 5.3λ	16.2 18.5	4.5 2.4
[9]	1	5.6 10	$0.28\lambda_{5.6GHz}$	1.5λ x 1.5λ	10.1 15.2	4.1 2.7
This work	1	2.4 5.8	$0.18\lambda_{2.4GHz}$	1.5λ x 1.5λ	14.3 (14.1dBic) 15.5	7.8 5.5

6.5 Conclusions

In this chapter, a dual-band Fabry-Pérot Cavity Antenna (FPCA) operating at two important WLAN bands (the 2.4GHz band and 5.8GHz band) is presented. It radiates RHCP waves at 2.4GHz and LP waves at 5.8GHz. The proposed antenna uses only a single PRS layer to achieve good 3dB gain bandwidth in both bands. The cavity height of the antenna is also significantly reduced by using an AMC ground plane. The dimensions of the proposed antenna are $1.5\lambda_{2.4GHz}$ x $1.5\lambda_{2.4GHz}$ x $0.18\lambda_{2.4GHz}$ (187.5mm x 187.5mm x 22.5mm) where $\lambda_{2.4GHz}$ is the free space wavelength at 2.4GHz. The antenna achieves a 3dB axial ratio bandwidth (AR-BW) of 7.9% at 2.4GHz with peak measured gains of 14.3dBi and 15.5dBi at 2.4GHz and 5.8GHz respectively. The antenna also exhibits a 3dB gain BW of 7.8% within the first band and 5.5% within the second band. The following US FCC UNII bands can be used by the antenna: U-NII-2C, U-NII-2C/3, U-NII-3, U-NII-3/4. These fall within the 5.61-5.875GHz WLAN band. The corresponding channels are: 124, 128, 132, 136, 140, 144, 149, 153, 157, 161, 165, 169, 173.

REFERENCES

[1] N. Wang, Q. Liu, C. Wu *et al.*, “Wideband Fabry-Perot resonator antenna with two complementary FSS layers,” *IEEE Transactions on Antennas and Propagation*, vol. 62, no. 5, pp. 2463–2471, 2014.

[2] K. Konstantinidis, A. P. Feresidis, P. S. Hall, “Multilayer partially reflective surfaces for broadband Fabry-Perot cavity antennas,” *IEEE Transactions on Antennas and Propagation*, vol. 62, no. 7, pp. 3474–3481, 2014.

[3] A. Lalbakhsh, M. U. Afzal, K. P. Esselle *et al.*, “Single dielectric wideband partially reflecting surface with variable reflection components for realization of a compact high-gain resonant cavity antenna,” *IEEE Transactions on Antennas and Propagation*, vol. 67, no. 3, pp. 1916–1921, 2019.

[4] G. V. Trentini, “Partially reflecting sheet arrays,” *IRE Transactions on Antennas and Propagation*, vol. AP-4, no. 4, pp. 666–671, 1956.

[5] B. A. Zeb, Y. Ge, K. P. Esselle *et al.*, “A simple dual-band electromagnetic band gap resonator antenna based on inverted reflection phase gradient,” *IEEE Transactions on Antennas and Propagation*, vol. 60, no. 10, pp. 4522–4529, 2012.

[6] M. L. Abdelghani, H. Attia, T. A. Denidni, “Dual- and wideband Fabry-Pérot resonator antenna for WLAN applications,” *IEEE Antennas and Wireless Propagation Letters*, vol. 16, pp. 473–476, 2017.

[7] F. Meng, S. K. Sharma, “A dual-band high-gain resonant cavity antenna with a single layer superstrate,” *IEEE Transactions on Antennas and Propagation*, vol. 63, no. 5, pp. 2320–2325, 2015.

[8] E. B. Lima, J. R. Costa, C. A. Fernandes, “Multiple-beam focal-plane dual-band Fabry-Pérot cavity antenna with reduced beam degradation,” *IEEE Transactions on Antennas and Propagation*, vol. 67, no. 7, pp. 4348–4356, 2019.

[9] J. Chen, Y. Zhao, Y. Ge *et al.*, “Dual-band high-gain Fabry- Pérot cavity antenna with a shared aperture FSS layer,” *IET Microwaves, Antennas and Propagation*, vol. 12, no. 13, pp. 2007–2011, 2018.

CHAPTER 7

A MULTIBAND MULTIFUNCTIONAL CHIRAL METASURFACE

7.1 Objective

The phenomenon of asymmetric transmission (AT) has already been discussed in Subsection 3.3.2 of Chapter 3. It was also noted that multi-layered chiral metasurfaces (CMSs) lacking C4 rotational symmetry can exhibit this AT phenomenon for incident LP waves. As discussed in Chapter 2, researchers have presented numerous bi-layered and multilayered MSs which can exhibit AT over the years. Although the AT phenomenon has been studied extensively, there are still a few issues that should be addressed. These are listed as follows:

(i) Multiband CMSs found in literature have reported a maximum of 3 AT bands till date.

(ii) The nature of the transmitted wave does not change in any of the AT exhibiting MSs found in literature, i.e., an LP wave is transmitted as an LP wave (only the *E*-field direction is changed) and a CP wave is transmitted as a CP wave (only the handedness is changed).

(iii) For MSs which exhibit AT of LP incident waves, the forward and backward co-polarized transmission coefficients are the same. This fact can be utilized to design a symmetric co-polarized pass-band for the MS (co-polarized transmission coefficient > 0.8).

(iv) Only a handful of the presented AT exhibiting MSs have good angular stability. Most of the other structures have poor angular stability and their operations are confined to a narrow range of incident wave angles.

The aim of this chapter is to design a CMS which has (i) good angular stability and can perform (ii) asymmetric CPC transmission of LP waves within more than 3 frequency bands, (iii) asymmetric LTC transmission and (iv) symmetric co-polarization transmission. The proposed CMS can therefore act as a propagation direction dependent LTC polarization converter as well as direction independent co-polarized pass-band filter. These added functionalities increase the usefulness of the MS. Multiple bands ensure integration with a wide range of applications in different frequency bands and make the proposed CMS very useful.

7.2 Unit Cell Geometry and Response

The microwave substrate used for the proposed CMS is Arlon AD-430 with ε_r = 4.3, tanδ = 0.003 and thickness = 1.52 mm. Copper is used to draw the metallic portions of the unit cells with $\sigma = 5.8 \times 10^7$ S/m. The unit cell design has been performed using CST Studio Suite with periodic boundary conditions (PBCs) set on all four sides. An incident wave traveling towards the –z direction is considered to be the forward wave and an incident wave traveling towards the + z direction is considered to be the backward wave. The *E*-field of the LP incident wave can be oriented either along the x-axis (E_x component) or along the y-axis (E_y component). When the incident *E*-field has an x-directed component (E_x), we define R_{xx} = co-polarized reflection coefficient, R_{yx} = cross-polarized reflection coefficient, T_{xx} = co-polarized transmission coefficient and T_{yx} = cross-polarized transmission coefficient. Similarly, when the incident E-field has a y-directed component (E_y), the x and y subscripts are interchanged.

Initially, a metallic circular ring (inner radius R1 = 3.2 mm, width W1 = 1 mm and split gap S = 1.5 mm) is taken as the top unit cell and a 90^0 rotated version as the bottom unit cell. The unit cell periodicity is L-cell = 12 mm. The ring is designed to have a circumference ≈ λ_g at 6GHz ($\lambda_g = \lambda_0$/sqrt(ε_r)). After simulation, it is found that the MS has a Co-T band for both E_x and E_y incidence (T_{xx} and T_{yy} > 0.8) centered around 3.8GHz (≈ 6GHz/1.5) and a CPC transmission band for E_x incidence (T_{yx} > 0.8) around 11.2GHz (≈ 3 × 3.8GHz). The shift in resonance frequency (from 6GHz to 3.8GHz) is due to the additional capacitance of the split gap, the capacitance between the top and bottom unit cells and between the adjacent unit cells. At the first operational band (3.8GHz), the circumference of the circular ring is $\approx 1.5\lambda'_g$ (λ'_g = guided wavelength at 3.8GHz). Two rectangular metallic strips of length L = 4 mm and width W1 are then added at the two ends of the split gap. This increases the effective perimeter of the circular ring and hence both the Co-T and CPC bands shift to the left. The modified circular ring now resembles the Greek letter omega, Ω. Finally, with the aim of increasing the number of operational bands, a semicircular arc of inner radius R2 and width W2 is capacitively coupled to this omega shaped structure. This is the final unit cell structure and is shown in Fig. 7.1(a) - (c) with R1 = 3.2 mm, W1 = 1 mm, R2 = 4.5 mm, W2 = 0.5 mm, L-arc = 5π mm, L = 4 mm, S = 1.5 mm, L-cell = 12 mm. Each unit cell therefore consists of an omega shaped metallic structure coupled electromagnetically to a semicircular metallic arc. The metallic patterns on the bottom surface are 90^0 rotated versions of the top metallic patterns. The resulting CMS lacks C4 symmetry. It also has more than one layer. Therefore, it can exhibit AT for LP waves.

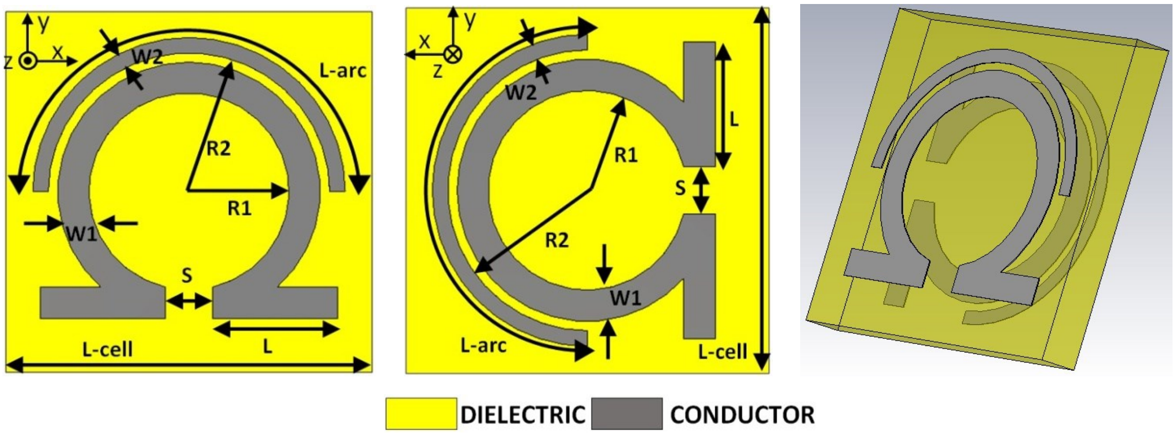

(a) (b) (c)

Fig. 7.1. Unit cell (a) top view, (b) bottom view and (c) 3D view.

The reflection and transmission coefficients of the MS for both orientations of the *E*-field (E_x and E_y) are presented in Fig. 7.2 for a forward wave. By observing Fig. 7.2(a), it can be seen that for E_x incidence the MS provides 1 Co-T band ($T_{xx} > 0.8$) around 3.3GHz and 2 CPC transmission bands ($T_{yx} > 0.8$) around 9.8GHz and 11.5GHz respectively. Similarly, by observing Fig. 7.2(b), it can be seen that for E_y incidence the MS provides 1 Co-T band ($T_{yy} > 0.8$) around 3.3GHz and 3 CPC transmission bands ($T_{xy} > 0.8$) around 5.7GHz, 6.3GHz and 12.8GHz respectively. Interestingly, there is another band near 4.1GHz in Fig. 7.2(b) where the incident LP wave is converted to a CP wave. This LTC polarization conversion band will be studied in the later sections. The 5 CPC transmission bands and the LTC transmission band of the MS are asymmetric in nature. However, the Co-T band is symmetric in nature. Figure 7.3 sheds light on the different operations of the MS. The handedness of the

CP wave in the LTC band is defined with respect to the propagation direction. At 4.1GHz for E_y incidence on Side 1 (forward wave incidence), the transmitted wave is RHCP with respect to the direction of propagation of the forward wave. Similarly, at 4.1GHz for E_x incidence on Side 2 (backward wave incidence), the transmitted wave is RHCP with respect to the direction of propagation of the backward wave.

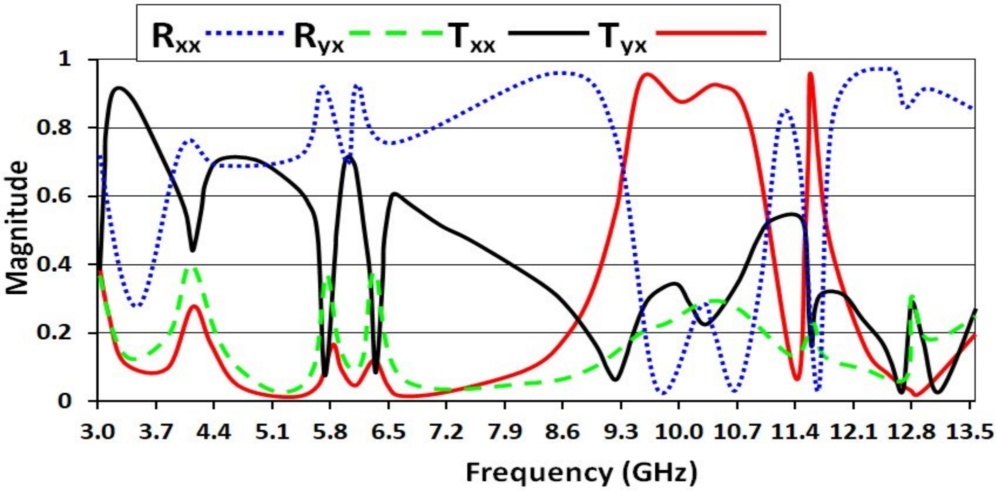

(a)

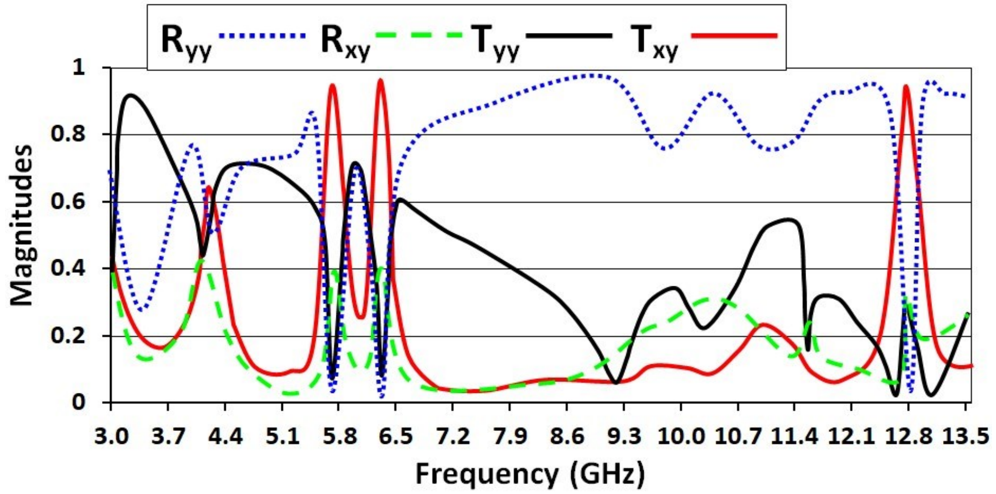

(b)

Fig. 7.2. Simulated co– and cross-polarized reflection and transmission parameters for a –z directed LP incident plane wave (forward wave) having (a) E_x component and (b) E_y component.

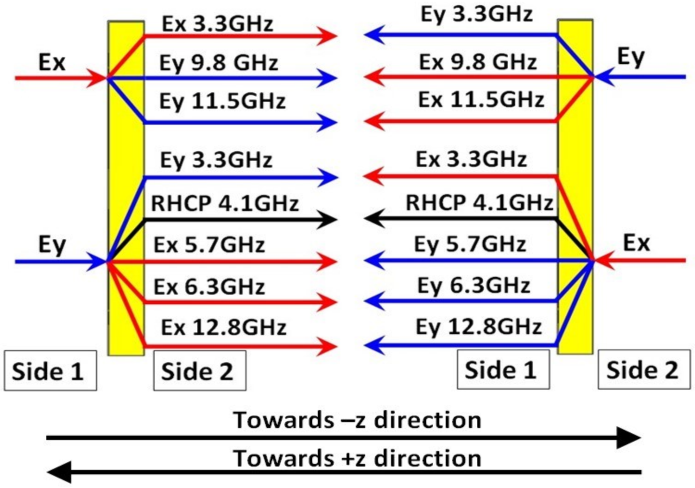

(a) (b)

Fig. 7.3. Transmission bands of the MS when (a) –z directed LP plane wave (forward wave) is incident on the top surface (Side 1) and (b) + z directed LP plane wave (backward wave) is incident on bottom surface (Side 2).

The plot of the AT parameter is presented in Fig. 7.4. It can be seen that the asymmetric parameter is close to 0.8 around 5.7GHz, 6.3GHz, 9.8GHz, 11.5GHz as well as 12.8GHz. Therefore the MS achieves a high degree of asymmetry within these CPC transmission bands.

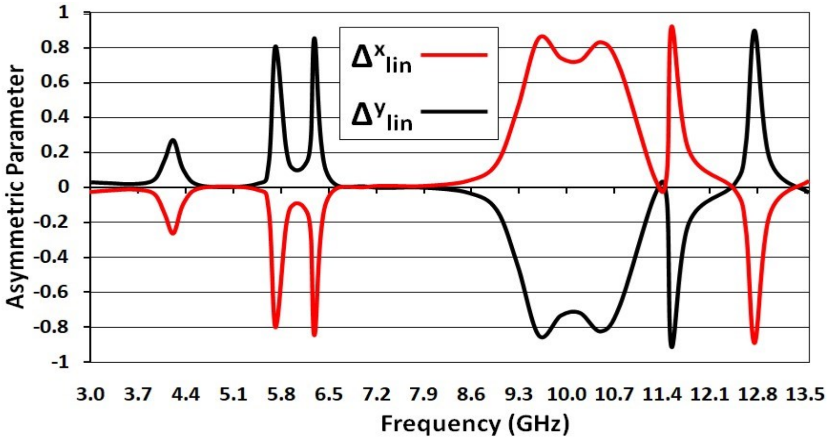

Fig. 7.4. Simulated asymmetric transmission parameter Δ_{lin}^{i} for the CMS.

In [1], authors present a continuous omega-shaped metasurface. However, there are several key differences between [1] and this work. Firstly, the unit cells of the top and bottom in [1] are continuous and there is no separation between adjacent unit cells. Secondly, although the unit cells have been termed omega-shaped, they resemble a square wave pulse and the MS looks like a train of square wave pulses. Thirdly, there are no metallic strips capacitively coupled to the unit cells. Finally, the resulting MS of [1] exhibits a single CPC AT band whereas the proposed MS exhibits 5 CPC AT bands, 1 LTC AT band and 1 Co-T band.

7.2.1 Effects of adding the semicircular metallic arcs

The best way to understand the impact of adding the semicircular arcs is to plot the transmission parameters of the CMS with and without the arcs. This has been done in Fig. 7.5. It can be observed from Fig. 7.5(a) that for an incident wave having E_x component, the arcs give rise to the CPC band at 11.5GHz. Similarly, from Fig. 7.5(b), it can be noted that for an incident wave having E_y component, the arcs give rise to the CPC bands at 5.7GHz, 6.3GHz and 12.8GHz. Therefore, the addition of the semicircular metallic arcs to the unit cells increases the number of CPC bands for both x- and y-directed incident E-fields.

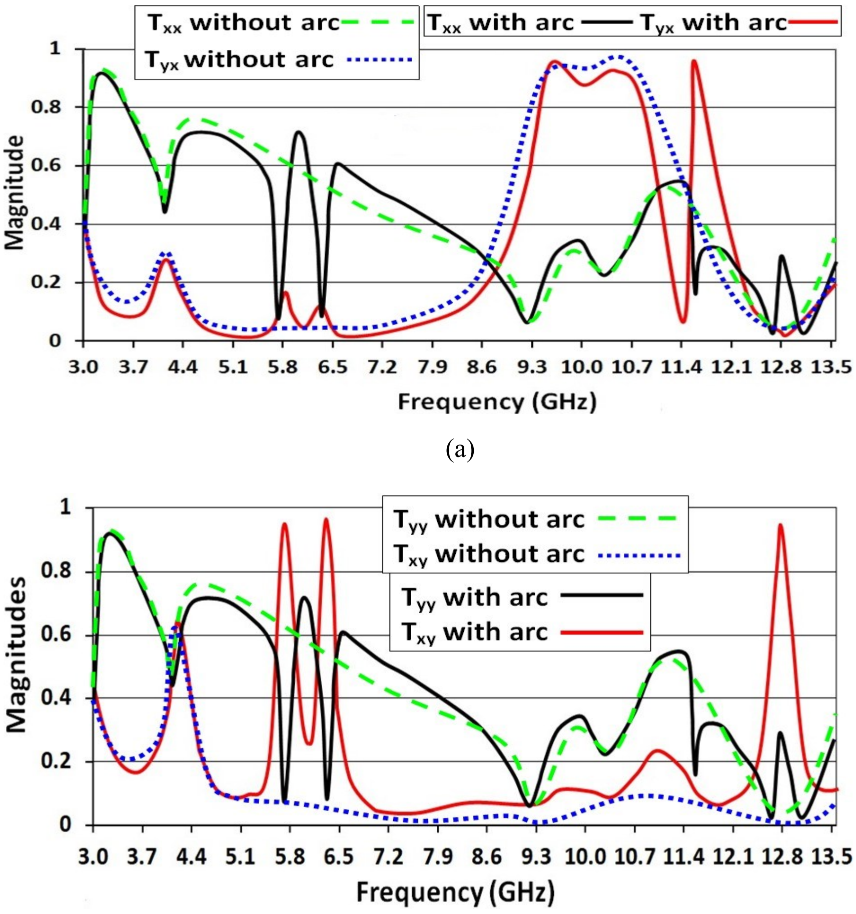

(a)

(b)

Fig. 7.5. Transmission parameters with and without the semicircular arcs for incident LP plane wave (forward wave) having (a) E_x component and (b) E_y component.

7.2.2 Co-T bands

It is observed from Fig. 7.2 that there is a Co-T band around 3.3GHz for both E_x and E_y orientations of the incident *E*-field. For the transmission band to exist for both x- and y-directed *E*-fields, the unit cells of the MS must appear the same to both E_x as well as E_y. This can happen when most of the induced currents circulate along the inner circular ring-like structures on the top and bottom unit cells and there is only a small portion of current on the semicircular arcs and rectangular portions (length L). In such a case, both the incident E_x and E_y will see two stacked conducting circular ring-like structures from both Side1 and Side 2. To understand why the transmission band is co-polarized, the induced current distributions need to be observed. When both the top and bottom conducting rings produce co-directional circulating currents, the induced *H*-fields will have only a z-component. Hence, there will be no component of the induced *H*-field parallel to the induced *E*-field (either E_x or E_y). Therefore, no cross-polarization conversion will take place.

7.2.3 Linear to circular polarization conversion band

For E_y incidence on Side 1, there is a range of frequencies around 4.1GHz where the incident LP wave is converted to a CP wave upon transmission. In order for this to happen, the magnitudes of the two transmitted components T_{xy} and T_{yy} have to be nearly the same and the phase difference between these components have to be an odd multiple of π/2. The axial ratio (AR) of such a transmission band can be calculated as follows

$$\mathrm{AR} = \frac{1}{2}\left[\frac{\left|T_{\mathrm{yy}}\right|^2 + \left|T_{\mathrm{xy}}\right|^2 + \left(\left|T_{\mathrm{yy}}\right|^4 + \left|T_{\mathrm{xy}}\right|^4 + 2\left|T_{\mathrm{yy}}\right|^2\left|T_{\mathrm{xy}}\right|^2\cos(2\Delta\varphi)\right)^{\frac{1}{2}}}{\left|T_{\mathrm{yy}}\right|^2 + \left|T_{\mathrm{xy}}\right|^2 - \left(\left|T_{\mathrm{yy}}\right|^4 + \left|T_{\mathrm{xy}}\right|^4 + 2\left|T_{\mathrm{yy}}\right|^2\left|T_{\mathrm{xy}}\right|^2\cos(2\Delta\varphi)\right)^{\frac{1}{2}}}\right]^{\frac{1}{2}}. \tag{7.1}$$

In the above equation, $\Delta\varphi$ is the phase difference between T_{yy} and T_{xy}. The AR can then be calculated in dB. Equation 7.1 can also be used when the incident wave has an E_x component simply by replacing T_{yy} by T_{xx} and T_{xy} by T_{yx}. To determine the handedness of the transmitted CP wave, i.e., right-hand CP (RHCP) or left-hand CP (LHCP), Stokes parameters (S_0, S_1, S_2 and S_3) are used. The ratio of S_3/S_0 can be used to identify the handedness of the CP wave. For a pure RHCP wave, S_3/S_0 = +1 and for a pure LHCP wave, S_3/S_0 = -1. S_0 and S_3 are defined (for an incident wave having E_y component) as follows:

$$S_0 = |T_{yy}|^2 + |T_{xy}|^2 \text{ and } S_3 = 2|T_{yy}||T_{xy}|\sin\Delta\varphi \,. \tag{7.2}$$

7.2.4 Induced surface currents

The currents induced on the top and bottom metallic patterns of the unit cells at the centre frequencies of the operational bands are presented in Fig. 7.6. The induced currents at 3.3GHz for E_x or E_y incidence on Side 1 is shown in Fig. 7.6(a). As discussed in the previous subsection, there are co-directional circulating currents concentrated along the top and bottom inner circular rings. The induced currents at 4.1GHz are similar to the induced currents at 3.3GHz but are oppositely directed in the top and bottom layers. The induced currents at 5.7GHz and 6.3GHz for E_y incidence on Side 1 are shown in Figs. 7.6(c) and (d) respectively. Within these bands, most of the currents are concentrated along the semicircular arcs and a small amount of current is present along the circumferences of the inner circular rings.

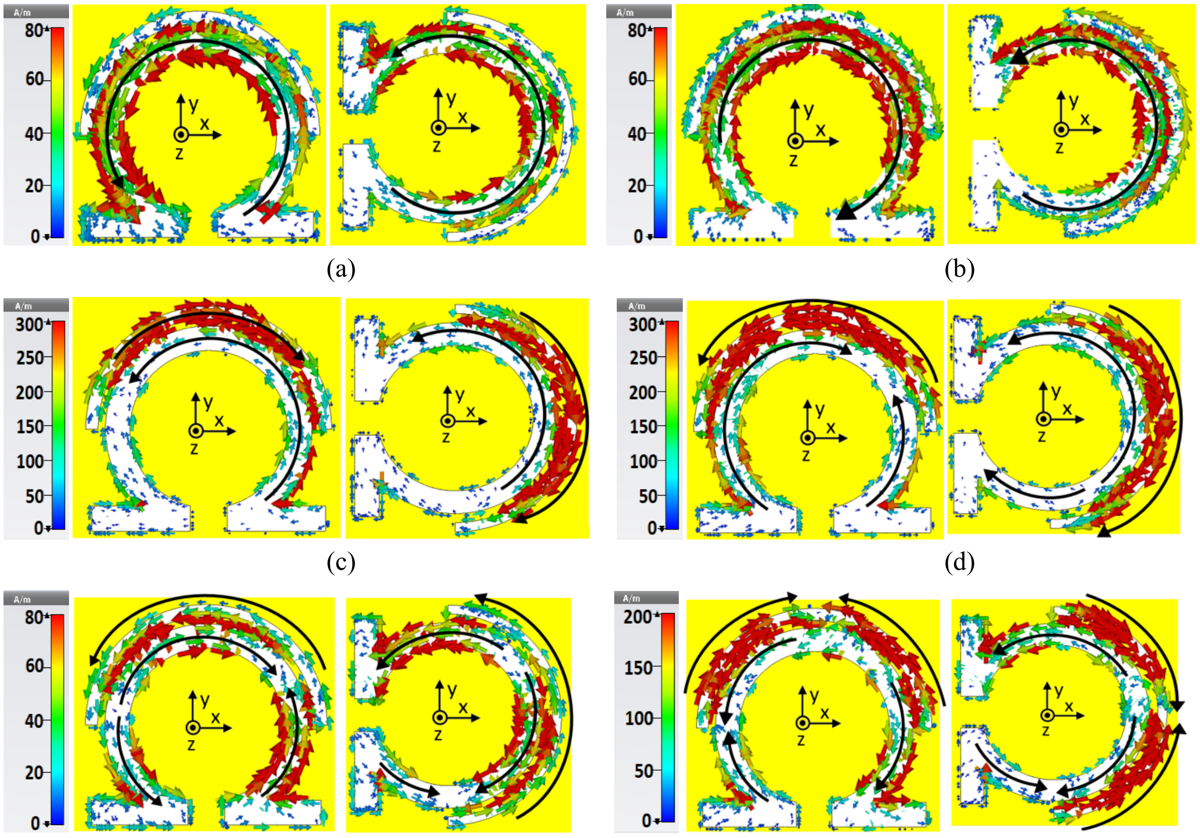

(a) (b)

(c) (d)

(e) (f)

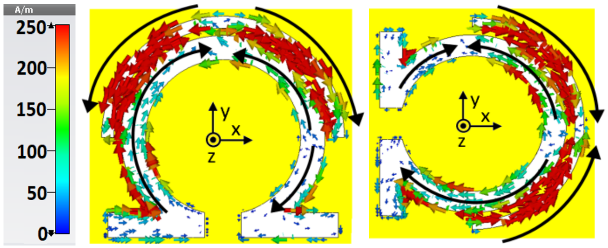

(g)

Fig. 7.6. Simulated surface currents (A/m) of top and bottom layers for normal incidence of a forward EM wave at (a) 3.3GHz (for E_x and E_y incidence), (b) 4.1GHz (for E_y incidence), (c) 5.7GHz (for E_y incidence), (d) 6.3GHz (for E_y incidence), (e) 9.8GHz (for E_x incidence), (f) 11.5GHz (for E_x incidence) and (g) 12.8GHz (for E_y incidence).

The induced currents on the top and bottom semicircular arcs are co-directional at 5.7GHz and oppositely directed at 6.3GHz. Figure 7.6(e) illustrates the induced currents at 9.8GHz for E_x incidence on Side 1. It can be seen that most of the currents are concentrated along the inner circular rings and only a small portion is present along the semicircular arcs. The currents on the inner circular rings now have an additional null with respect to the distribution of Fig. 7.6(d), thereby implying that a higher order mode is now being supported by the rings. The induced current distributions at 11.5GHz for E_x incidence on Side 1 and at 12.8GHz for E_y incidence on Side 1 are illustrated in Fig. 7.6(f) and Fig. 7.6(g) respectively. At both these frequencies, most of the currents are concentrated along the semicircular arcs and a small portion is present along the circumferences of the inner rings. The currents along the semicircular arcs have an additional null, implying that a higher order mode is supported by the semicircular arcs. The nature of the currents induced on the inner circular rings at both frequencies is the same as that of Fig. 7.6(e). The only difference between Fig. 7.6(f) and Fig. 7.6(g) is the orientation of the currents on the top and bottom layers. At any instance of time, the currents on the top and bottom semicircular arcs at 11.5GHz converge towards/diverge away from the arc length centers together. However, at 12.8GHz, when the currents on the top semicircular arc converge towards the arc length center, the currents on the bottom arc diverge away from the arc length center and vice-versa. By observing the induced surface currents, the importance of the semicircular arcs becomes evident. Large portions of the induced currents are present on these arcs at 5.7GHz, 6.3GHz, 11.5GHz as well as 12.8GHz. Hence, without the arcs, these bands cannot exist.

7.2.5 Band tuning and performance optimization

The proposed CMS has 7 operational bands and there are 8 parameters of the unit cell which can be tuned. These are R1, W1, R2, W2, S, L, L-arc and L-cell. Since the CPC bands centered about 5.7GHz, 6.3GHz, 11.5GHz and 12.8GHz are dependent on the semicircular arc; these bands can be tuned by varying R2, W2 and L-arc. On the other hand, the Co-T band centered around 3.3GHz, the LTC band centered around 4.1GHz and the CPC band centered around 9.8GHz are mainly dependent on the inner circular ring-shaped structure. These bands can be tuned efficiently by varying R1, W1 and S. The rectangular portions of the unit cell (length ‘L’; Fig. 7.1) and the unit cell periodicity (L-cell) are used to fine tune the response of the MS. By adjusting the length L and periodicity L-cell, the transmission peaks of the bands can be adjusted and improved. The responses of the MS for varying L-cell are shown in Fig. 7.7 to demonstrate the above point. After adjusting the 8 aforementioned parameters, the optimized values of the parameters are chosen (values presented at the beginning of Sec. 7.2) to reflect the best performance of the MS within the chosen frequency range of 3–13.5GHz. All the 7 operation bands can also be shifted up or down by scaling the 8 unit cell parameters. For instance, if all the unit cell parameters are multiplied by 1.5, the resulting operation bands will also shift down in frequency by a factor of about 1.5.

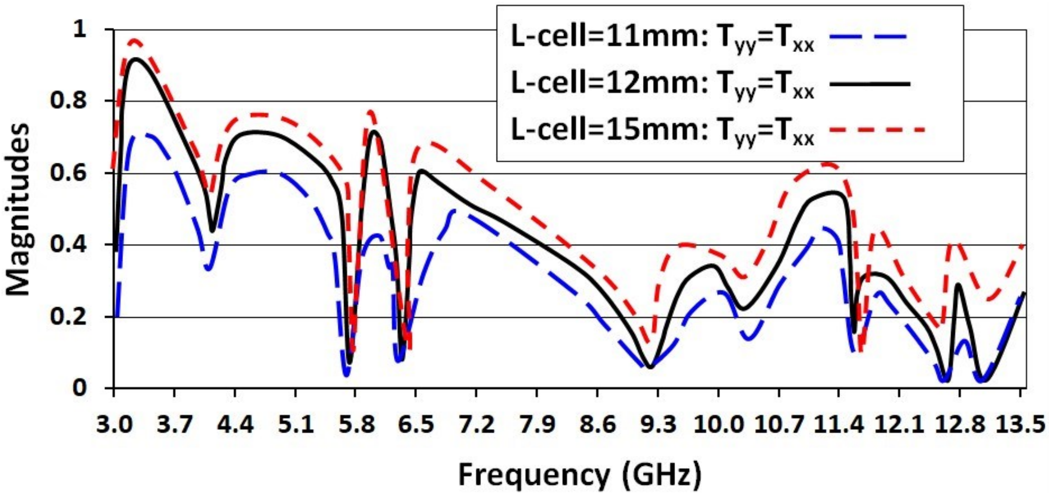

(a)

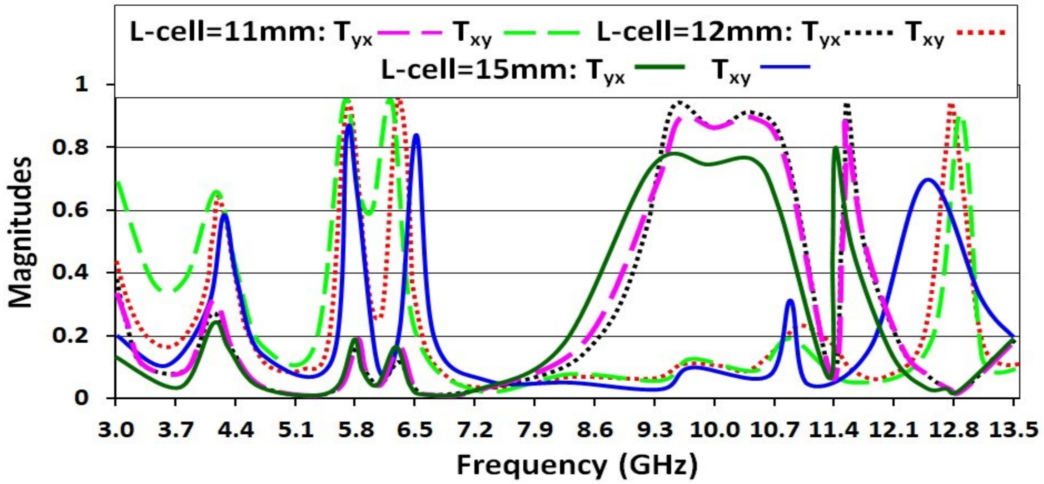

(b)

Fig. **7.7.** Effects of varying L-cell on (a) co– and (b) cross-polarized transmission coefficients.

7.3 Experimental Verification

In order to experimentally verify the simulation results, a prototype of the MS is fabricated with 12 × 12 unit cells (144 mm × 144 mm) as shown in Fig. 7.8(a). The transmission coefficients are measured inside an anechoic chamber by using two identical dual-ridge wideband horn antennas. The Port extension feature of the VNA is used to measure the The MS is placed in the far-field region of both antennas to ensure plane wave incidence. The measurement configurations are shown in Fig. 7.8(b) and (c). The co- and cross- polarized transmission coefficient measurement setups are also shown in Fig. 7.8(d).

The first set of measurements (both co- and cross) are performed with only the two horn antennas and antenna stands. This is to measure the transmission phase and magnitudes in free space within the anechoic chamber.

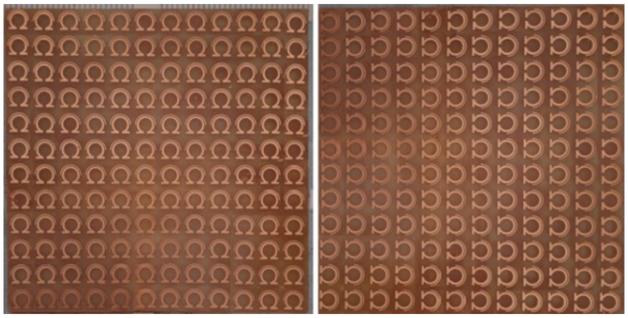

(a)

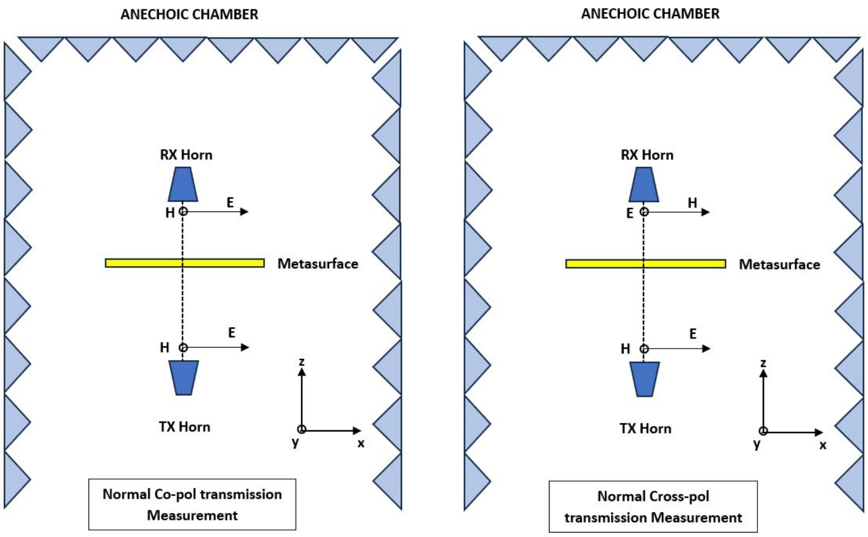

(b)

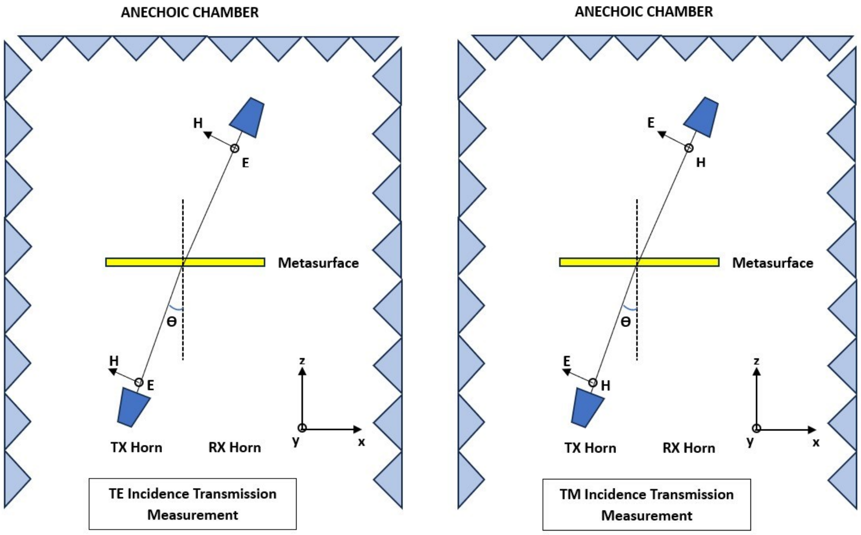

(c)

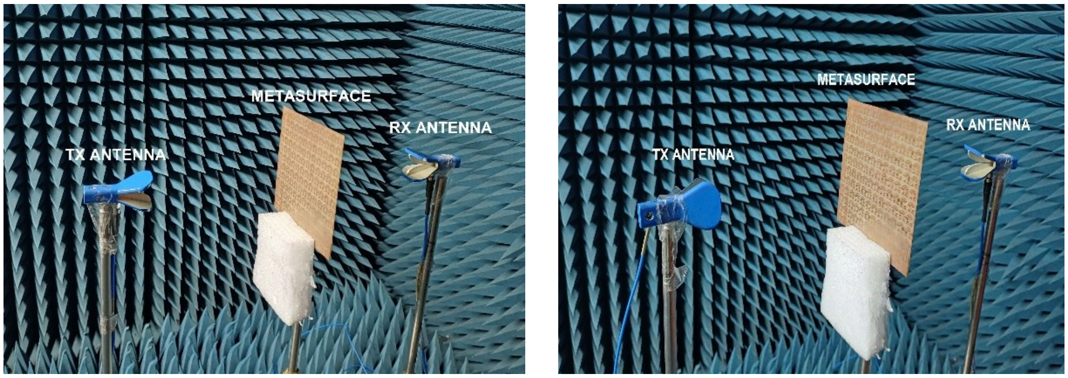

(d)

Fig. 7.8 (a) Fabricated MS with 144 unit cells. Measurement configurations (b) for normal incidence and (c) TE, TM incidence. (d) Measurement setup for co- (left) and cross- (right) polarization measurements.

Then, the metasurface is placed in between and the two horn antennas and the co- as well as cross-polarization coefficients are measured again using the S_{21} of the VNA. The S_{21} magnitudes of the second set of measurements are normalized with respect to the S_{21} magnitudes of the first set of measurements. Similarly, the S_{21} phases of the second set of measurements within the LTC band frequencies are references with respect to the S_{21} phases of the first set of measurements within the LTC band. The magnitudes and phases of the S_{21} are then used to find the Axial ratio as presented in (7.1). The measured magnitudes and phases of T_{xy} and T_{yy} used to calculated the AR for normal incidence is provided below in Fig. 7.9.

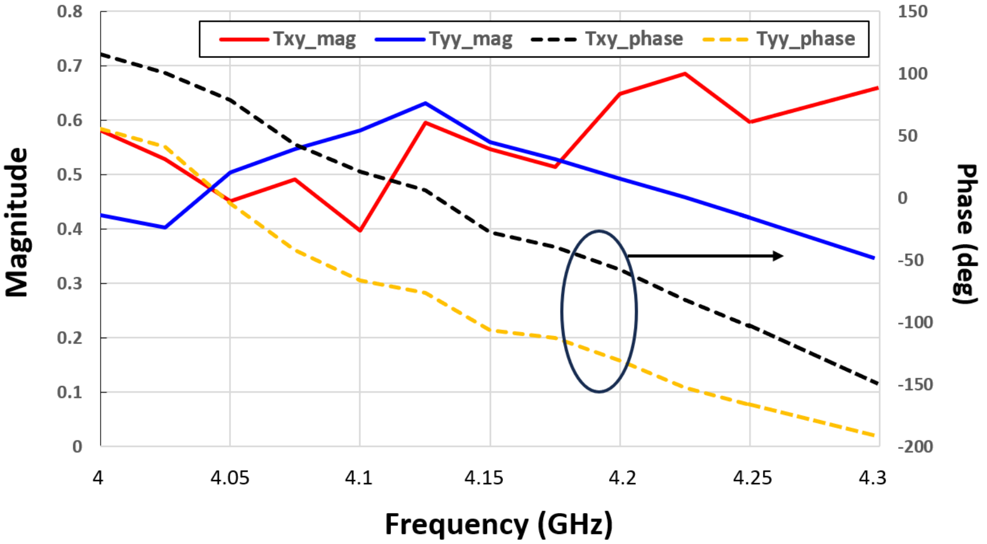

Fig.7. 9. Measured co- and cross- polarized magnitudes and phases within the LTC band.

7.3.1 Co-T band

The co-polarized transmission (Co-T) band of the MS exists from 3.05GHz to 3.5GHz for normal incidence (bandwidth calculated for range of frequencies where T_{yy} or $T_{xx} > 0.8$). The maximum measured magnitudes of T_{yy} and T_{xx} within this band are 0.91 and 0.92 respectively (at normal incidence). On observing Fig. 7.10, it is found that the Co-T band gives good response for incident angles up to 60^0 for both TE and TM incidence.

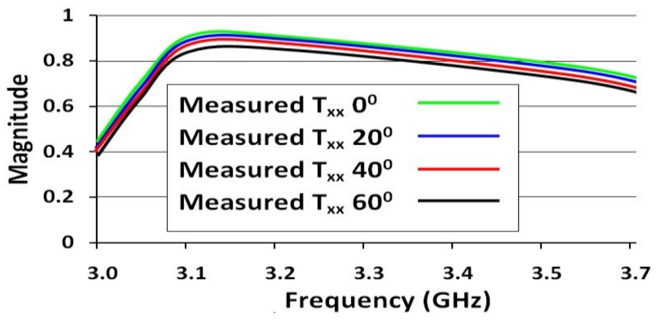

(a)

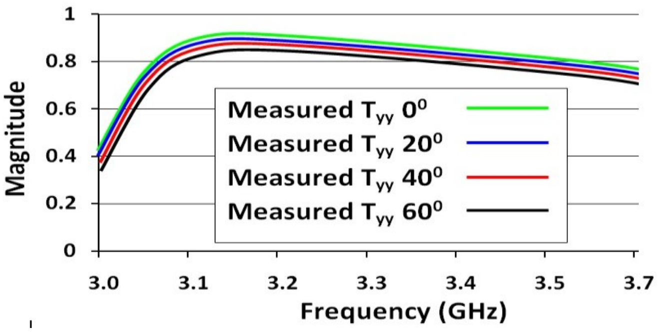

(b)

Fig.7. 10. Angular stability of the Co-T band for (a) TM and (b) TE incidence.

7.3.2 LTC band

The AR of the LTC band is calculated using (7.1). Under normal incidence, the AR of the LTC band remains below 3dB from 4.05GHz to 4.23GHz. The handedness of the transmitted wave is calculated using (7.2). The The simulated and measured plots of the AR and S_3/S_0 for different incident angles are presented in Fig. 7.11. The LTC band shows good response for incident angles up to 60^0 for TE incidence of a plane wave on Side 1. The S_3/S_0 plot is close to +1 within the LTC band which denotes that the transmitted wave is an RHCP wave (RHCP with respect to the direction of propagation of the wave).

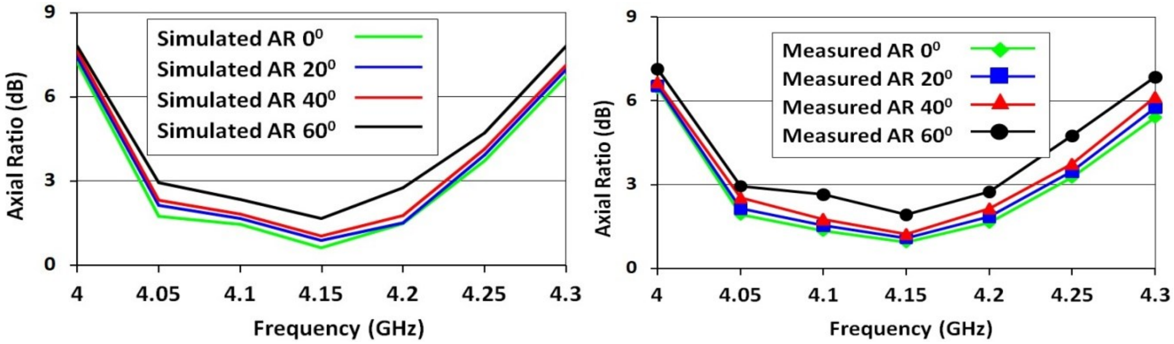

(a)

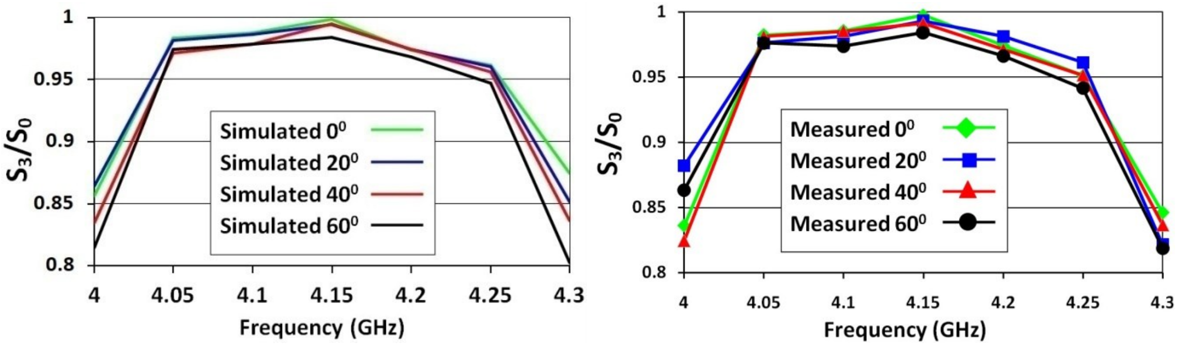

(b)

Fig. 7.11 (a), (b) The AR and (c), (d) S_3/S_0 ratios of the proposed MS for TE incidence within the LTC band.

7.3.3 Polarization conversion ratio (PCR)

The polarization conversion ratio (PCR) is a measure of how efficiently a structure converts the polarization of the incident wave. The PCR is the ratio of the power transmitted in the cross-polarized component to the total transmitted power. It is given mathematically as

$$\mathrm{PCR} = \frac{\left|T_{yx}\right|^2}{\left|T_{yx}\right|^2 + \left|T_{xx}\right|^2} \text{ or } \frac{\left|T_{xy}\right|^2}{\left|T_{xy}\right|^2 + \left|T_{yy}\right|^2}. \tag{7.3}$$

The simulated and measured PCRs for incident *E*-field along y-direction (Fig. 7.12(a)) and for incident *E*-field along x-direction (Fig. 7.12(b)) show that there are in fact 5 CPC bands (where PCR > 0.8). They lie within 5.65–5.76GHz, 6.24–6.35 GHz, 8.9–10.7GHz, 11.42–11.57GHz and 12.43–13.25GHz. The maximum measured cross–polarized wave transmission coefficients (T_{xy} or T_{yx}) are found to be 0.9, 0.91, 0.93, 0.92 and 0.91 within the 5.7GHz, 6.3GHz, 9.8GHz, 11.5GHz and 12.8GHz bands respectively (for normal incidence). Therefore, the MS achieves efficient transmission in all the CPC bands. The measured angular stabilities of the PCRs are shown in Fig. 7.13. It should be noted that the range of frequencies within which the angular stability is up to 60^0 is from 3GHz to 11.5GHz. Above 11.5GHz, the unit cell size becomes ≈ $0.46\lambda_0$ (where λ_0 = free space wavelength at 11.5GHz). Since the angular stability usually degrades with increasing cell size, the angular stability of the MS decreases above 11.5GHz. The 11.5GHz and 12.8GHz CPC bands have relatively less angular stability (up to 30^0). The measured results are close to the simulated results.

There are some slight discrepancies between the simulated and measured results which can be attributed to fabrication tolerances and the finite nature of the fabricated metasurface.

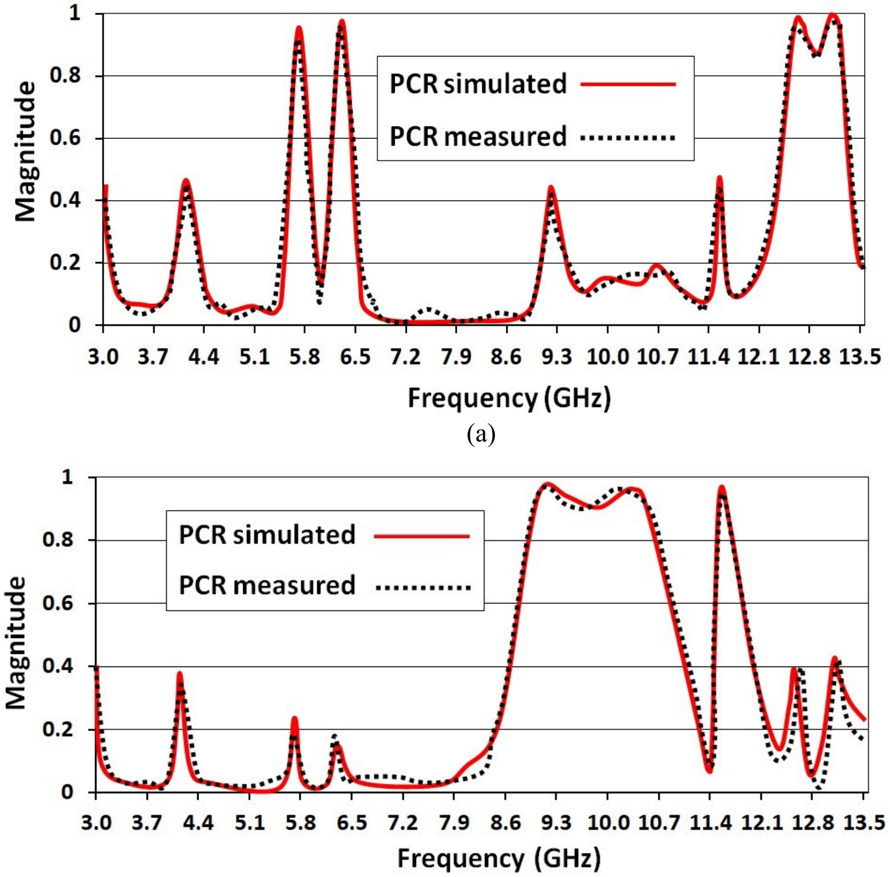

(a)

(b)

Fig. 7.12. Simulated and measured PCR for (a) E_y incident on Side 1 and (b) E_x incident on Side 1.

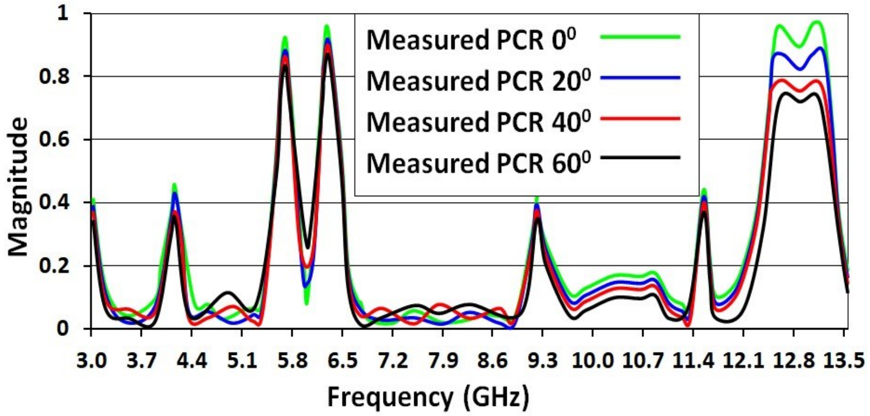

(a)

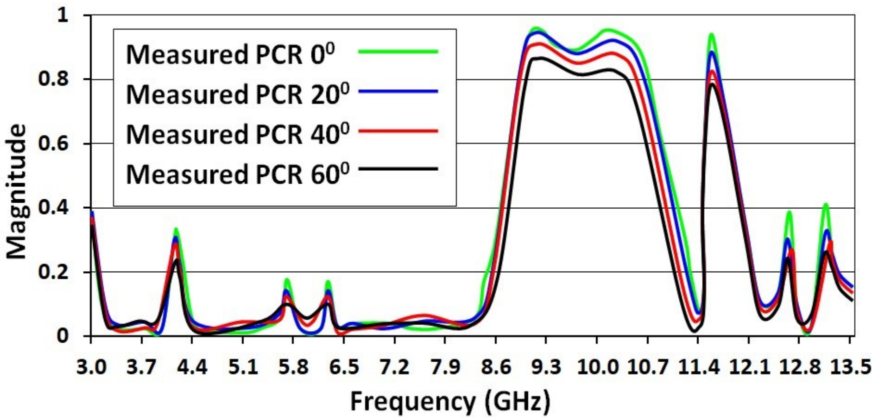

(b)

Fig. 7.13 Measured PCR for (a) TE incidence and (b) TM incidence on Side 1.

7.4 Comparisons with similar structures and advantages of the proposed MS

The proposed MS is compared with similar works found in literature in Table 7.1. The proposed MS has more CPC bands (5 in total) than any other MS presented in literature. Additionally, it also has a symmetric Co-T band as well as an asymmetric LTC band which make it more versatile. The structure has good angular stability and is ultrathin. The electrical thickness of the MS is $\lambda_0/35$ at the 1st asymmetric CPC transmission band, $\lambda_0/48.7$ at the asymmetric LTC transmission band and $\lambda_0/64.7$ at the 1st Co-T band. Having multiple bands allows the proposed MS to be useful across different microwave bands. The MS can perform propagation direction dependent CPC transmission in the C, X and Ku bands. The asymmetric CPC transmission band within the X band is relatively wideband with a bandwidth of 18.36% (8.9–10.7GHz). The MS can act as a direction of propagation independent spatial co-polarized pass-band filter in the S band and as a direction of propagation dependent linear to circular polarization converter within the C band. The proposed MS can therefore perform different functions within the different microwave bands. This gives it an advantage over previous MSs found in literature. The operational frequency bands of the MS can also be tuned and shifted up or down to fit user-defined specifications. The highest operational band within the 60^0 angular stability region (3–11.5GHz) is the CPC band centered at 9.8GHz. The unit cell size at 9.8 GHz with respect to the free space operating wavelength at 9.8GHz is $0.37\lambda_0$. The MS in [2], which also has an angular stability up to 60^0, has a similar unit cell size of $0.35\lambda_0$ at its centre operating frequency.

Table 7.1. Comparisons with similar structures found in literature.

Ref.	Co-T bands (GHz)	CPC bands (GHz)	LTC bands (GHz)	Thickness	Angular Stability
[2]	None	1 (10.1#)	None	$\lambda_0/38$	60^0
[3]	None	1 (13.87-16.04)	None	$\lambda_0/27$	60^0
[4]	None	2 (3.241-3.243, 3.675-3.677)	None	$\lambda_0/10.2$	0
[5]	None	2 (7.6-7.7, 9.15-9.25)	None	$\lambda_0/13$	0
[6]	None	3 (9.1#, 13.9#, 19.1#)	None	$\lambda_0/15$	0
[7]	None	3 (10.9-11.2, 14.4-14.8, 18.4-18.5)	None	$\lambda_0/20.4$	40^0 (within first 2 bands)
This work	1 (3.05-3.5)	5 (5.65-5.76, 6.24-6.35, 8.9-10.7, 11.42-11.57, 12.43-13.25)	1 (4.05-4.23)	$\lambda_0/64.7$ (3.05GHz) $\lambda_0/48.7$ (4.05GHz) $\lambda_0/35$ (5.65GHz)	60^0 (3-11.5GHz) 60^0 (above 11.5GHz)

Bandwidth values not provided explicitly.

7.5 Conclusions

A planar CMS is proposed with two layers of omega-shaped unit cells placed on opposite sides of a microwave substrate. The unit cells on the bottom are rotated 90^0 with respect to the unit cells on the top. To achieve multiple transmission bands, a semicircular metallic arc is electromagnetically coupled to each omega-shaped unit cell. The final structure exhibits one symmetric co-polarized transmission (Co-T) band, one asymmetric linear-to-circular (LTC) polarization conversion transmission band as well as five asymmetric cross-polarization conversion (CPC) transmission bands (cross-polarization conversion of LP incident plane waves). The MS is ultrathin and has a thickness of $\lambda_0/64.7$ which makes it very lightweight. It also operates favorably for incident angles up to 60^0 for both transverse-electric (TE) and transverse-magnetic (TM) incidence within 3–11.5GHz. The operational bands can be tuned by varying the different parameters of the unit cell geometry to meet user requirements. The MS can also be used across many microwave frequency bands.

REFERENCES

[1] Y. H. Wang, R. C. Jin, J. Li, J. Q. Li, Z. G. Dong, "Enhanced asymmetric transmissions attributed to the cavity coupling hybrid resonance in a continuous omega-shaped metamaterial," *Opt. Express*, vol. 26, pp. 3508–3517, 2018.

[2] M. I. Khan *et al*., "Efficient asymmetric transmission for wide incidence angle using bi-layered chiral metasurface," *J. Phys. D Appl. Phys.*, vol. 53, no. 30, 305004, 2020.

[3] S. Aisha *et al*., "An efficient chiral polarization rotator with asymmetric transmission for large incidence angles," *Journal of App. Phys*., vol. 128, 213102, 2020.

[4] M. L. Li *et al*., "Microwave linear polarization rotator in a bilayered chiral metasurface based on strong asymmetric transmission," *J. Opt*., vol. 19, no. 7, 075101, 2017.

[5] S. Khan, T. F. Eibert, "A dual-band metasheet for asymmetric microwave transmission with polarization conversion," *IEEE Access*, vol. 7, pp. 98045–98052, 2019.

[6] D. Liu, Z. Xiao, Z. Wang, "Multi-band asymmetric transmission and 900 polarization rotator based on bi-layered metasurface with F-shaped structure," *Plasmonics*, vol. 12, pp. 445–452, 2017.

[7] M. I. Khan, B. Hu, Y. Chen, N. Ullah, M. J. I. Khan, A. R. Khalid, "Multiband efficient asymmetric transmission with polarization conversion using chiral metasurface," *IEEE Ant. Wirless Prop. Lttr.*, vol. 19, no. 7, pp. 1137–1141, 2020.

CHAPTER 8

A MULTIBAND META-MIRROR

8.1 Concept of a Meta-Mirror

When a CP wave is incident on a conventional mirror (e.g. a metallic reflector at low frequencies), the handedness of the reflected CP wave changes with respect to an observer who observes both the incident and reflected waves from the same position. In contrast, when a CP wave is incident on a meta-mirror, the handedness of the incident and reflected waves remain the same for the observer. The difference between a conventional mirror and a meta-mirror is illustrated in Fig. 8.1.

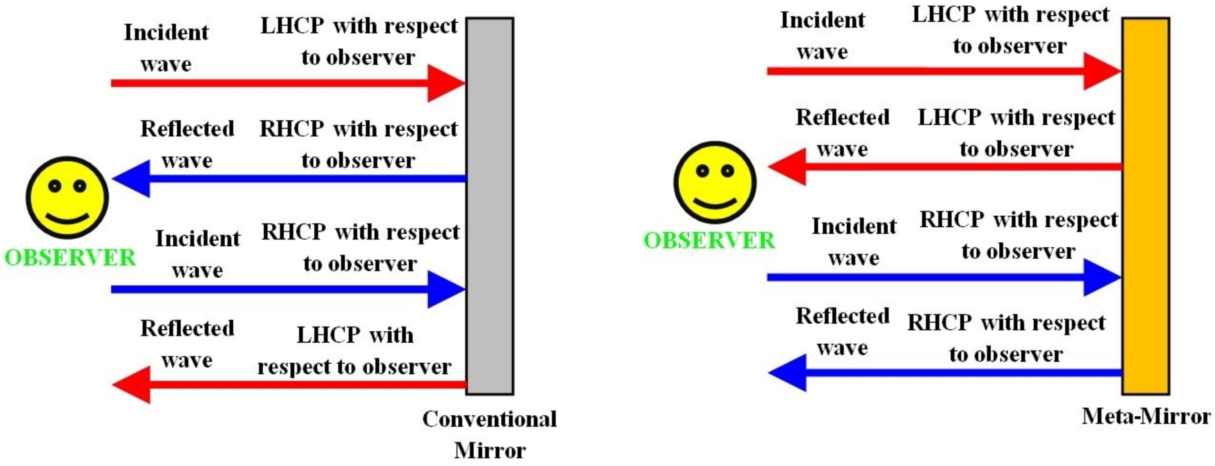

Fig. 8.1. Comparison between a conventional mirror and meta-mirror.

8.2 Objective

Although most of the Chiral MSs (CMSs) present in literature exhibit AT for LP incident waves, researchers have also studied the asymmetry phenomenon for CP incidence [1]–[6]. In fact, the very first paper on AT by Fedotov *et al*. [1] was based on the AT of CP waves. However, all of them exhibit broadband responses and none exhibit asymmetry in more than one frequency band. Moreover, all these papers work only with the asymmetric *transmission* of CP waves. In this chapter, we explore the phenomenon of asymmetric *reflection* of incident CP waves. It is found that an MS which can perform asymmetric reflection of CP waves can also act as a meta-mirror.

The main aim of this chapter is to design a bilayered ultrathin CMS, which can perform asymmetric reflection of incident CP waves within multiple frequency bands in the microwave region while also exhibiting good angular stability within these bands. Such an MS can be used as a multiband direction dependent meta-mirror. Multiple bands ensure that the structure can be integrated with different applications across different frequency bands. The effects of the different parts of the unit cell on the different operational bands are also studied with the aim of controlling the operational bands more efficiently.

8.3 Unit Cell design

In order to observe the asymmetric reflection property for incident CP waves, a bilayered CMS is designed which lacks C4 rotational symmetry. The top and bottom geometries of the CMS unit cell are 90^0 rotated versions of one another. The unit cell of the proposed CMS is shown in Fig. 8.2.

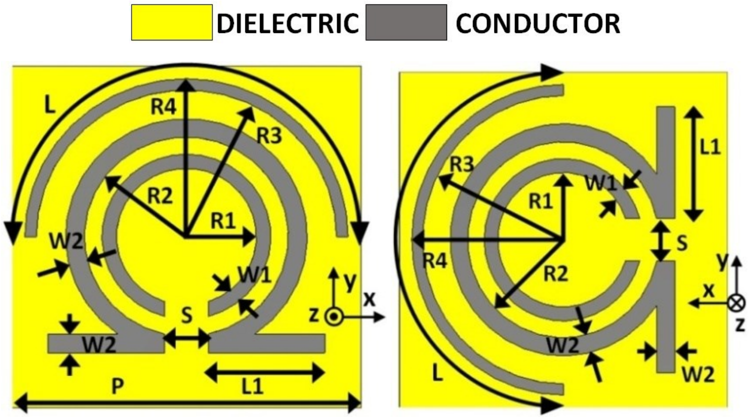

(a) (b)

Fig. 8.2 (a) Top and (b) bottom geometry of the CMS unit cell.

The microwave substrate used for the proposed MS is Arlon AD-430 with ε_r = 4.3, tanδ = 0.003 and thickness = 1.52mm. Copper is used to draw the metallic portions of the unit cells with $\sigma = 5.8 \times 10^7$ S/m. The unit cell design has been performed using CST Studio Suite with periodic boundary conditions (PBCs) set on all four sides. Each unit cell consists of an omega-shaped metallic structure coupled electromagnetically to an outer semicircular metallic strip and an inner circular metallic split ring. The dimensions are chosen as follows: R1 = 2.4mm, W1 = 0.5mm, R2 = 3.5mm, W2 = 0.65mm, R3 = 5.15mm, R4 = 5.55mm, L = 5.55πmm, L1 = 4mm, S = 1.5mm and P =12 mm. The unit cell parameters are optimized to provide the best performance within 5–6.5GHz and 9–12.5GHz. The tuning and scaling of the frequency bands are discussed in a later section.

8.4 CMS Properties

An EM wave which travels towards the –*z*-direction is considered to be the forward wave and an EM wave traveling towards the +*z*-direction is considered to be the backward wave. The handedness of a CP wave is again defined with respect to the direction of propagation of the wave. An incident RHCP wave is RHCP with respect to the incident wave propagation direction while a reflected RHCP wave is RHCP with respect to the propagation direction of the reflected wave.

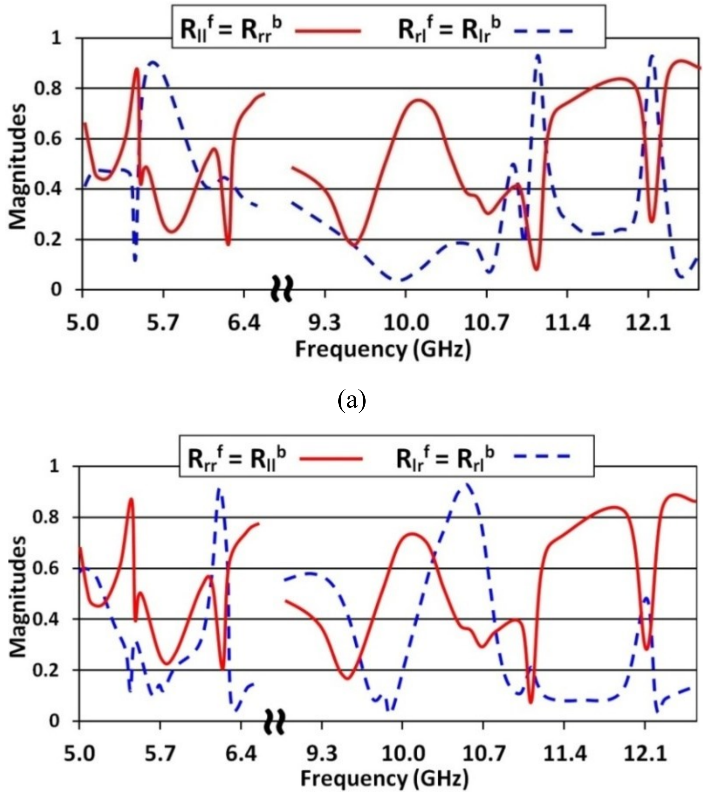

(a)

(b)

Fig. 8.3. Reflection coefficients of the CMS for (a) LHCP forward incidence (RHCP backward incidence) and (b) RHCP forward incidence (LHCP backward incidence).

The reflection coefficients of the proposed MS for RHCP and LHCP are shown in Fig. 8.3. When an incident wave is RHCP (LHCP) and the reflected wave is also RHCP (LHCP), the reflection coefficient is denoted by R_{rr} (R_{ll}). The other reflection and transmission coefficients can be easily deduced from the above statement.

It is observed from Fig. 8.3(a) that for the normal incidence of an LHCP forward wave (RHCP backward wave), there are three frequency bands where R_{rl}^{f} (R_{lr}^{b}) > 0.8. These frequency bands are 5.55–5.78GHz, 11.06–11.17GHz, and 12.03–12.18GHz. Similarly, it can be observed from Fig. 8.3(b) that for the normal incidence of an RHCP forward wave (LHCP backward wave), there are two frequency bands where R_{lr}^{f} (R_{rl}^{b}) > 0.8. These frequency bands are 6.1–6.23GHz and 10.42–10.68GHz. For an observer looking in the direction of the incident wave, the reflected wave will exhibit the same handedness as the incident wave (after reflection from the MS) within the five bands mentioned above. Hence, the MS can act as a meta-mirror within these bands. The asymmetry parameter Δ is calculated using

$$\Delta_{rx}^{l} = |R_{ll}^{f}|^2 + |R_{rl}^{f}|^2 - |R_{ll}^{b}|^2 - |R_{rl}^{b}|^2 = -\Delta_{rx}^{r} \tag{8.1}$$

where the superscript '*l*' and '*r*' are used to denoted LHCP and RHCP respectively while the subscript '*rx*' is used to denote reflection. There are five frequency bands where $|\Delta_{rx}| > 0.6$. These are also the five bands where the MS acts as a meta-mirror. This is demonstrated in Fig. 8.4.

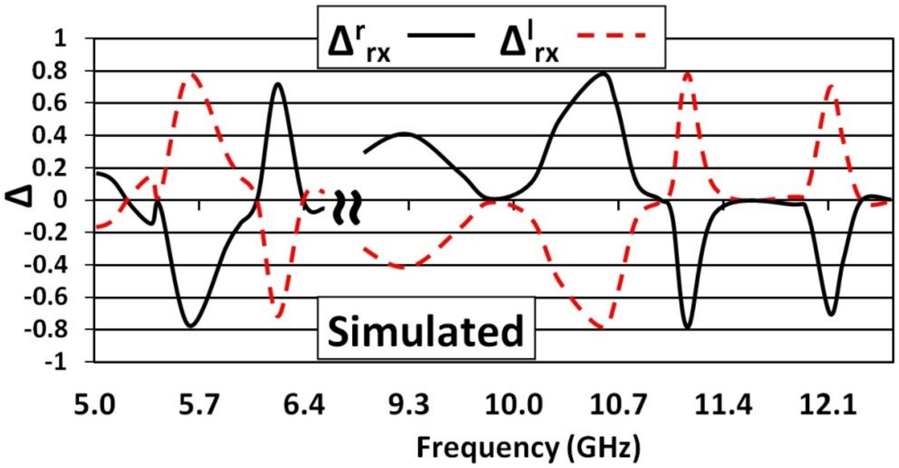

Fig. 8.4. Simulated asymmetry parameter of the proposed CMS.

8.4.1 Importance of the different parts of the Unit Cell

To understand the importance of the different parts of the unit cell, the evolution of the unit cell geometry is presented in Fig. 8.5(a) along with the Δ^r_{rx} plot for each configuration (Fig. 8.5(b)). "**A**" represents the unit cell with only the middle omega-shaped metallic pattern, "**B**" represents the unit cell with the semicircular metallic strip coupled to the omega-shaped metallic pattern, and "**C**" represents the proposed unit cell of Fig. 8.2.

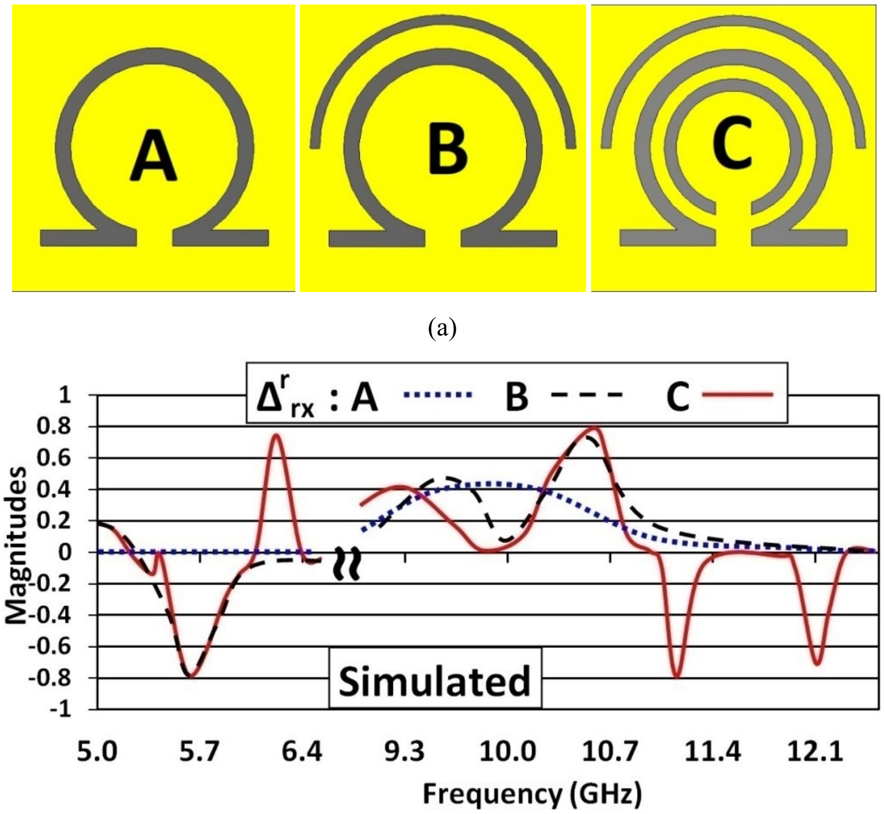

(a)

(b)

Fig. 8.5. (a) Evolution of the unit cell geometry and (b) asymmetry parameters for the three configurations of the unit cell.

It is observed that configuration A has no asymmetry bands within 5–6.5GHz while possessing a weak asymmetry ($\Delta^r_{rx} \approx 0.4$) within a portion of the 9–12.5GHz band. Configuration B has two significant asymmetry bands; one within 5–6.5GHz and the other within 9–12.5GHz. Therefore, the addition of the semicircular strips helps introduce two asymmetry bands. Finally, configuration C has three additional asymmetry bands; one within 5–6.5 GHz and two within 9–12.5GHz. It is the addition of the inner split ring that helps introduce these three additional asymmetry bands. Therefore, it is clear that the outer semicircular strip and inner split ring play an important role in increasing the number of asymmetry bands.

8.4.2 Induced Surface Current Distributions

The induced surface currents at the centre frequencies of each of the five operational bands are shown in Fig. 8.6.

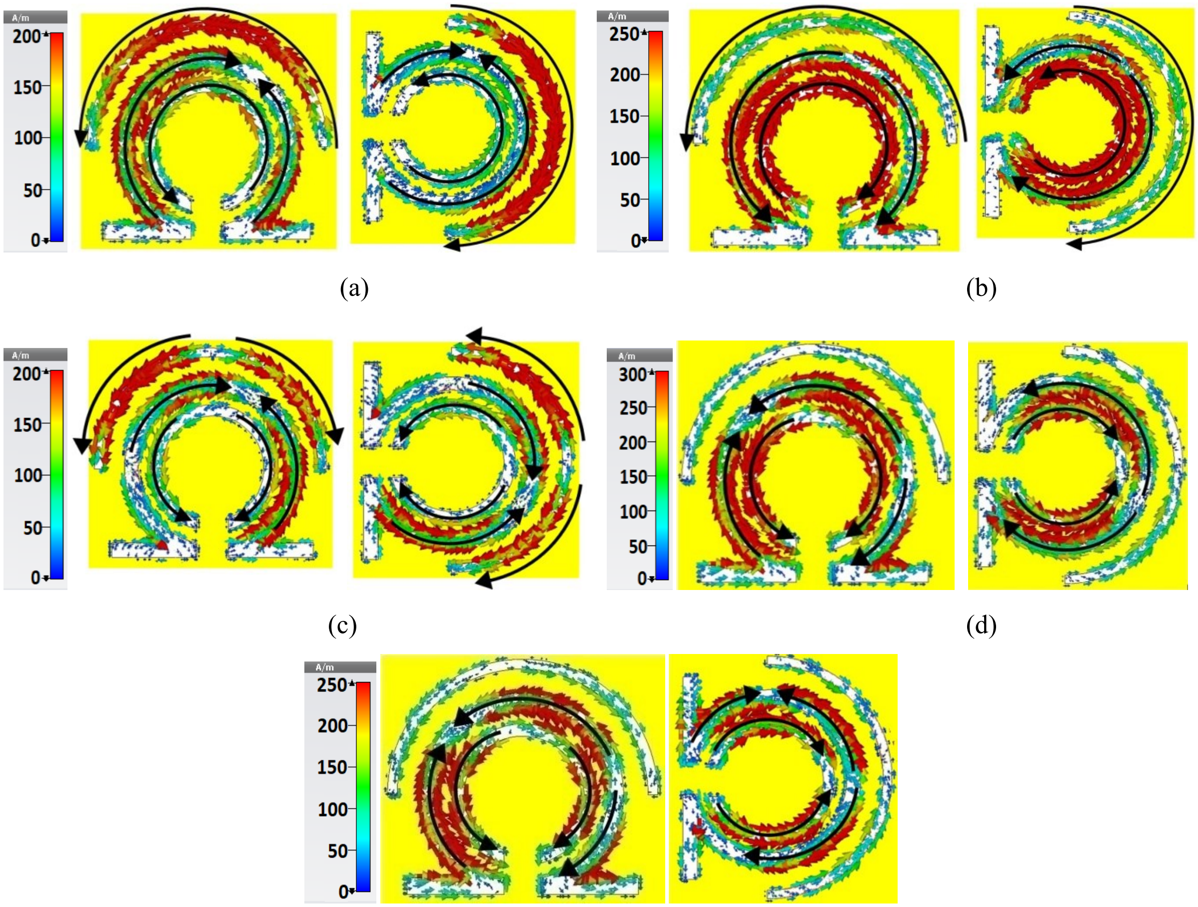

(a) (b)

(c) (d)

(e)

Fig. 8.6. Simulated surface current distributions (A/m) on the top and bottom layers for normal incidence of a forward EM wave at (a) 5.66GHz (for LHCP incidence), (b) 6.16GHz (for RHCP incidence), (c) 10.55GHz (for RHCP incidence), (d) 11.11GHz (for LHCP incidence) and (e) 12.1GHz (for LHCP incidence).

It is noted from Figs. 8.6(a) and (c) that a large portion of the induced currents are present on the semicircular strips at the center frequencies of the first band (5.55-5.78GHz) and third band (10.42-10.68GHz). At the center frequencies of the remaining three bands (6.1-

6.23GHz, 11.06-11.17GHz and 12.03-12.18GHz), the currents are mainly concentrated along the inner split ring and portions of the middle omega-shaped structure. This can be observed from Figs. 8.6(b), (d) and (e). Therefore, the first and third operational bands are influenced by the presence of the semicircular strips while the second, fourth and fifth bands are influenced by the inner split ring.

8.4.3 Tuning the Frequency Bands

In order to use the MS for specific applications, its frequency bands need to be tuned and scaled to fit the desired specifications. Since the 5.55-5.78GHz and 10.42-10.68GHz bands depend mainly on the semicircular strips, they can be tuned by varying the dimensions of the semicircular strips. Similarly, the 6.1-6.23GHz, 11.06-11.17GHz and 12.03-12.18GHz bands depend mainly on the inner circular split ring and can be tuned by varying its dimensions. The dimensions of the middle omega-shaped structure can also be tuned to enhance the peak magnitudes of the asymmetry bands. All the five frequency bands can be shifted to lower or higher frequencies by scaling the dimensions of the unit cell. To verify this, each dimension of the unit cell is divided by 1.5. The asymmetry parameter of the scaled MS is shown in Fig. 8.7.

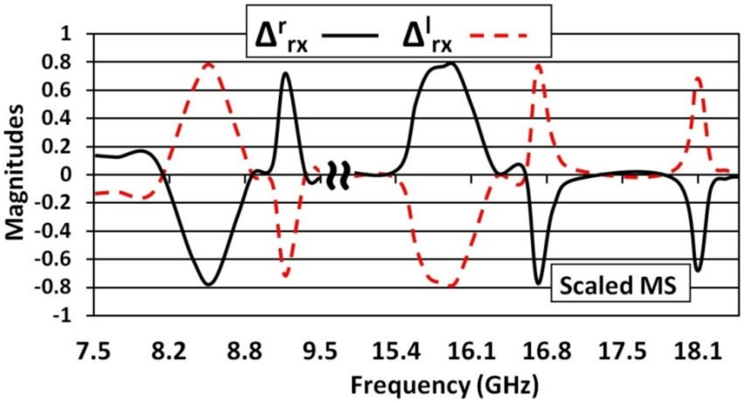

Fig. 8.7. Asymmetric parameter of scaled MS.

It is seen that the center frequency of each asymmetry band has shifted up by about 1.5. The new bands are now centered about 8.49GHz (≈ 1.5 x 5.665GHz), 9.25GHz (≈ 1.5 x 6.165GHz), 15.82GHz (≈ 1.5 x 10.55GHz), 16.67GHz (≈ 1.5 x 11.115GHz) and 18.15GHz (≈ 1.5 x 12.105GHz).

8.5 Experimental Verifications

In order to verify the results, a prototype of the MS is fabricated (Fig. 8.8) with 12 x 12 unit cells (144mm x 144mm). The reflection and transmission coefficients of the MS for LP incident waves having x- and y-directed *E*-field orientations (E_x and E_y) are measured inside an anechoic chamber by using two identical LP dual-ridge wideband horn antennas and a VNA. The MS is placed in the far-field region of both antennas to ensure plane wave incidence. Then, the measured complex LP reflection coefficients (R_{xx}, R_{yy}, R_{xy} and R_{yx},) are converted to the circular basis by using the following equation:

$$\begin{pmatrix} R_{rr} & R_{rl} \\ R_{lr} & R_{ll} \end{pmatrix} = \frac{1}{2}\begin{pmatrix} R_{xx} + R_{yy} + i(R_{xy} - R_{yx}) & R_{xx} - R_{yy} + i(R_{xy} + R_{yx}) \\ R_{xx} - R_{yy} - i(R_{xy} + R_{yx}) & R_{xx} + R_{yy} - i(R_{xy} - R_{yx}) \end{pmatrix}. \tag{8.2}$$

In the above equation, when all the LP coefficients are for forward (backward) incidence, the resulting CP coefficients are also for forward (backward) incidence. Using the calculated CP coefficients, the polarization conversion ratios (PCR) for the five asymmetric reflection bands can be calculated. As discussed in Chapter 7, the PCR is a measure of how efficiently an MS converts the polarization of an incident wave. It is given as $\mathrm{PCR}_{ij} = |R_{ij}|^2/(|R_{ij}|^2 + |R_{jj}|^2)$ where $\{i, j\}$ is replaced by $\{l, r\}$.

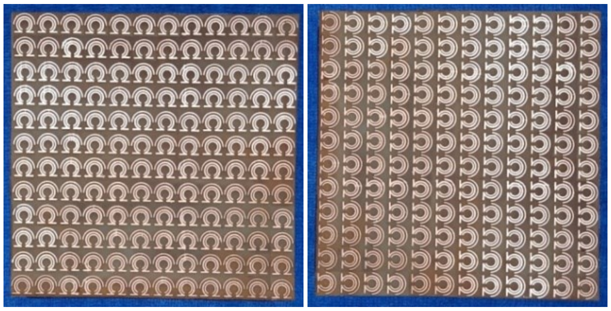

Fig. 8.8. (a) Fabricated prototype of the MS having 144 unit cells.

The measurement configurations for the metasurface are the same as the measurement configurations presented in Sec. 5.5 of Chapter 5. The co- and cross-polarized linear reflection coefficient measurement setups are shown in Fig. 8.9. Using the phase reference and phase measurement method discussed in Sec. 5.5, the complex reflection coefficients needed in (8.2) are calculated.

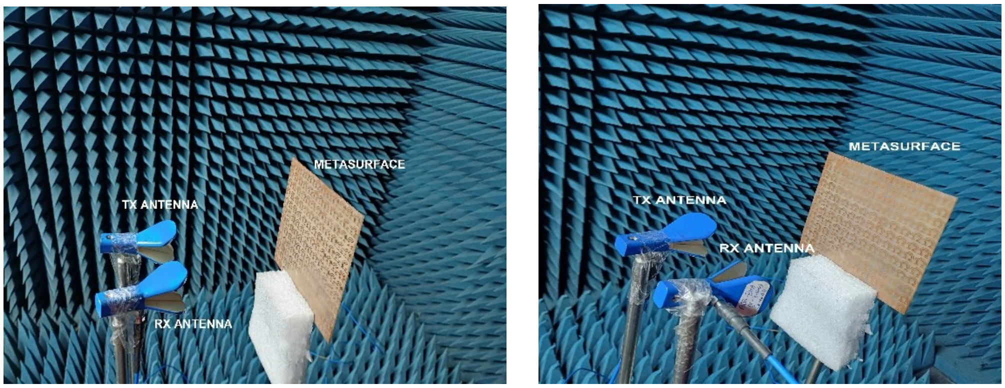

Fig. 8.9 Co-polarization (left) and cross-polarization reflection coefficient measurement setups.

The measured and simulated PCRs are plotted in Fig. 8.10(a). The measured and simulated results show good agreement. The measured angular stabilities of the PCR bands and the asymmetry parameter Δ_{rx} are also plotted in Figs. 8.10(b) and (c) for LHCP and RHCP forward incidences, respectively. Out of the five asymmetry bands, the first four bands have angular stabilities up to 45^0 while the final band (12.03-12.18GHz) has an angular stability up to 30^0. The reduction in angular stability of the final band is due to the increase in the unit cell dimensions with respect to the operating wavelength. At 11.5GHz the unit cell size is ≈ 0.46λ. Above 11.5GHz, the angular stability decreases.

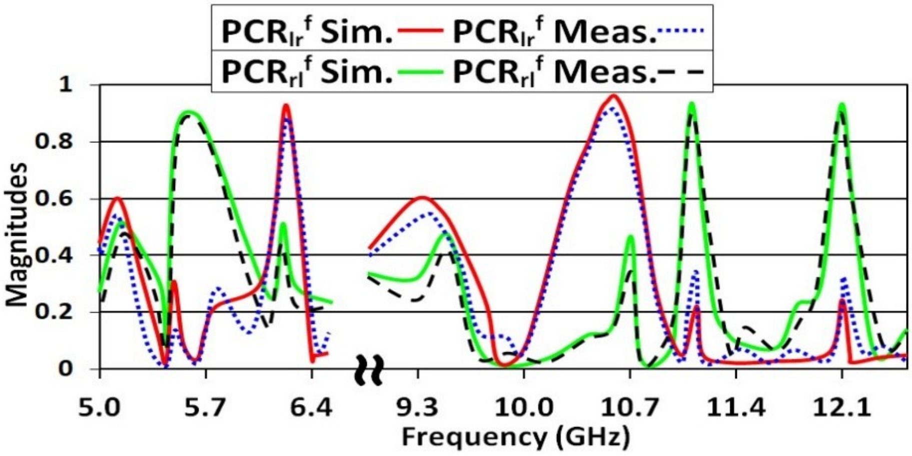

(a)

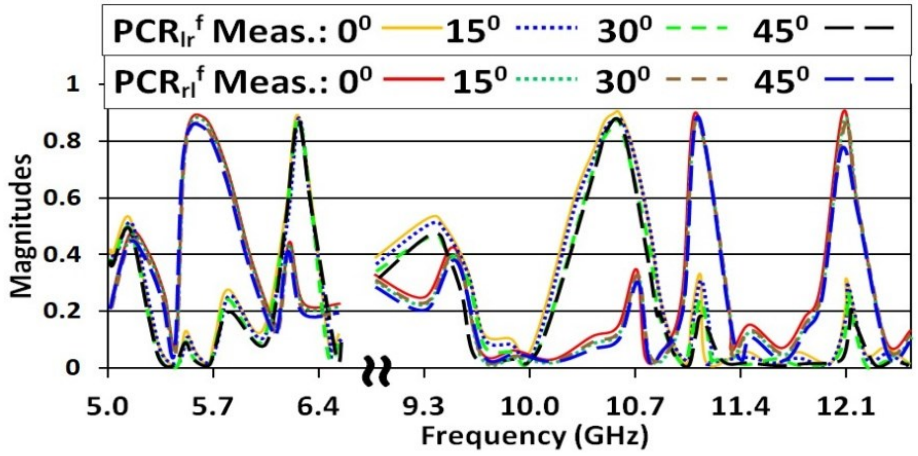

(b)

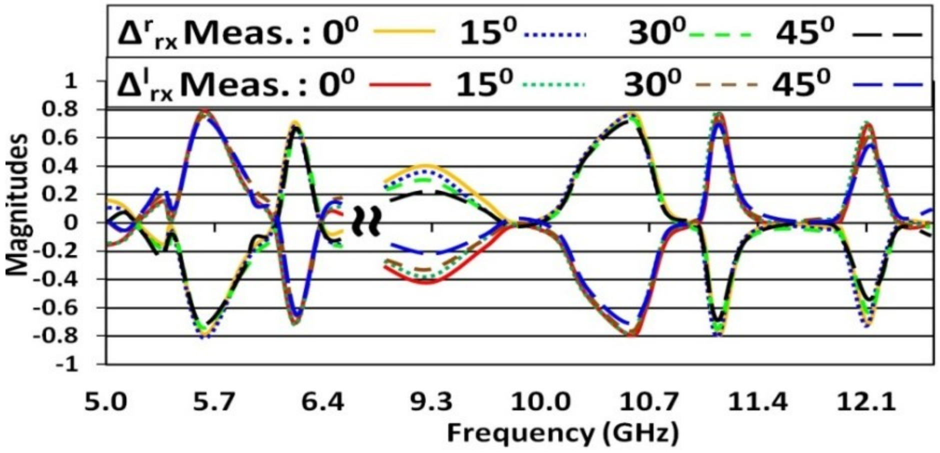

(c)

Fig. 8.10 (a) Simulated and measured PCR at normal incidence. Variations of the (b) PCR and (c) Δ_{rx} for LHCP and RHCP oblique incidence.

The peak measured magnitudes of the cross-polarized reflection coefficients and co-polarized transmission coefficients within the five asymmetry bands are given as follows → 5.55-5.78GHz: R_{rl}^f = 0.91; 6.1-6.23GHz: R_{lr}^f = 0.92; 10.42-10.68GHz: R_{lr}^f = 0.93; 11.06-11.17GHz: R_{rl}^f = 0.92 and 12.03-12.18GHz: R_{rl}^f = 0.92. The magnitudes of the asymmetry parameter, $|\Delta_{rx}|$, remain close to 0.8 within the 5.55-5.78GHz, 10.42-10.68GHz and 11.06-11.17GHz bands up to 45^0. For the 6.1-6.23GHz band, $|\Delta_{rx}|$ remains close to 0.7 up to 45^0 and for the final band (12.03-12.18GHz), $|\Delta_{rx}|$ remains above 0.6 up to 30^0.

To verify the handedness of the reflected waves, two CP patch antenna pairs are used. They are centered at 5.665GHz (LHCP; for the 5.55-5.78GHz band) and at 6.165GHz (RHCP; for the 6.1-6.23GHz band). The antennas are shown in Fig. 8.11 (a).

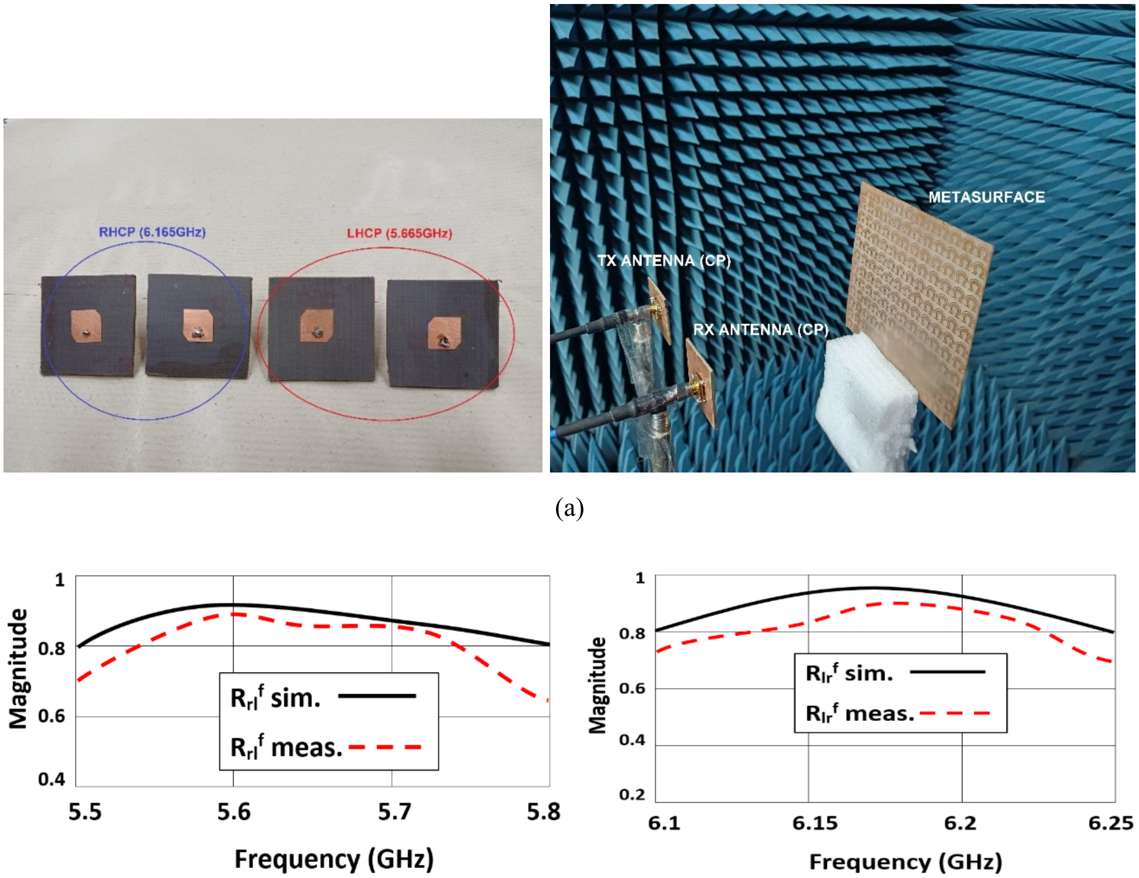

(a)

(b)

(c)

Fig. 8.11 (a) LHCP and RHCP antenna pairs used for measurement (left) and measurement setup (right). (b) Measuring the reflection coefficient magnitude within the 5.5-5.8GHz band for LHCP incidence. (c) Measuring the reflection coefficient magnitude within the 6.1-6.25GHz band for RHCP incidence.

Figure 8.11(b) and 8.11(c) contain a comparison between the simulated cross-polarization reflection coefficients for CP incidence and the measured cross-polarization reflection coefficients for CP incidence using the patch antennas. The measured curves follow the simulated ones.

8.6 Conclusions

A multiband CMS is presented in this chapter which can be used as an asymmetric meta-mirror within the C, X and Ku bands for CP incidence. The operational bands can be adjusted to meet user requirements. The planar and ultrathin nature of the CMS makes it easy to fabricate. It gives a stable response for incident angles up to 45^0 within the first four asymmetry bands and 30^0 within the final asymmetry band.

REFERENCES

[1] V. A. Fedotov, P. L. Mladyonov, S. L. Prosvirnin, A. V. Rogacheva, Y. Chen, and N. I. Zheludev, "Asymmetric propagation of electromagnetic waves through a planar chiral structure," *Phys. Rev. Lett,. v*ol. 97, no.16, pp. 167401–167404, 2006.

[2] R. Singh *et al.,* "Terahertz metamaterial with asymmetric transmission," *Phys. Rev. B*, vol. 80, 153104, 2009.

[3] M. Kenney *et al.,* "Pancharatnam-Berry phase induced spin-selective transmission in Herringbone dielectric metamaterials," *Adv. Mater.*, vol. 28, 9567, 2016.

[4] C. Pfeiffer, C. Zhang, V. Ray, L. J. Guo, and A. Grbic, "High performance bianisotropic metasurfaces: asymmetric transmission of light," *Phys. Rev. Lett.,* vol. 113, 023902, 2014.

[5] K. Tanaka *et al.,* "Chiral bilayer all-dielectric metasurfaces," *ACS Nano,* vol. 14, no. 11, pp. 15926-15935, 2020.

[6] F. Zhang *et al.,* "All-dielectric metasurfaces for simultaneous giant circular asymmetric transmission and wavefront shaping based on asymmetric photonic spin-orbit interactions," *Adv. Funct. Mater.,* vol. 27, 1704295, 2017.

CHAPTER 9

A TRI-BAND SSPP BASED END-FIRE ANTENNA

9.1 Objective

As discussed in Chapters 2 and 3, SSPPs show high-field confinement in a sub-wavelength scale and have been used to design compact antennas [1-9]. Although most antennas designed using SSPPs achieve frequency dependent beam scanning in the broadside direction, some antennas exhibiting end-fire radiation patterns have also been designed [5, 7-9]. But none of the end-fire antennas designed using SSPPs operate in more than one frequency band. They are either broadband or narrowband. Even while studying normal (non-SSPP based) end-fire antennas present in literature, it is found that they work within a single continuous band [10-13].

Sometimes, separate frequency bands are needed for communication purposes and the out of band frequencies need to be suppressed using filters. Dual/tri-band antennas serve this purpose by providing separate frequency bands without the need of filters.

The main aim of this chapter is to design a planar SSPP based antenna which exhibits end-fire radiation within three different frequency bands while also performing frequency-dependent end-fire beam scanning within one of the operational bands.

9.2 Proposed Antenna Geometry

The antenna has been designed and analyzed using CST Studio Suite. The principal radiator is a comb-shaped antenna based on an SSPP transmission line. It is tapered toward the radiating edge to provide gradual impedance matching to free space. The antenna is designed on an FR-4 substrate (thickness = 1.52mm, $\varepsilon_r = 4.3$, and $\tan\delta = 0.02$). The top surface of the substrate contains the SSPP based antenna with a gradually tapered end as shown in Fig. 9.1(a). The antenna is fed by a Co-planar Waveguide (CPW). The width of the central CPW line and the gap with the adjacent ground planes are chosen to present 50Ω impedance to the input port. Another CPW structure is replicated on the bottom surface of the substrate having dimensions identical to the top CPW line. The central conductor of the lower CPW is extended horizontally by a length *L* = 11.7mm and then bent vertically by a length *d* = 7.5mm to form a stub as shown in Fig. 9.1(b). The widths of the central lines of both the CPWs are 1mm and the gaps are 0.15mm as illustrated in the magnified part of Fig. 9.1(b).

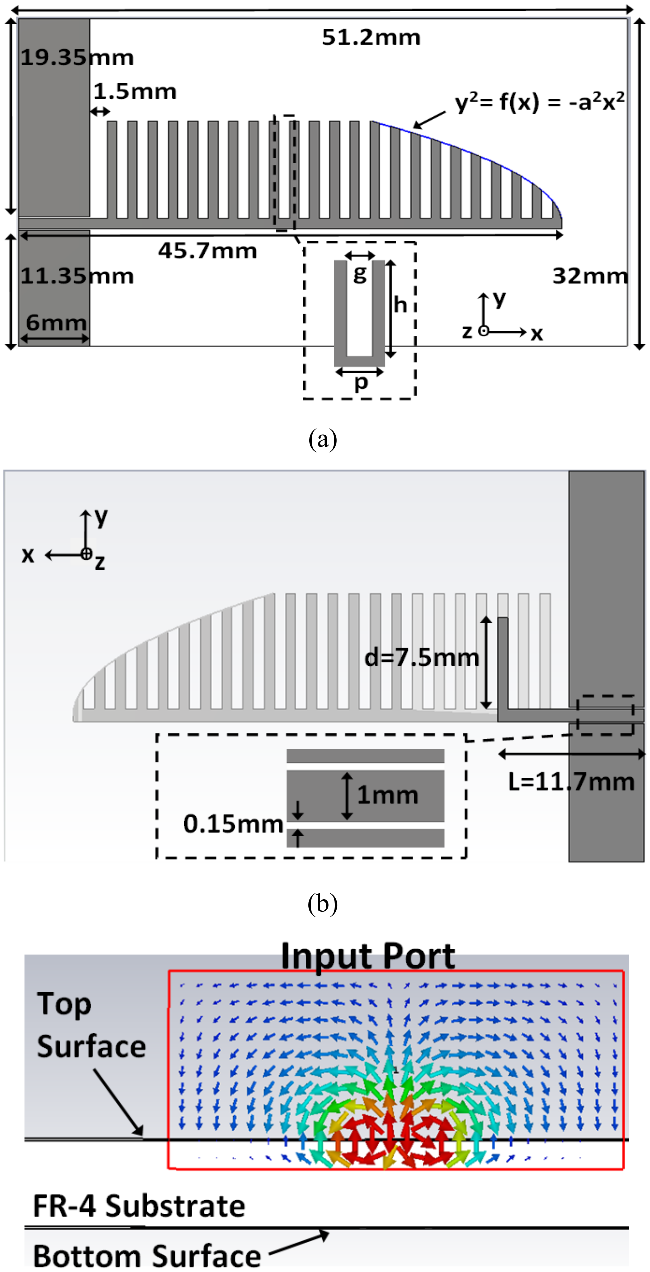

(a)

(b)

(c)

Fig. 9.1. Proposed antenna (a) top and (b) bottom surface. (c) End view of the antenna showing waveguide port position and E-field distributions (V/m).

It should be noted however that the input signal port is connected only with the top CPW while the bottom CPW-like structure forming the stub is simply a parasitic element, which interacts with the fields on the top surface. During simulation, a waveguide port provides signal only to the top CPW structure as shown in Fig. 9.1(c). During fabrication, the central line of only the top CPW is connected to the inner conductor of a Sub-Miniature A (SMA) connector while the grounds of only the top CPW are connected to the outer conductor of the SMA. No input connections are made with the CPW-like structure on the bottom surface. The dimensions of the different parts of the antenna are shown in Figure 9.1(a). The CPW central line also acts as the base of the SSPP transmission line. The end taper of the antenna follows a parabolic profile with a = 2.5. As stated previously, the bottom surface of the substrate contains a similar CPW feed where the central line is bent to form a stub. The effects of the stub will be discussed in a later section.

9.2.1 SSPP Unit Cell

The unit cell of the SSPP transmission line is magnified in Fig. 9.1(a). It has a period P = 1.7mm, height h = 9.5mm, and gap g = 0.8mm. The dispersion diagram of the unit cell is simulated using CST Eigenmode Solver with periodic boundary conditions (PBC) along x-direction. The dispersion diagrams of the unit cell with varying height h are shown in Fig. 9.2. As h increases, the cutoff frequency of the bound SSPP mode reduces. In this chapter, h = 9.5mm is chosen, which results in a cutoff frequency of around 13.2GHz.

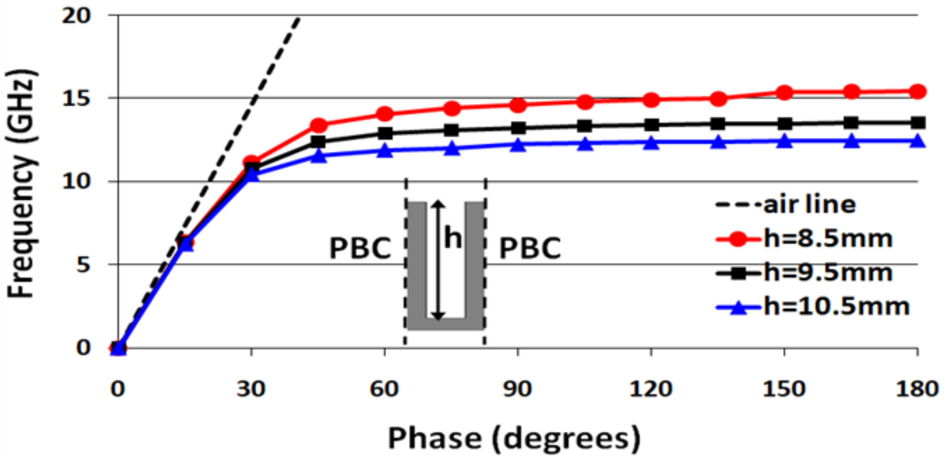

Fig. 9.2. Dispersion diagrams of the SSPP unit cell with varying h.

9.2.2 Unequal Dimensions of the CPW Ground Planes

As shown in Fig. 9.1(b), the central line of the bottom CPW-like structure is extended and bent to form a stub. It can also be seen that the ground lengths of both the top and bottom CPW are unequal, with one being 19.35 mm and the other being 11.35 mm.

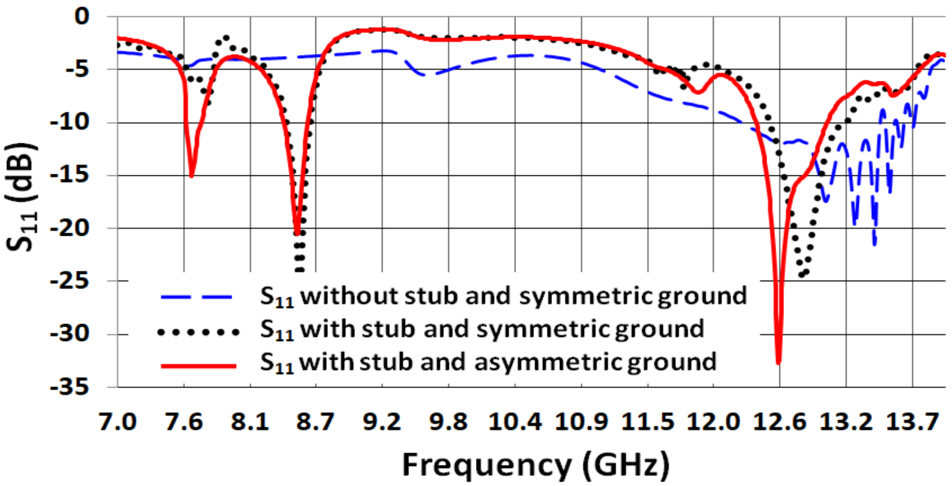

Fig. 9.3. S_{11} vs. frequency for three different cases.

Figure 9.3 compares the simulated S_{11} vs. frequency of three cases. The first case (case 1; blue dashed line) consists of only the comb-like antenna with equal CPW ground dimensions (19.35mm each) on the top surface and nothing on the bottom surface. For this configuration, there is only one band centered roughly around 13GHz (12.4-13.4GHz) where $S_{11} < -10$ dB. The second case (case 2; black dotted line) consists of the comb-like antenna on the top surface as well as the stub on the bottom surface with both having equal CPW ground dimensions (19.35mm each). It can be seen that the addition of the stub and CPW grounds at the bottom leads to a decrease in the -10dB S_{11} bandwidth (BW) of the 13GHz band (which now lies within 12.5-13.2GHz) while introducing a second band near 8.5 GHz where $S_{11} < -10$ dB. The final case (case 3; red solid line) consists of the proposed antenna shown in Figs. 9.1(a) and (b) with both the comb-like antenna and the stub having unequal CPW ground dimensions (19.35mm and 11.35mm). Removing the symmetry of the CPW ground planes (case 3) further leads to a third band near 7.7GHz where S_{11} is below -10dB. Therefore, the final antenna has three bands of operation.

9.2.3 Evolution of the Bottom Structure Geometry

We investigate the effects of the capacitively coupled element, placed on the bottom surface of the substrate, on the SSPP based comb-shaped antenna placed on the top surface.

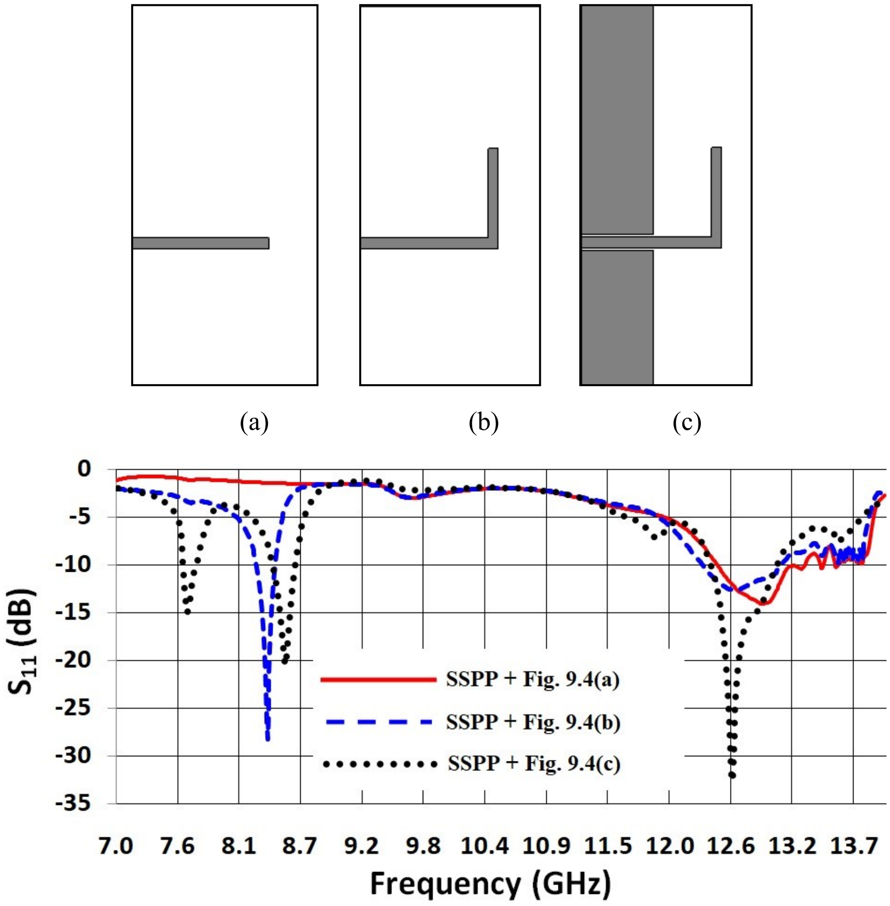

(a) (b) (c)

(d)

Fig. 9.4 (a), (b), (c) Evolution of bottom geometry. (d) S_{11} vs. frequency for the three bottom geometries.

The first capacitively coupled element introduced is a simple horizontal stub as shown in Fig. 9.4(a). The S_{11} of the resulting structure is shown with a red continuous line in Figure 9.4(d). The effect of the simple horizontal stub is negligible and the SSPP antenna has only a single band where S_{11} < -10dB. To enhance the capacitive coupling with the SSPP antenna placed on top, a vertical portion is now added to the horizontal stub, resulting in an L-shaped stub. This is illustrated in Fig. 9.4(b). The S_{11} of the updated structure is shown in Fig. 9.4(d) with a blue dashed line. This structure has an additional band (S_{11} < -10dB) near 8.5GHz. To further enhance the coupling, the asymmetric CPW ground planes present on top are also replicated at the bottom (Fig. 9.4(c)). The S_{11} plot of this final structure is shown in Fig. 9.4(d) with a black dotted line. It can be seen that there are now three S_{11} < -10dB bands.

Therefore, by introducing the asymmetric CPW ground planes on the bottom of the substrate, a third band (S11 < -1 dB) has been introduced near 7.7GHz. It will be seen in the following sections that the vertical portion of the stub is mainly responsible for the band near 8.5GHz while the interaction between the stub and bottom CPW ground planes is mainly responsible for the band near 7.7GHz.

9.3 Electric Field Distributions

The simulated average *E*-field distributions present on the upper and lower surfaces of the antenna at the center frequencies of the three frequency bands are shown in Fig. 9.5. At 7.7GHz, the average *E*-fields on the top surface are concentrated mainly along the ground planes and the tapered radiating edge of the antenna. On the bottom surface, there is an interaction of the fields between the stub and the ground plane. Therefore, increasing the length *d* changes this interaction and shifts the first frequency band.

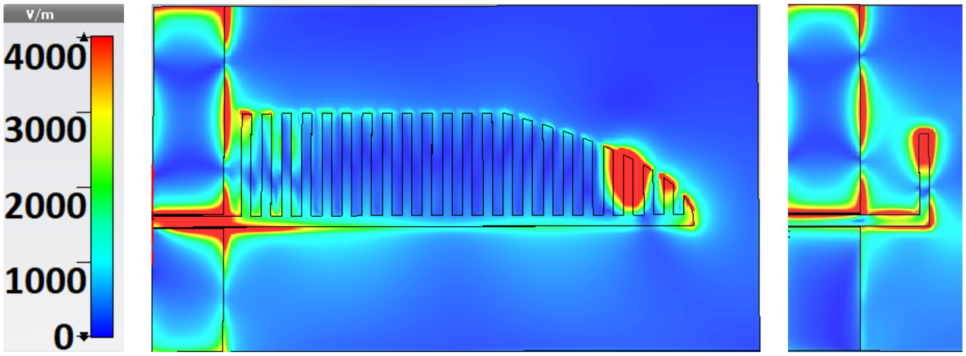

(a)

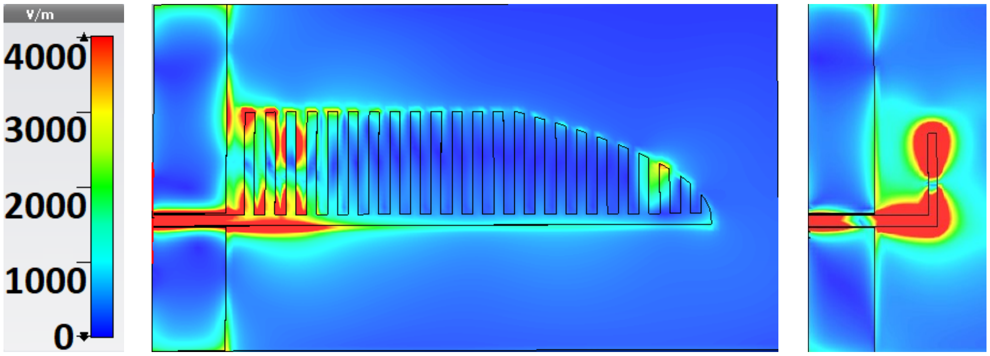

(b)

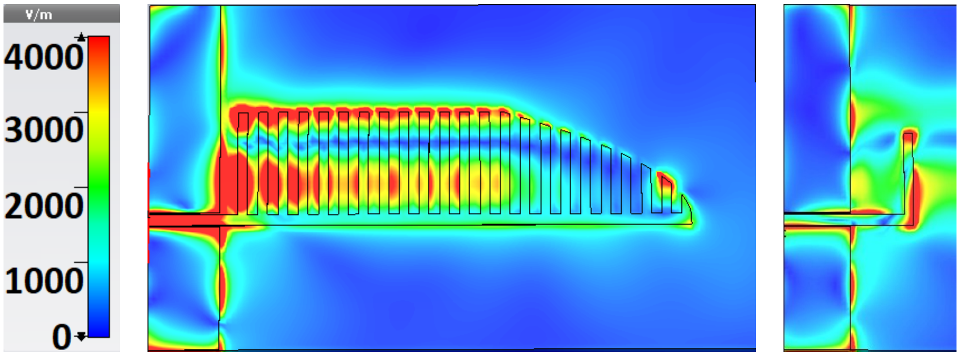

(c)

Fig. 9.5. Average E-field distributions (V/m) on the top (left) and bottom (right) surfaces at (a) 7.7GHz, (b) 8.5GHz and (c) 12.6GHz.

At 8.5GHz, the average *E*-fields on the top surface are concentrated mainly within the first few SSPP unit cells and the tapered radiating edge. On the bottom surface, the *E*-fields are mostly concentrated along the stub. Therefore, changing the position of the stub, *L*, affects the second band. At 12.6GHz, the field distributions on the top surface resemble the usual SSPP propagating mode with the *E*-fields confined within a major portion of the SSPP transmission line before being radiated away as they approach the tapered edge. On the bottom surface, there is some field concentration along the stub which slightly affects the matching of the third band.

9.4 Tuning the Frequency Bands

To find effective ways of tuning the bands, a parametric analysis of the antenna is performed where all the antenna dimensions are varied to study their effects on the frequency bands. The observations from this analysis are discussed below.

The third band (centered at 12.6GHz) of the antenna is the bound propagating SSPP mode which depends mainly on the characteristics of the SSPP unit cell. It can be tuned by changing the height, *h*, of the unit cells. The location of the third band can be determined from the dispersion curve of the unit cell (Fig. 9.2). After parametric analysis involving various values of *h*, it is found that this band starts from frequencies close to (and below) the cutoff frequency for a given *h*. Since increasing *h* reduces the cutoff frequency, this band can be shifted to the left by increasing *h*. The second band (centered at 8.5GHz) can be primarily tuned by changing *L* without affecting the first or third band. However, there is a limit to this tuning. As L increases, the second band shifts left and moves closer to the first band (centered at 7.7 GHz). After a certain value of L, the second band ceases to exist and merges with the first band. After parametric analysis and curve fitting, it is found that the location of the second band can be calculated approximately (to within a few MHz) by using the equation

$$\mathrm{f}_{2\mathrm{nd-band}} = c \times (1.99 + 20.1e^{0.0427L})^{-1}\ \mathrm{GHz} \tag{9.1}$$

where $c = 3 \times 10^{11}$ mm/s (speed of light in vacuum), L is in mm and $L >$ CPW ground plane width (6 mm; Figure 9.1(a)). The first band can be tuned by changing d. However, there is a limit to this tuning as well. After parametric analysis, it is found that the first band can only be tuned properly within the approximate range of $0.57h \le d \le h$. Outside this range, the band does not exist. After parametric analysis and curve fitting, it is found that the location of the first band can be calculated approximately by using the equation

$$\mathrm{f}_{1\mathrm{st-band}} = c \times (31.674d^{0.1033})^{-1}\ \mathrm{GHz} \tag{9.2}$$

where d is in mm and $0.57h \le d \le h$. Therefore, the height of the SSPP unit cell limits the tuning range of the first band.

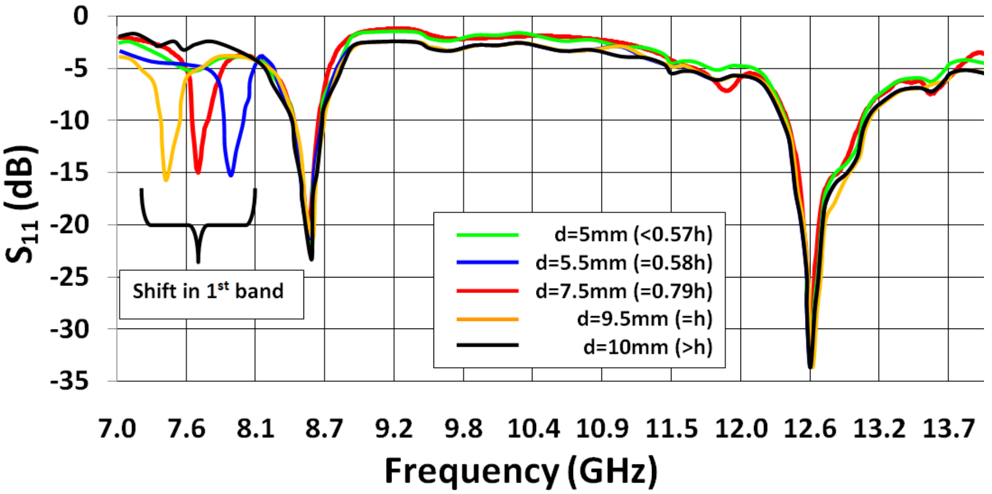

(a)

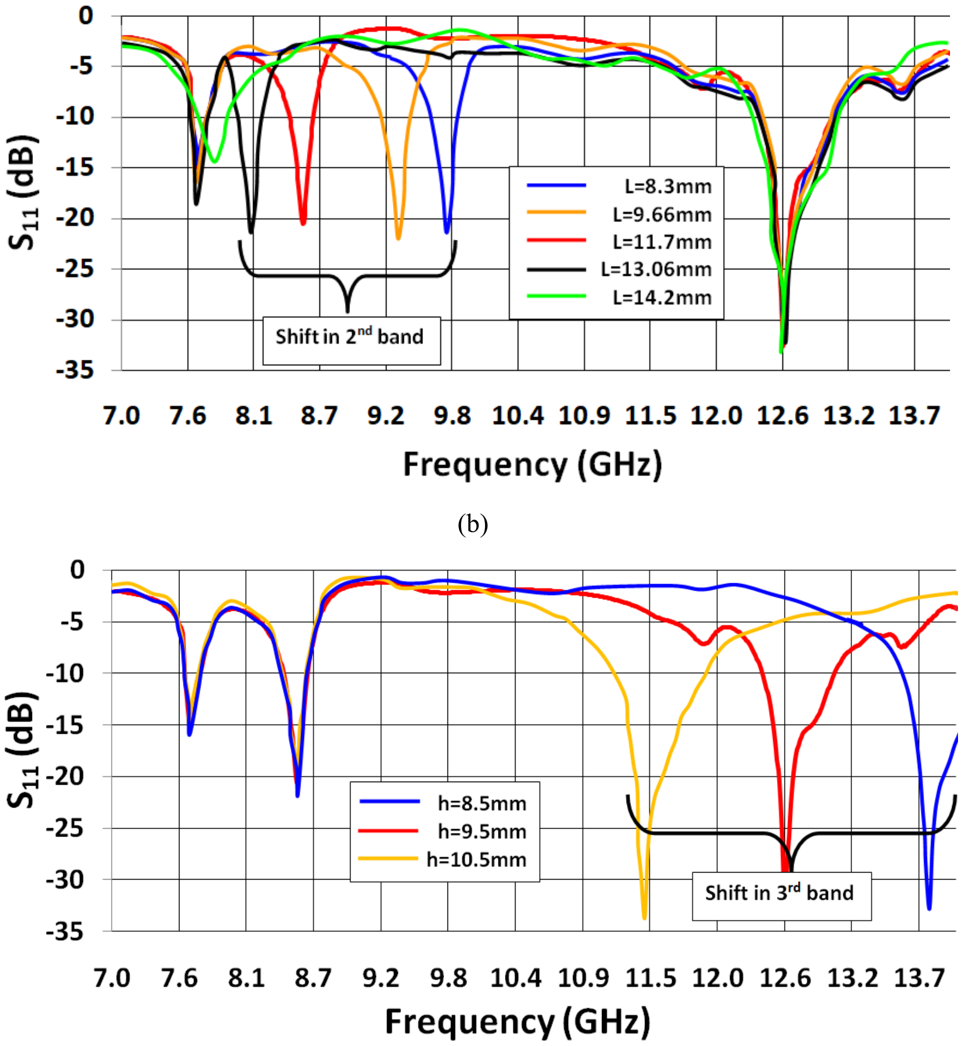

(b)

(c)

Fig. 9.6. Tuning the (a) first band, (b) second band and (c) third band.

The tuning of the frequency bands is shown in Fig. 9.6. The shifts in frequency of the first two bands found from the figure are very close to the frequencies predicted from (9.1) and (9.2). From the above analysis, it can be concluded that although all three bands of the antenna can be tuned independently, there are limits to the tuning range. The first and second bands can be tuned by varying the stub dimensions (*d* and *L*) while the third band depends on the SSPP unit cell dimension *h*.

9.5 Experimental Verifications and Antenna Radiation Patterns

The proposed antenna is fabricated on an FR-4 substrate as shown in Fig. 9.7(a). On observing Fig. 9.7(b), it is seen that the measured S_{11} vs. frequency plot shows good agreement with the simulated S_{11} plot.

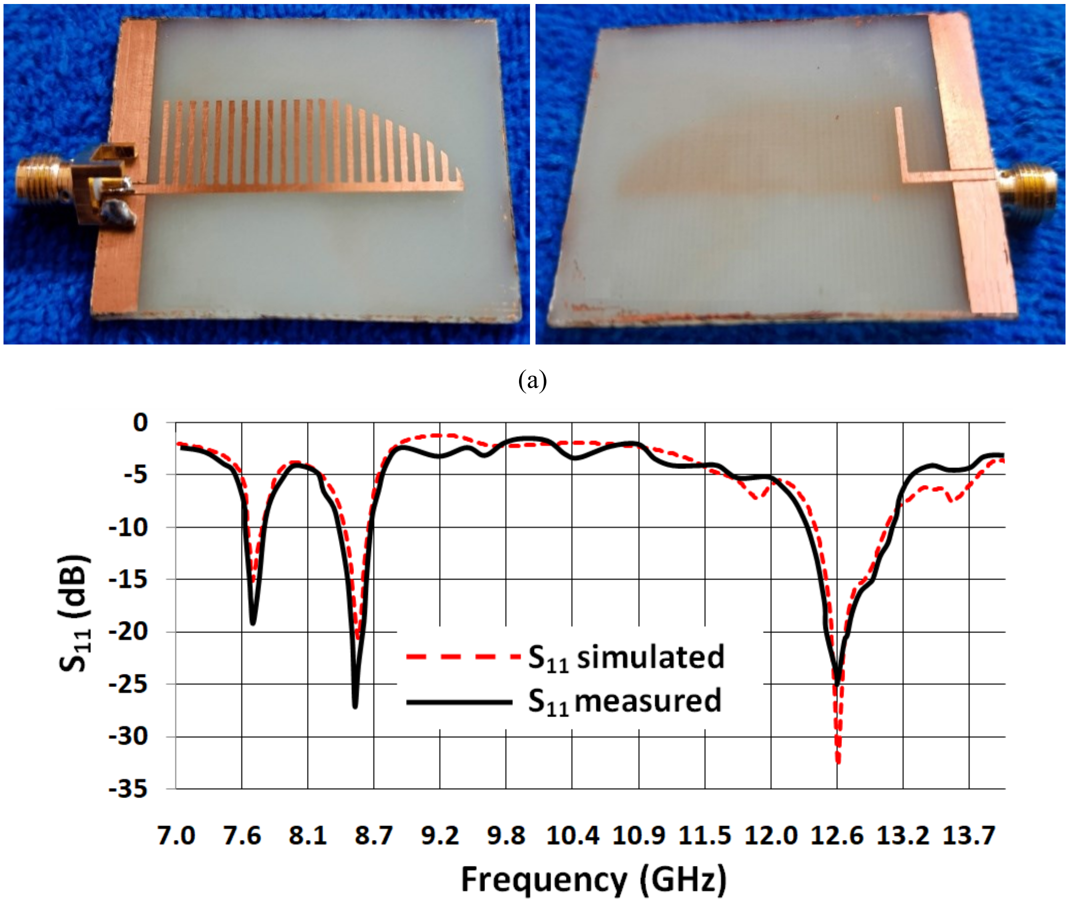

(a)

(b)

Fig. 9.7 (a) Fabricated prototype top and bottom. (b) Comparison between simulated and measured S_{11}.

The -10dB S_{11} BWs of the three bands lie within 7.6-7.75GHz, 8.4-8.68GHz, and 12.4-13GHz with relative BWs of 2% (first band), 3.3% (second band), and 4.8% (third band) respectively. The simulated and measured normalized radiation patterns of the fabricated structure are presented in Fig. 9.8.

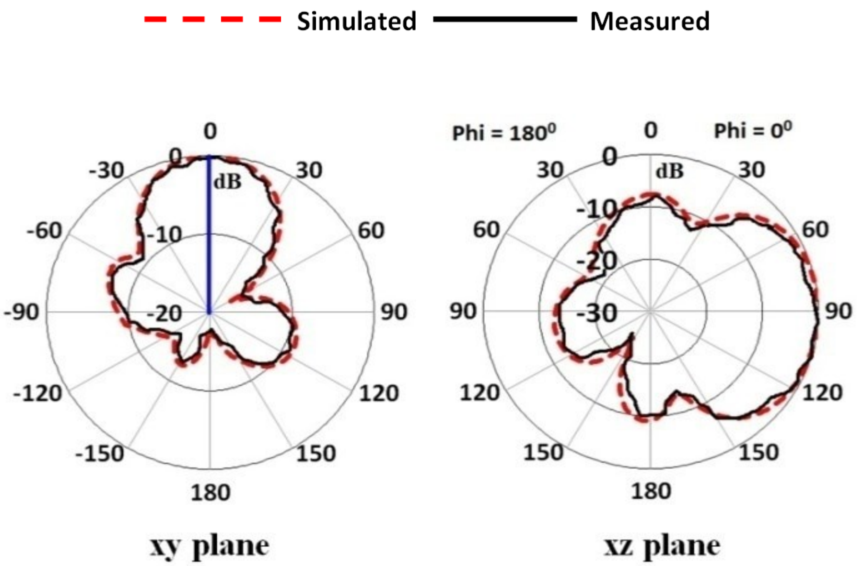
Simulated
Measured
0
30
60
90
120
150
180
-30
-60
-90
-120
-150
dB
0
-10
-20
xy plane
Phi = 180⁰
Phi = 0⁰
-30
xz plane

(a)

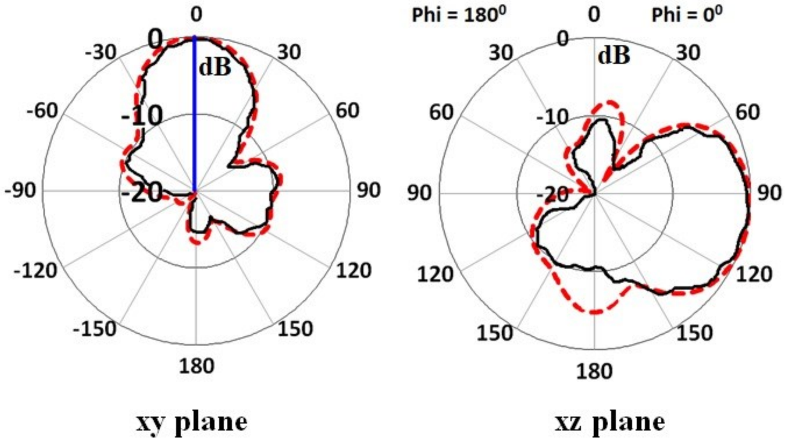
0
30
60
90
120
150
180
-30
-60
-90
-120
-150
dB
0
-10
-20
xy plane
Phi = 180⁰
Phi = 0⁰
xz plane

(b)

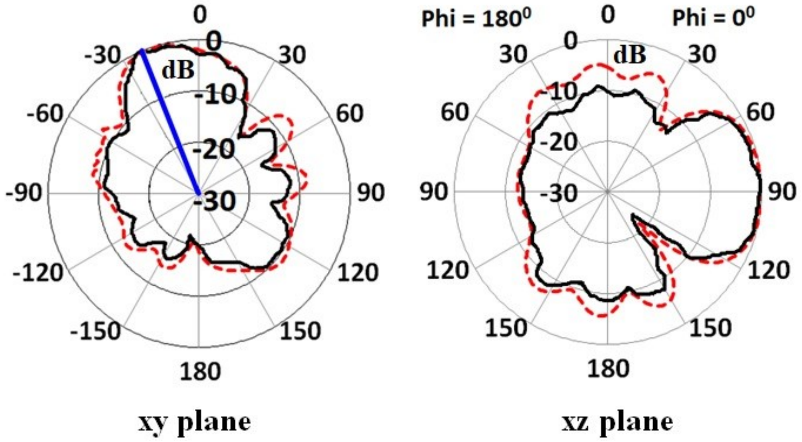
0
30
60
90
120
150
180
-30
-60
-90
-120
-150
dB
0
-10
-20
-30
xy plane
Phi = 180⁰
Phi = 0⁰
xz plane

(c)

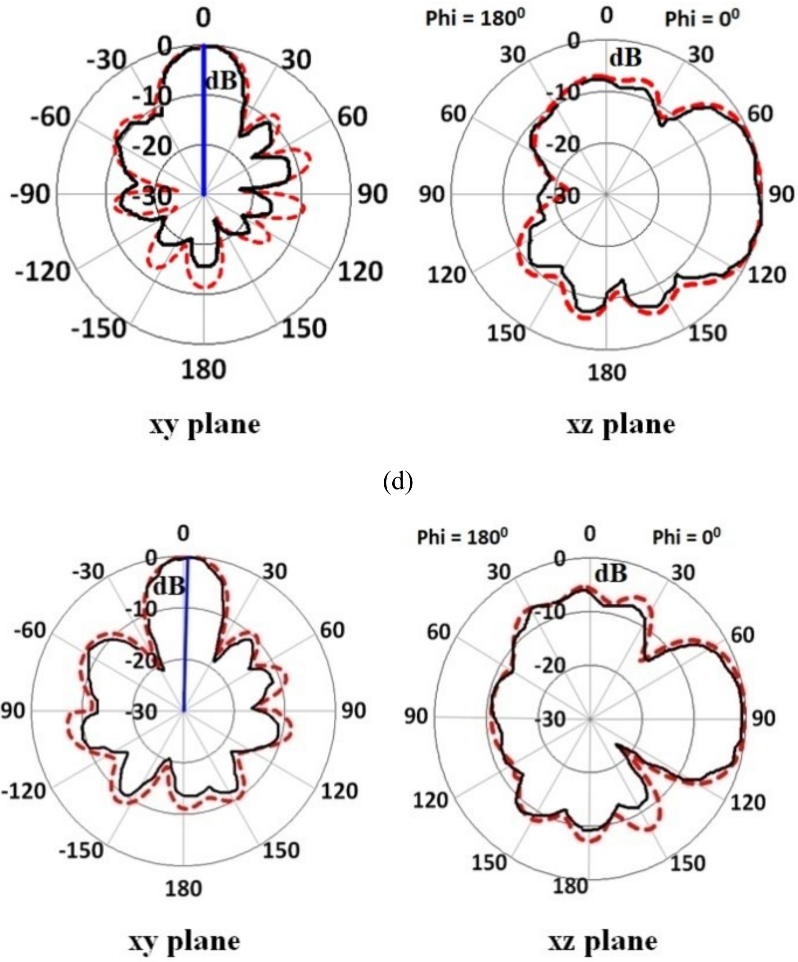

(d)

(e)

Fig. 9.8. Normalized simulated and measured far field patterns at (a) 7.7GHz, (b) 8.5GHz, (c) 12.4 GHz, (d) 12.6GHz and (e) 13GHz.

For each frequency, a solid blue line is drawn to represent the radiation pattern maximum direction in the xy plane. It can be seen from Figs. 9.8 (a) and (b) that the structure exhibits an end-fire radiation pattern at both 7.7GHz and 8.5GHz. An interesting phenomenon is observed within the third frequency band (12.4-13GHz). At 12.4GHz, the main beam of the end-fire radiation points toward phi = -19^0 (xy plane of Fig. 9.8(c)). At 12.6GHz, the main beam of the end-fire radiation points toward phi = 0^0 (xy plane of Fig. 9.8(d)) while at 13GHz, the main beam of the end-fire radiation points toward phi = 2^0 (xy plane of Fig. 9.8(e)). Therefore, the structure exhibits frequency dependent end-fire beam scanning in the xy plane with the scan angle varying from phi = -19^0 to phi = 2^0. A total scan range of 21^0 is achieved within 600MHz. It should also be noted that the 3dB beamwidth of the antenna exhibits a total scan range of 51^0 from phi = -35^0 to phi = 16^0. This can be a beneficial feature in cases requiring end-fire beam scanning.

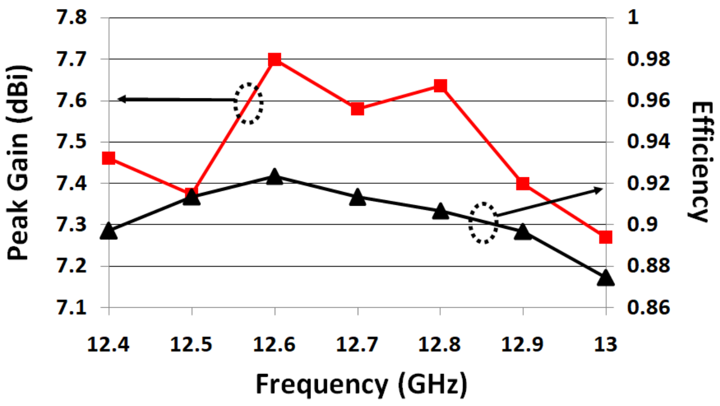

Fig. 9.9. Measured peak gain vs. frequency and simulated efficiency vs. frequency within the third band.

Maximum measured gains are found to be 7dBi at 7.7GHz and 7.5dBi at 8.5GHz with simulated efficiencies of 86% and 96% respectively. The maximum measured gain and simulated efficiency vs. frequency in the third band (12.4-13GHz) are shown in Figure 9.9. It can be seen that gain throughout the third band is >7.2dBi while the efficiency is >86%. Hence, the designed antenna shows high efficiency and good gain in all the three bands.

9.6 Advantages of the Proposed SSPP based Antenna

The antenna proposed in this chapter is the first SSPP based end-fire antenna to operate within three distinct frequency bands. It also exhibits frequency dependent end-fire beam scanning in the xy plane (plane of the antenna) in the third band. The antenna has a very low profile and uses only a single feed to achieve three bands as well as beam scanning. It is also single layered and simple to fabricate.

Table 9.1 provides a comparison of the proposed antenna with both SSPP based end-fire antennas [5, 7-9] and normal end-fire antennas [10-13] found in literature. It should be noted that although the gains and BWs of the other antennas are better, the proposed antenna possesses three operating bands and beam scanning ability in the third band, which makes it unique and advantageous for multiple applications. The measured gain of the antenna in the three bands are also sufficiently high (7, 7.5, and 7.7dBi respectively) for carrying out efficient communication.

Table 9.1. Comparisons with some existing end-fire antennas.

Ref.	No. of frequency bands	Beam scanning in the antenna plane	Size (w.r.t free space wavelength of lowest frequency)	End-fire band BW (%)	Peak Gain within operating band (dBi)
5	1	No	$2.85\lambda_0$ x $0.8\lambda_0$	12.5	9.2
7	1	No	$9.25\lambda_0$ x $4.43\lambda_0$	10.5	12.1
8	1	No	$2.26\lambda_0$ x $0.64\lambda_0$	No data	7
9	1	No	$3.33\lambda_0$ x $0.74\lambda_0$	7.3	7.86
10	1	No	$1.43\lambda_0$ x $0.36\lambda_0$	17.5	10.2
11	1	No	≈ $6.4\lambda_0$ x $6.4\lambda_0$	26	15.3 (dBic)
12	1	No	$0.7\lambda_0$ x $0.1\lambda_0$	6.45	4.9 (dBic)
13	1	No	$7.33\lambda_0$ x $3.8\lambda_0$	54	14.9
This work	3	Yes (3rd band)	$1.3\lambda_0$ x $0.81\lambda_0$	2 (1st band) 3.3 (2nd band) 4.8 (3rd band)	7 (1st band) 7.5 (2nd band) 7.7 (3rd band)

The beam scanning ability of the antenna can be used for mobile communication as well as target detection in electronic warfare (in the form of radars). It can also be used for Ku band satellite communication. But in that case, the antenna must be oriented in such a way that the beam maximum points toward the +z axis.

One of the possible scenarios in which the proposed structure can be used is as follows: The first two bands of the antenna can be used for information exchange with base stations/control stations while the third band of the antenna can be used for target detection (due to its beam scanning ability). The proposed structure can then operate as a normal antenna in the C and X bands while working as radar in the Ku band. When an increased scan range is needed, two units of the proposed antenna can be designed and placed on top of each other (with sufficient spacing between them to prevent mutual coupling) in such a manner that one of the antennas scans from -19^0 to $+2^0$ while the other antenna scans from $+19^0$ to -2^0. Due to the high-field confinement of the SSPP antenna, the two units of the proposed antenna can be placed quite close to each other without much mutual coupling. Therefore, a total scan range of 38^0 can be achieved.

9.7 Conclusions

In this chapter, a planar SSPP based antenna is presented, which exhibits end-fire radiation patterns at three distinct frequency bands. The main radiator consists of a coplanar waveguide fed comb-shaped spoof surface plasmon polaritons based antenna placed on top of a microwave substrate. An L-shaped stub like structure is added to the bottom of the substrate and is coupled electromagnetically to the main radiator. The resulting antenna operates in three frequency bands. It achieves end-fire radiation within 7.6-7.75GHz (first band), 8.4-8.68GHz (second band) and 12.4-13GHz (third band) with maximum measured gains of 7dBi, 7.5dBi and 7.7dBi respectively. The antenna dimensions are $1.3\lambda_0$ x $0.81\lambda_0$ x $0.038\lambda_0$ (51.2 x 32 x 1.52 mm) where λ_0 = free space wavelength at 7.6GHz. The antenna has a maximum simulated efficiency of 86% at 7.7GHz, 96% at 8.5GHz, and 92% at 12.6GHz. The structure also exhibits frequency dependent end-fire beam scanning within the 12.4 to 13 GHz band in the xy plane (plane of the antenna), achieving a total scan range of 21^0 from phi $= -19^0$ to phi $= 2^0$.

REFERENCES

[1] Z. C. Hao, J. Zhang, L. Zhao, “A compact leaky-wave antenna using a planar spoof surface plasmon polariton structure,” *Int. J. RF Microwave Comput. Aided Eng*., vol. 29, no. 5, e21617, 2019.

[2] H. W. Yu, Y. C. Jiao, Z. Weng, “Spoof surface plasmon polariton fed circularly polarized leaky-wave antenna with suppressed side-lobe levels,” *Int. J. RF Microwave Comput. Aided Eng*., vol. 30, no. 3, e22080, 2019.

[3] S. D. Xu, L. Liu, D. F. Guan *et al*., “A hybrid substrate integrated waveguide and spoof surface plasmon polaritons leaky-wave antenna with open stopband suppressed,” *Int. J. RF Microwave Comput. Aided Eng.,* e22413, 2020.

[4] T. Zhong, H. Zhang, “Continuous scanning leaky-wave antenna utilizing second-mode spoof surface plasmon polaritons excitation,” *Int. J. RF Microwave Comput. Aided Eng*., vol. 30, no. 11, e22418, 2020.

[5] A. Kandwal, Q. Zhang, X. L. Tang, L. W. Liu, G. Zhang, “Low-profile spoof surface plasmon polaritons traveling-wave antenna for near-end-fire radiation,” *IEEE Antennas Wireless Propag. Lett*., vol. 17, no. 2, pp. 184-187, 2018.

[6] L. Liu, Z. B. Yang, D. F. Guan *et al*., “An SIW antenna utilizing odd mode spoof surface plasmon polaritons for broadside radiation,” *Int. J. RF Microwave Comput. Aided Eng*., e22177, 2020;

[7] L. Liu, M. Chen, X. Yin, “Single-layer high gain end-fire antenna based on spoof surface plasmon polaritons,” *IEEE Access*., vol. 8, pp. 64139-64144, 2020.

[8] J. Y. Yin, D. Bao, J. Ren *et al*., “End-fire radiations of spoof surface plasmon polaritons,” *IEEE Antennas Wireless Propag. Lett*., vol. 16, pp. 597-600, 2017.

[9] D. Tian, R. Xu, G. Peng *et al*., “Low-profile high-efficiency bidirectional end-fire antenna based on spoof surface plasmon polaritons,” *IEEE Antennas Wireless Propag. Lett.,* vol. 17, no. 5, pp. 837-840, 2018.

[10] H. Guo, W. Geyi, “Design of bidirectional antenna array with adjustable end-fire gains,” *IEEE Antennas Wireless Propag. Lett*., vol. 18, no. 8, pp. 821-824, 2019.

[11] X. Ruan, C. H. Chan, “An end-fire circularly polarized complementary antenna array for 5G applications,” *IEEE Trans. Antennas Propag*., vol. 68, no. 1, pp. 266-274, 2020.

[12] B. Xue, M. You, W. J. Lu, L. Zhu, “Planar end-fire circularly polarized antenna using concentric annular sector complementary dipoles,” *Int. J. RF Microwave Comput. Aided Eng*., vol. 26, no. 9, pp. 829-838, 2016.

[13] H. Bai, G. M. Wang, X. J. Zou, “Broadband substrate-integrated waveguide-fed end-fire metasurface antenna array with gain enhancement,” *Int. J. RF Microwave Comput. Aided Eng*., vol. 31, no. 4, e22551, 2021.

CHAPTER 10

CONCLUSIONS

In this concluding chapter, we summarize the contributions of the dissertation and discuss future research areas in the domain of metasurfaces.

10.1 Contributions of the Thesis

In Chapter 4, a dual-band RFID reader antenna is presented which radiates CP waves within both the UHF-RFID band and 2.4GHz WLAN band. Using an AMC reflector below the reader antenna, the gain of the antenna is enhanced within the UHF-RFID band which in turn increases the read range. The resulting antenna plus reflector system is easy to fabricate, has a low profile height and can detect RFID tags irrespective of their orientation due to the CP nature of the radiated waves. The information received from the tags can then be sent by the reader to a base-station through the 2.4GHz WLAN band.

In Chapter 5, an AMC is designed using self-complementary unit cells. The resonance frequency of the proposed AMC remains fixed for different *E*-field orientations as well as for incident angles up to 88^0 for both transverse electric and transverse magnetic incidence. It is very useful in applications which are sensitive to the shift in resonance frequency. The proposed AMC has the best angular stability out of all AMCs present in literature till date. It is also easy to fabricate and ultrathin, making it easily reproducible.

In Chapter 6, a dual-band FPCA is presented. It radiates CP waves within the 2.4GHz WLAN band and LP waves within the 5.8GHz WLAN band. The PRS is made using a single dielectric layer having metallization on both sides and a positive reflection phase gradient. The positive reflection phase helps the antenna achieve a wide 3dB gain bandwidth. The radiating antenna placed within the cavity is surrounded by an AMC ground plane. This ultimately helps in reducing the height of the FPCA. The resulting FPCA has very high gain, wide 3dB gain BWs within both the bands and a reduced cavity height of around $\lambda/6$ (as opposed to the conventional cavity height of $\lambda/2$) with respect to the 2.4GHz band. All these features make the proposed antenna desirable in applications requiring high gain antennas with small vertical heights.

In Chapter 7, a multiband and ultrathin CMS is presented which has seven operational frequency bands. It can perform asymmetric transmission of LP waves within five bands, asymmetric LTC within one band and symmetric co-polarized transmission within one band. The antenna can be used as a direction of propagation dependent cross-polarization and liner-to-circular polarization converter. It can also be used as a direction of propagation independent co-polarized spatial pass-band filter. All the operational bands of the proposed CMS can be tuned and adjusted to meet user specifications. Multiple bands ensure that the CMS can be integrated with different applications in different frequency bands.

In Chapter 8, an ultrathin multiband CMS is designed. It acts as a meta-mirror for incident CP waves. The handedness of the CP wave remains preserved before and after reflection from the meta-mirror. The proposed CMS has five operational bands. All the bands can be shifted and tuned by varying the different parts of the unit cell. The CMS is very easy to design and fabricate.

In Chapter 9, an SSPP based tri-band antenna is designed which exhibits end-fire radiation within the three operating bands. It can also perform end-fire beam scanning within the third operating band, achieving a scan range of 21^0 in the plane of the antenna. The antenna has good radiation efficiency and gain within all three bands. The proposed antenna is the first SSPP based antenna which exhibits end-fire radiation within three distinct frequency bands.

10.2 Future Research Areas

Graphene based MSs for THz applications are an interesting prospect. Although they have been studied to some extent, more work can be done on this topic. Such arrangements can provide large BWs as well as tunability. With the advancement of fabrication techniques, realizing such structures will also become easier.

In this dissertation, we only deal with passive MSs whose properties are fixed with respect to the geometries of the unit cell. However, introducing switching elements like PIN diodes or tuning elements like varactor diodes to each unit cell can increase the operating range as well as functionality of the MS. Such reconfigurable MSs can be useful in many applications which require dynamic control of the MS properties.

Space-time modulated metasurfaces, although not a part of this dissertation, have become a hot area of research in recent times. Such MSs are ultrathin, planar and can break reciprocity without the use of magnets. They can be used to design nonreciprocal metasurfaces for advanced wave-front engineering. A lot of research can still be conducted on these space-time modulated metasurfaces.

Huygens' metasurface is another type of metasurface which has become popular in recent times. Such an MS consists of both electric and magnetic dipole moments which are orthogonal to each other. They can be used to achieve reflection-less refraction and they can also control the refraction angle for a given incident angle. Huygens' metasurfaces have also been used to design thin lenses for beam collimation. These MSs hold a lot of potential for future research.

The field of metamaterials and metasurfaces is evolving rapidly with a lot of research being conducted worldwide by some of the leading researchers and academicians. It is expected that metasurfaces and metamaterials with new and unique properties will be developed in the forthcoming years which will revolutionize the domain of electromagnetic engineering.